UNIVERSITY OF
BIRMINGHAM

MODELLING AND EXPERIMENTS OF METAL INTERCONNECT DEGRADATION IN SOLID OXIDE FUEL CELLS

by

Mélissa Oum

A thesis submitted to the University of Birmingham for the degree of

DOCTOR OF PHILOSOPHY

Centre for Fuel Cell and Hydrogen Research

School of Chemical Engineering

College of Engineering and Physical Sciences

University of Birmingham

December 2020

Abstract

Chromium is a key component of ferritic stainless steels developed for solid oxide fuel cell (SOFC) interconnect components. The properties of these steel alloys change over time due to the formation of a chromia scale and subsequent volatilisation of chromium gaseous species. As the operational temperature of SOFC systems is continuously reduced, the present thesis reports research aimed at investigating the behaviour of chromium in stainless steels, at 700°C – from an experimental and modelling point of view.

The research consisted of three stages. The first stage involved a detailed study of the sinterability of pure chromium at 1150°C and the isothermal oxidation of the sintered pellets at 700°C in dry and humidified atmospheres. The aim was to optimise the sinterability of chromium and improve the understanding of pure chromium behaviour at a reduced operating temperature. The results showed that for both binder-free and binder containing chromium pellets, sintering time was the determining factor to achieve low porosity and high-density pellets. No volatile chromium was found in dry oxidation at this temperature and the study revealed that the duration of exposure and the chromium collection method used influenced the values of oxidation and evaporation rate constants obtained.

The second stage involved a study of the isothermal humidified oxidation at 700°C of commercial ferritic steels K41 and Crofer 22H. The study aimed primarily at deriving oxidation and volatilisation rate constants from the oxide growth for use in the modelling of the lifetime of the binary system FeCr. Crofer 22H, whilst equally growing a spinel oxide surface layer, showed less chromium evaporation than K41. Besides this, effects of sample preparation method were also investigated, which demonstrated that compared to other

methods commonly used, a refined grinding was the most effective pre-treatment method in achieving a thinner oxide.

The final stage involved designing a one-dimensional thermodynamic-kinetic diffusion and oxidation model for the FeCr system. The developed model can predict the sequential layering oxide phases that are not always differentiable experimentally as well as quantify oxide growth thickness and depletion profiles of chromium in single-phase Fe-Cr binary alloys, using the Calphad approach and finite difference method. The thermodynamic modelling predicted the successive oxide phases formation at 700°C: $(Fe,Cr)_2O_3$, spinel $(Fe,Cr)_3O_4$ and halite (FeO) and highlighted the inconsequential effect of the oxygen partial pressure at values higher than 10^{-8} atm. The kinetic calculations applied to Fe17Cr and Fe22Cr inferred that in the long term, for the Fe17Cr alloy, it would take 26,500 hours of exposure to a cathodic SOFC atmosphere to reach the critical minimum chromium concentration of 11 wt.%, whereas the same concentration would be reached after 53,500 hours for the Fe22Cr alloy.

À mes sœurs Barbara et Danielle, et à moi-même : A chaque étape de cet enfer qu'est la vie, je ferai toujours de mon mieux pour nous. Entre monts et vallées, contre vents et marées.

Acknowledgements

A PhD, like life is a journey. It comes with its share of happiness and despair, and it brings people to share either with. My acknowledgments extend beyond this page to anyone who has ever given out of their time to help me in the smallest possible way: I am forever grateful.

My heartfelt thanks to Prof. Robert Steinberger, my supervisor, who gave me this once in a lifetime opportunity. Thank you for your patience and guidance throughout the years and showing up for me when I needed it the most, none of this would have happened it wasn't for you Prof. My thanks to Birmingham University and the Engineering and Physical Sciences Research Council (EPSRC) for their financial support throughout the years. To the Hydrogen & Fuel Cells Doctoral Training Center (DTC) research group, in particular its manager Dr. Ahmad El-Kharouf and laboratory supervisor Chyntol Kayimbe for providing an enjoyable atmosphere to work in, fixing all the technicalities and equipment in the labs, and always being available for discussion.

I would like to particularly thank John Hooper, Lynn Draper, Christine Dickson, and Dr. Mark Taylor for their support in troubled waters, of which you saved me out from many times. My heart overflows of gratefulness for you all.

I would like to acknowledge and thank my ship peers in this long voyage, Abby-Abs S., Aimee J., Alan S., Chris H., Diana M., Kun Z., Lina.T, Nikkia M., Oujen H.P, Recep A., Rizki A., Sam. S, Sathish P., and, Zeyu J., for all the help in the labs and beyond, all the cheerful conversations that helped me put things in perspective, all the good times we had together. Each one of you has played a part in this written work.

I would also like thank Anastasia V., Anastassia M., Artemis T., Christelle K., Khalid A., Léah, Roméo P., Stephanie S., Steve T., and William G., for their encouragement. Thank you, Francis M., for the drawing.

Hats off to my mum, dad and my sisters Barbara and Danielle for supporting me in the best way they knew and could. I love you more than words can ever say.

Finally, I would like to thank myself, for growing in resilience and strength, and showing up, year after year, with self-love. To anyone reading this in their journey, if you can't run then walk, and if you can't walk then crawl, but whatever you do, just never give up on yourself. You can do this.

List of Presentations

1. 08th European SOFC & SOE Forum, Luzern, Switzerland, 01-07 July 2016 (Poster presentation).

2. H2FC SUPERGEN 2016 Conference, Belfast, UK, 12-14 December 2016 (Poster presentation).

3. Fuel Cell & Hydrogen Technical Conference, Birmingham, UK, 31 May-01 June 2017 (Poster presentation).

4. 15th Symposium on Solid Oxide Fuel Cells, 23 -28 July 2017, Hollywood, Florida USA (Oral Presentation).

5. Chemical Engineering Department Research poster day, 22nd June 2019, University of Birmingham, UK, (Poster presentation, certificate of achievement 'best engaging poster').

6. ANSOLE days, 2-6th September 2018, Bandjoun, Cameroon (Oral Presentation, award certificate).

7. EFC-Workshop – High Temperature Corrosion under Complex Conditions, Deposits and Salts, 26 - 28 September 2018 DECHEMA-Haus, Frankfurt (Poster presentation).

List of Publications

1. Oum. M., Steinberger R., *Degradation and Lifetime Prediction for SOFC Metal Interconnects: A Review on Modelling Techniques*. 2021. (In Review)

2. Oum. M., Andrews J., Steinberger R., *Modelling Microstructural and Chemical Degradation of Ferritic Stainless Steels for SOFC Interconnects* ECS transactions. 2017. Volume 78. 1565-1574.

3. Steinberger *et.al Benchmarking Protective Coatings for SOFC ferritic Steel Interconnects – The SCORED 2:0 Project*. 2016. Conference paper. 12th European SOFC & SOE Forum.

4. Oum M., Hong J.E, Steinberger R., *Thermochemical and Kinetic Modelling of Chromium-Rich alloys*. Conference paper. 12th European Proceedings 12th SOFC & SOE Forum. 2016.

Table of Contents

List of Tables

List of Figures

List of Abbreviations

Abbreviation	**Definition**
ASS	Austenitic Stainless Steel
ASR	Area Specific Resistance
DSS	Duplex Stainless Steel
CTE	Coefficient of Thermal Expansion
EDS	Energy Dispersive Spectrometry
FSS	Ferritic Stainless Steel
LSM	Lanthanum Strontium Manganite
MSS	Martensitic Stainless Steel
NiBSA	Nickel Based Super Alloys
ODS alloys	Oxide Dispersed Strengthened Alloys
PEMFC	Polymer Electrolyte Membrane Fuel Cell
PSD	Particle Size Distribution
SEM	Secondary Electron Microscopy
SOFC	Solid Oxide Fuel Cell
UV-VIS	Ultraviolet-Visible (spectroscopy)

YSZ	Yttria-Stabilised Zirconia
XRD	X-ray Diffraction

Chapter 1 Introduction

« *Toute chose a un début…* »

1.1 Context

In December 2019, the COP25 meeting reported the continuous increase of greenhouse gas emissions caused by an ever growing industrialisation of our communities, with a growing and measurable impact on the environment and climate [1]. To minimise global warming and its associated effects, a move towards sustainable technologies is imperative to reduce the reliance on fossil fuel energy sources. In the last century, various technologies have been introduced within the energy sector, and active research enables their continuous development. In the renewable energy sector, combining approaches seems to be the way forward, considering the fluctuating nature of solar and wind energy, with peaks and lows of production. A typical scenario would be the provision of energy storage and electricity grid control through the collection of excess energy produced via wind, solar, or tidal power. This excess clean energy could be used to power the electrolysis of water, thereby producing hydrogen (H_2) gas. The latter can be used in a Polymer Electrolyte Fuel Cell (PEFC) device installed in an electric vehicle and can supply continuous power. Solid Oxide Fuel Cells (SOFC) are for their part used as generators in homes and buildings, with a maximum fuel-to-electricity efficiency conversion of 60% and above, and 85% and more if heat recovery (co-generation) is included. SOFCs have started to anchor themselves in residential markets for combined heat and power units (CHPs), deployed in countries such as Japan, South Korea, and Germany, and they are soon to be deployed in India with an output range between 0.5 and 10 kWel [2]; they have also been deployed for larger scale electricity generation (up to 80 MWel) in US data centres of large companies by Bloom Energy [3]. Other types of fuel cells exist and are at different stages of their development, as depending on the end purpose, different types can be used. All fuel cells operate on the same principle (Fig.1-3): two

electrodes, namely the anode and the cathode, convert the fuel and oxygen (O_2) from the air, respectively. The oxygen undergoes a reduction at the cathode, whilst the fuel is oxidised at the anode. The formed ions are transported across an electrolyte, which gives the name to the type of fuel cell. The electrons produced by these electrochemical reactions are conveyed via an external circuit to provide power, with water and heat released as by-products. High purity hydrogen is a base fuel for nearly all fuel cell types. SOFCs have the particularity of being able to convert a wide range of fuels, including hydrogen, carbon monoxide, and hydrocarbons (natural gas, propane...). This is achieved via internal reforming, whereby hydrocarbons are converted to hydrogen and carbon monoxide within the fuel cell, due to the temperature of operation. This internal recycling of heat increases the electrical efficiency of the system. Table 1-1 summarises the different types of fuel cells, and their stage of development, starting with the currently most deployed.

In an SOFC, the oxygen is reduced at the cathode forming O^{2-} oxygen ions as follows:

$$O_2 + 4e^- \rightarrow 2O^{2-} \qquad \text{Equation 1-1}$$

These anions are conveyed to the anode by an ion conductor ceramic oxide (i.e. electrolyte), and hydrogen (or a reformed hydrocarbon fuel) is oxidised at the anode:

$$2H_{2(g)} + 2O^{2-} \rightarrow 2H_2O_{(g)} + 4e^- \quad \text{Equation 1-2}$$

Thus, the overall reaction for an SOFC is:

$$2H_{2(g)} + O_2 \rightarrow 2H_2O_{(g)} \qquad \text{Equation 1-3}$$

In an SOFC stack, single cells are linked by an interconnect, which provides the electrical connection between the cells. There is no commercially available material that meets all the requirements for interconnect applications. Chromium rich steels, as reviewed in Chapter 2, are the most prominent candidates for interconnect applications, due to the ability of

chromium to withstand oxidative attack at high temperatures through the formation of a protective (passivating) chromium oxide layer (Cr_2O_3).

Table 1-1. Overview of fuel cells on the market.

Fuel Cell Name	**Type of Electrolyte** [2,4]	**Fuel Options** [4]	**Operating Temperature Range (°C)** [4]	**Efficiency (%)** [4]	**Typical Application Examples** [2]	**Global Deliveries in 2018 (1,000 Units)** [2]
Polymer Electrolyte Fuel Cell (PEFC)	Polymer Membrane	Pure H_2	50 to 100 High-temperature variant 100-180	45 to 55	Road vehicles and specialty vehicles Residential CHP (Japan)	39.7
Solid Oxide Fuel Cell (SOFC)	Ceramic Oxide	H_2, biogas, natural gas, syn-gas, Ammonia	600 to 950	~50 to 60	CHP, off-grid generators	24.9
Direct Methanol Fuel Cell (DMFC)	Polymer Membrane	Methanol (CH_3OH)	50 to 100	20 to 35	Mobile electronic devices or chargers and portable power packs, APUs	3.7
Phosphoric Acid Fuel Cell (PAFC),	Phosphoric Acid	Pure H_2	160 to 220	55	Stationary	0.2
Molten Carbonate Fuel Cell (MCFC)	Molten carbonate salts	Coal-derived gas, natural gas., Biogas, H_2	550 to 650	55	Large power generation plants (MW capacity)	0.0
Alkaline Fuel Cell (AFC)	Potassium Hydroxide (KOH)	Pure H_2	50 to 90	50 to 60	Space programmes, vehicles	0.0

1.2 The Interconnect Component in SOFC: Functions and Requirements

Prior to the 1990s, SOFC units mostly ran at a high operating temperature range (900 to 1100°C), enabling the internal reforming of fuels, leading to the ability to directly use natural gas. However, the use of such elevated temperatures also meant complex and costly manufacturing methods, restricted and expensive materials options, as well as long-term performance degradation of the stack. Research focused on reducing the range of operating temperatures, as it would allow for the use of cheaper and less complex materials and manufacturing methods.

Various developments contributed to this quest, with a major achievement being the substitution of electrolyte-supported planar SOFC by an anode-supported design [5–7]. This enabled the reduction of the electrolyte thickness from 100 to 200 micrometres to tens of micrometres (10 to 20 µm) [6,8–10] thereby minimising the internal cell resistance [11]. From these accomplishments, a series of component optimisations followed [12–14], and the SOFC operating temperature was lowered to the range of 700 to 850°C [8,11,12]. Recent efforts aim to further lower this range to 500 to 650 °C [13–16].

The interconnect (IC) is an essential component of an SOFC planar stack, which has, in most designs, two main functions: Interlaced between the anode of one cell and the cathode of an adjacent cell, the interconnect provides the electrical series connection between the unit cells. Simultaneously, the interconnect acts a physical barrier between the oxidising anode and the reducing cathode, preventing the direct mixture of the two reactants.

In many designs, the interconnect comprises flow channels (Fig.1-1) which ensure the even distribution of the fuel and oxidant to their respective electrodes.

Figure 1-1. Example of an SOFC interconnect.

Due to these significant functions, the physiochemical requirements for material candidates for ICs are amongst the most exhaustive in SOFC technology, summarised in the list below [7,11,15–18]:

i. As a current collector, the interconnect must have an excellent electrical conductivity (minimum of 10-100 $S.cm^{1}$) and a low area specific resistance (ASR) (<0.1 $\Omega\ cm^{2}$).

ii. The material must have a coefficient of thermal expansion (CTE) compatible to that of the electrodes and electrolyte materials. Yttria Stabilised Zirconia (YSZ) is commonly used for the electrolyte, $LaSrFeCoO_3$ (LSM) for the cathode, and NiO/YSZ for the anode. For this arrangement, the CTE should approximately be 10.5 to $12.5x10^{-6}\ K^{-1}$ in the temperature range 25 to 1000°C.

iii. As a physical separator of the electrode atmospheres, the interconnect must show a good stability (chemical, physical, structural, microstructural and phase stability) across the fuel cell service lifetime (40,000 to 80,000 hours) at associated high operating temperatures (600 to 900°C). Perfect gas impermeability and low porosity is required to prevent leakages and an eventual direct chemical reaction between the reactants.

iv. The interconnect material should have a minimal response to the oxygen pressure gradient $p(O_2)$ to prevent dimensional change and limit mechanical stress.

v. The selected material should show resistance to sulfidation, carbon cementation, and high temperature oxidation to withstand the fuel cell operating conditions.

vi. Finally, as with any commercial endeavour, the interconnect should be low cost & easy to manufacture.

These stringent criteria restrict the list of candidate materials. Ceramic materials were long used as interconnect material. However, following the reduction in operating temperature, ceramic interconnects were replaced by their metal alloy counterparts, as discussed in the following section.

1.3 Interconnect Materials Development

Interconnect materials were initially made from ceramics due to the SOFC operating temperature ranging between 900 and 1000 °C. As the temperature of operation was reduced to 700 to 800 °C, ferritic stainless steels became the material of choice, due to their higher electrical conductivity and better shapability.

1.3.1 Doped Lanthanum Chromite ($LaCrO_3$)

Ceramics are inorganic, non-metallic solid materials, which due to their inherent nature can bear very high temperatures and withstand corrosion in harsh environments. Some ceramics have electrical conducting properties, which sub-classify them as semiconductors. This is the case of Lanthanum Chromite ($LaCrO_3$), a perovskite ceramic oxide (that is of form ABO_3), which has long been used as interconnect material for planar SOFC designs. $LaCrO_3$ is a p-type semiconductor (that is, the electrical current is carried by free electron holes rather than atom vacancies), stable in high temperature oxidising atmospheres, and has a CTE compatible with other ceramic stack components ($9.2x10^{-6}$ K^{-1}) [19]. In its pure form

however, $LaCrO_3$ is not sufficiently conductive for the purpose of SOFC interconnection. As compiled by Fergus [20], $LaCrO_3$ is generally doped with alkaline elements including magnesium (Mg), strontium (Sr), calcium (Ca), nickel (Ni), and cobalt (Co) which all act as electron acceptors and lead to an increased conductivity of the material. Sr reportedly further improved the CTE compatibility of $LaCrO_3$ with the other SOFC ceramic components while Mn and Ca were found to improve its mechanical strength [20]. Challenges mostly arose during manufacturing, due to the high vapour pressure of the volatile chromium components, leading to difficulty in sintering $LaCrO_3$ [21]. This meant that for the different SOFC designs (Fig.1-2) specific $LaCrO_3$ interconnects had to be designed and manufactured, which was seen as problematic and not cost effective [16].

1.3.2 Novelty Ceramic Materials

Following the introduction of metallic interconnects at the end of the 1980's, the interest in ceramic materials for this application considerably decreased with no competing ceramic material being developed. Kendall *et.al* [16] reported that the state-of-the art of ceramic interconnects included lanthanum substitutes, such as yttrium chromites, neodymium chromites and strontium titanates. Whilst having shown encouraging results, these compounds were more manufacturing costly and labour intensive. The in-depth discussion of these materials being outside the scope of this work, the interested reader is referred to references [16,21] for a more comprehensive discussion.

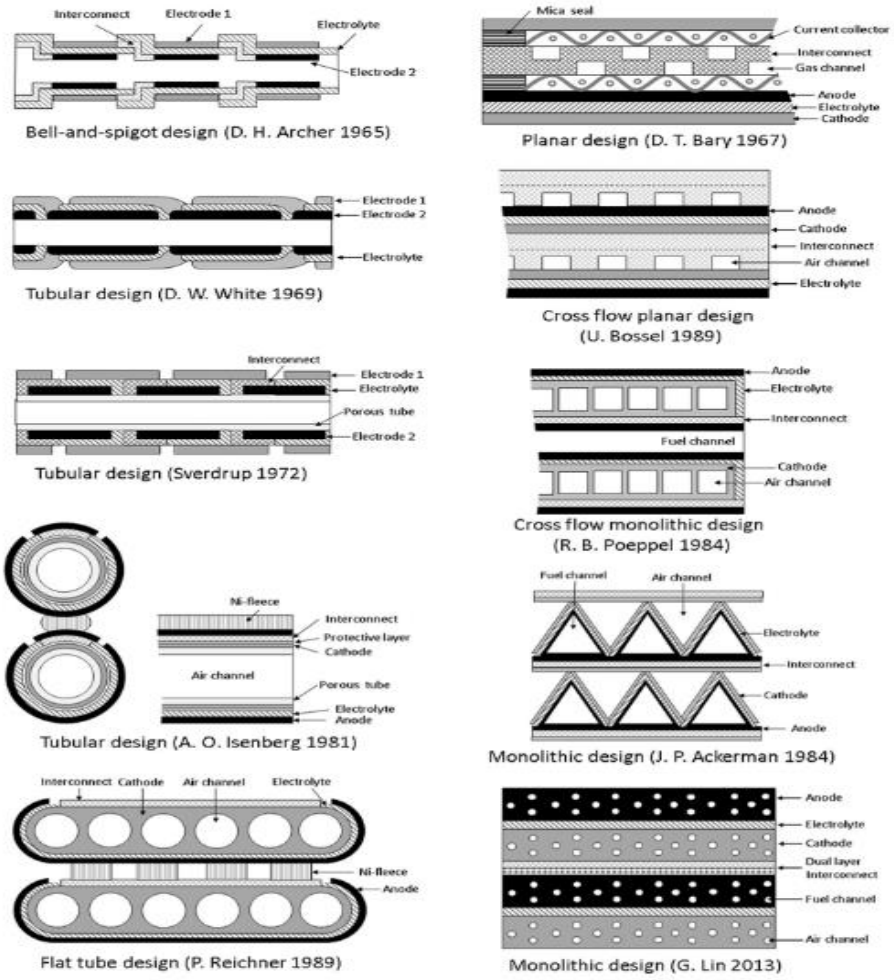

Figure 1-2. Various ceramic SOFC interconnect stack designs [16].

1.3.3 Metal Interconnects

Following the decrease in planar SOFC operating temperatures through improved cell designs, substituting ceramics by metals and alloys appeared as the way forward in the efforts for reducing interconnect manufacturing costs [6,17]. Compared to ceramics, metals and alloys generally offer higher bulk electrical conductivity, greater thermal conductivity, suppression of the thermal gradient across components, larger flexibility for CTE match due to a better ability to accommodate thermal stresses, easier manufacturing and workability, sufficient mechanical strength, and cheaper manufacturing costs [6,7,11,17,21–25]. Precious metals were briefly considered as interconnect (and sealing) materials. Silver for instance,

was evaluated in the temperature range 600 to 800°C under dual reactants (hydrogen/air) atmosphere representative of an SOFC environment [26]. However, these precious metals were rapidly abandoned due to their instability in air/hydrogen dual exposure, which led to porosity and volatility. Additional impediments included their limited availability and unlikely commercial viability [17,21,26].

Metals inevitably form an oxide of the form A_2O_3 upon contact with an oxidising atmosphere. The oxide constitutes a barrier against further corrosion attack from the environment. However, in the case of the interconnect, a continuous growth of the oxide layer contributes to an increase in the interconnect contact resistance, and thus a degradation in performance of the fuel cell. In fact, the ASR (Area Specific Resistance) of an oxidised metal interconnect is largely owned by that of the oxide layer:

$$ASR = 2\tau_o l_o \qquad \text{Equation 1-4}$$

where τ_o and l_o are the resistivity and thickness of the oxide scale, respectively [6]. Since the growth of this oxide scale is inevitable, the current challenge for metallic interconnects is to maintain the interconnect properties during the operating lifetime of the fuel cell by slowing down the oxide scale formation as much as possible. As such, current research focuses on: (i) understanding metallic alloy oxidation kinetics to maintain a slow growth rate of the scale in SOFC operation, (ii) enhancing the oxide conductivity, and (iii) maintaining the scale adhesion and microstructural properties during the anticipated service lifetime of the fuel cell, that is >40,000 h [21].

Initially, three high temperature alloy groups were identified: chromium-based alloys, nickel-based alloys, and iron-based alloys which all form a corrosion protective, yet conductive chromium oxide layer (Cr_2O_3). The oxide formation is induced by the diffusion and subsequent reaction of elemental chromium (Cr) present in the bulk of the alloy with oxygen

(O_2) from the vicinity of the cathode [6,16,17,21,24,27]. Other alloys such as alumina and silica formers, although bearing excellent microstructural properties cannot be considered for interconnect purpose as their oxide scales are electrically insulating.

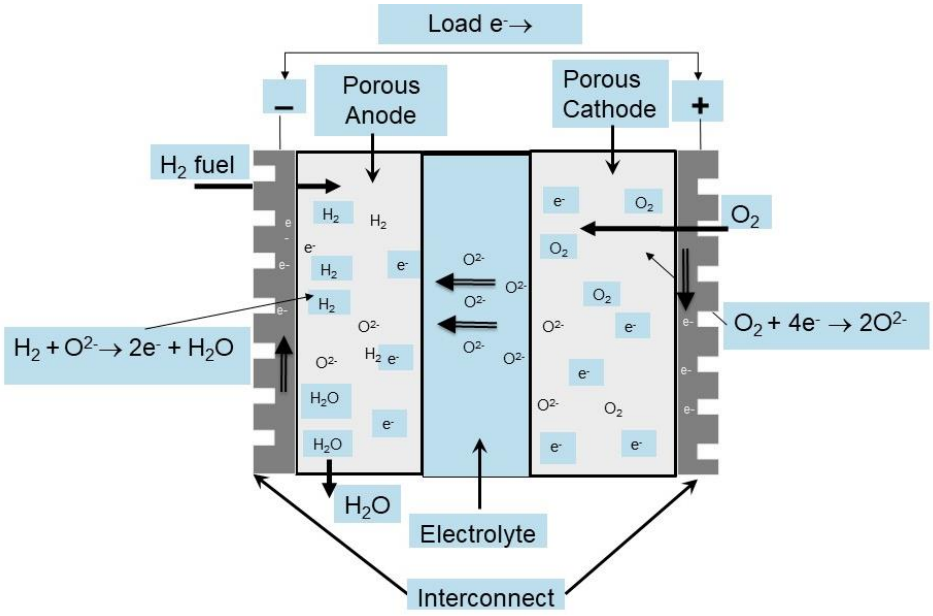

Figure 1-3. Overview of solid oxide fuel cell working principle.

Ferritic stainless steels (FSS) rich in chromium (17-25wt. %) have become the mainstream of interconnect materials. Their crystallographic body centre cubic structure (bcc) has a CTE compatible with that of the SOFC electrode and electrolyte. In addition, these alloys possess good electrical conductivity, are easy to fabricate and display comparatively low cost [21]. Like most metals and alloys, FSSs are unstable in air, and are thus subjected to oxidation attack under high temperature SOFC conditions. While the oxide formed protects the alloy against further oxidation, it further reacts with water molecules and oxygen in air to create volatile chromium species Cr^{6+}. Following volatilisation, these species are known to chemically and/or electrochemically deposit on the triple phase boundary of the porous cathode, deactivating its reactive sites [21,28]. This degradation process, known as cathode

chromium poisoning, results in the shortening of the lifetime of the fuel cell and is thus a key degradation effect to investigate and mitigate.

Protective coatings, heat surface treatments and composition variation constitute the state-of-the-art methods used to mitigate cathode poisoning, by reducing chromium volatilisation, improving the scale adhesion, and enhancing the interconnect conductivity, but there is not much knowledge available on the oxidation of pure chromium at 700°C.

The high life expectancy of the SOFC stack renders long-term experimental studies challenging. As a result, modelling tools and techniques are needed to respond to demands for deeper understanding of processes such as high temperature oxidation of alloys which are experimentally limited. Depending on the scale of the studies, various techniques can be employed, and while numerical studies of super alloy corrosion for aerospace and automotive fields are widely available [29–32], oxidation modelling of conductive steels, in particular chromium rich steels, remains at its beginnings.

1.4 Objectives

The objective of this work is to evaluate the oxidation behaviour of chromium and chromium rich steels under intermediate SOFC operating conditions (700°C) as well as their long-term performance. To do this, the research will aim at:

1. Optimising a methodology to produce low porosity and high-density chromium pellet samples.

2. Improving the understanding of pure chromium oxidation behaviour at 700°C in dry and humidified oxidising environment.

3. Deriving reaction rate constants through the humidified oxidation of chromium rich steels.

4. Modelling the oxide phase formation, oxide growth and chromium depletion in binary Fe17Cr and Fe22Cr systems, leading to the lifetime predicting of the considered systems.

Chapter 2 Literature Review: The Role of Chromium in SOFC Interconnect Development

"Knowledge comes, but wisdom lingers. It may not be difficult to store up in the mind a vast quantity of facts within a comparatively short time, but the ability to form judgments requires the severe discipline of hard work and the tempering heat of experience and maturity" – Calvin Coolidge

2.1 Development of Alloys for SOFC Interconnect Applications

This section briefly reviews alloy candidates for SOFC interconnect applications.

2.1.1 Oxide Dispersed Strengthened Alloys (ODS)

ODS alloys, also known as chromium based alloys (CrBA), are made from rare earth oxides dispersed into chromium rich alloys (>90% chromium content), thus the name, and were initially developed for electrolyte-supported SOFC operating temperatures around 1000ºC [6]. Oxides such as Y_2O_3, La_2O_3, $LaCrO_3$, $LaSrCrO_3$ have reportedly been used to develop ODSs either by elemental mixing of starting powders or by high energy ball milling of the oxides with the alloy [6,33]. These elements are added to improve the oxidation resistance, adhesion of the oxide scale to the substrate, and mechanical properties of the oxide scales grown on these alloys, as well as optimising the particle grain sizes [6,33]. Ducrolloy ($Cr_5Fe1Y_2O_3$) and the chromium-iron-yttria alloy (CFY) are representative ODS alloys, developed by Plansee and Siemens [7,17,23], which showed positive results, including CTE compatibility with the ceramic SOFC materials and good oxide scale adherence [17,27,34]. However, when tested for oxidation resistance and conductivity, these ODS alloys appeared to grow an excessively thick oxide scale layer (for the Ducrolloy for instance, the oxide thickness was approximatively 10 µm after a year of operation) as well as excessively high ASR values just after 75 hours (at 1000ºC) (Fig. 2-1), making them unsuitable for long term stack operation [6,23,27,35]. Following these findings, no further study was published on

ODS alloys for a long time, until a study investigated the long term performance of an SOFC stack with a CFY alloy at 850^{o}C, and revealed a slower degradation rate of 0.7%/1000 hours compared to 1.5 to 1.7%/1000 hours previously obtained at 1000^{o}C, as well as reduced ASR and lower Cr-evaporation than at the higher temperatures [36]. The second drawback, which might have been the most conclusive, was the reported expensive manufacturing cost of ODS alloys, making them less attractive towards mass production of SOFC stacks [17,21,23]. Whilst this may be the case, these alloys have also shown some potential for lower SOFC operating temperatures with the aforementioned lower ASR and reduced volatilisation of Cr species.

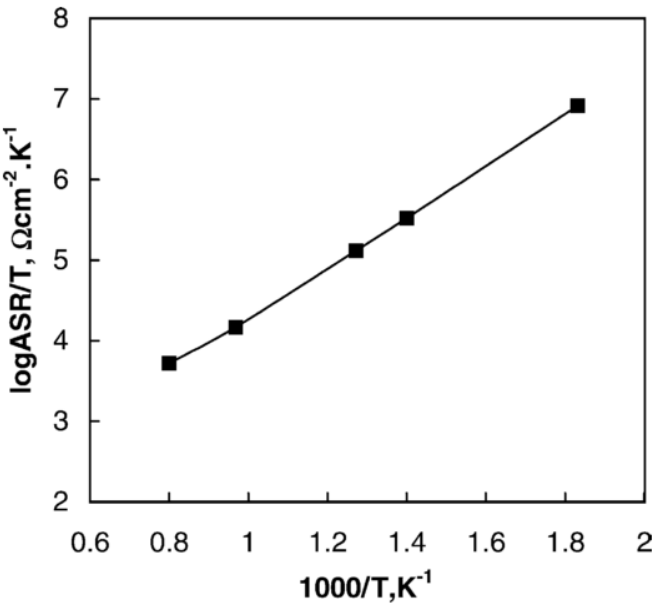

Figure 2-1. Temperature-dependence of the ASR of Ducrolloy oxidised at 1000^{o}C [31].

2.1.2 Nickel (Ni)-based Alloys

Contrary to ODS, nickel-based alloys (NiBSA) consist of a gamma (γ) phase with face-centre cubic crystal structure (FCC) and require a much lower concentration of chromium (15% minimum) in order to form a homogeneous Cr_2O_3 layer. NIBSA have been suggested as

interconnect material due to their higher corrosion and creep resistance, and good mechanical properties. These alloys maintain a satisfactory electrical conductivity at high temperatures, which means that they can withstand the harsh conditions of SOFC operation. However, most nickel alloys (Inconel 600, 625, 718, Haynes 230, R-41, ASL 528, Hastelloy) are not only expensive but have a CTE much higher than that of the other ceramic components of the fuel cell stack (14.0 to 19 $x10^{-6}$ K^{-1} against 9.2 $x10^{-6}$ K^{-1} for $LaCrO_3$). Whilst it was shown that doping the alloys with tungsten (W), molybdenum (Mo), carbon (C), aluminium (Al) or titanium (Ti) could palliate this CTE mismatch [37–39], the results were still not satisfactory for interconnect applications. Jablonski *et al*. [39] thus developed a new series of low CTE nickel alloys (J5, J12 and J13) which were evaluated against the nickel alloy Haynes 230 and ferritic alloy Crofer 22APU (Table 2-1.).

Table 2-1. Chromium nominal composition and experimental CTE values of nickel alloys, Haynes 230 and J5 compared with ferritic stainless steel Crofer 22APU (reproduced from [29]).

	Haynes 230	J5	Crofer 22APU	Reference CTE value ceramic FC components
[Cr] wt.%	22	12.5	22	-
CTE ($x10^{-6}$ °C)	14.7	12.6	11	12

Jablonski *et al*. [39] findings showed that the oxidation resistance of Haynes 230 in air + 3% H_2O was superior to that of J5 and Crofer 22 APU. However, the sub-scale cross section of Haynes 230 showed the presence of aluminium, which is detrimental to the electrical properties of the scale. The mechanical properties of Haynes 230 and J5 alloys were not much affected by the elevated temperature, where J5 ductility and strength were favourably

comparable to Haynes 230 [39]. In theory, provided that the CTE of these alloys can be adjusted to match those of the electrodes and electrolyte, nickel alloys like J5 have a potential for interconnect applications. Long-term experiments including ASR testing of these materials and cost effectiveness would be required.

2.1.3 Stainless Steels

Stainless steels (FeBAS) are steels to which chromium (Cr) is added. A minimum of 11% of chromium content [40] is necessary to form the self-healing protective and conductive chromium oxide layer (Cr_2O_3) in ambient conditions, and at least 17% is required at high temperatures (>500°C) [33] thus obtaining the 'stainlessness' of the steel. Because the chromia formed from stainless steels contains resultant impurities from the manufacturing process, stainless steels reportedly have a higher contact resistance (that is, lower conductivity) than their Ni-Cr alloy counterparts, which in addition also offer better oxidation properties [6,21,41]. However, stainless steels are attractive because their CTE values are closer to the ceramic components of the SOFC in the temperature range 600 to 900°C which can be further improved by alloying.

2.2 Chromium for SOFC Interconnect Applications

In this section, chromium, key constituent in stainless steels developed for SOFC interconnect applications, is introduced. A review of the suitability of the stainless steels developed as interconnect materials, alongside their most common manufacturing methods will be given.

2.2.1 Chromium Alloying

Chromium metal (Figure 2-2.) is a steel-lustrous grey transition metal mined as chromite ($FeCr_2O_4$) ore, which is then roasted and leached into metallic chromium. Added to steel, chromium forms an oxide layer of the form $Cr_{2-x}Fe_xO_3$ (where x is virtually zero for

chromium-rich alloys) on its surface [42,43]. The formation of this oxide is referred to as passivation because of its uniformity and protectiveness against corrosive environmental conditions; indeed, chromium oxide (Cr_2O_3), is insoluble in acids and alkali. Chromium has several properties (high melting point, high reactivity and high evaporation rate of molten chromium) which make its melting difficult, which complicates traditional machining of steels.

Table 2-2. Density and melting point of chromium.

Properties	Units	Value
Density	$g.cm^3$	7.19 at 20°C
Melting point	°C	1907

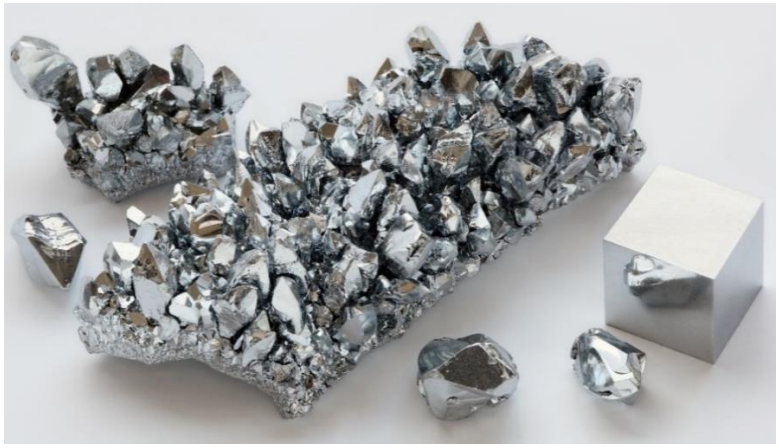

Figure 2-2. Raw chromium crystals (left) and fabricated cube (right) [44].

2.2.2 Stainless Steel Manufacturing

Traditionally Machined Stainless Steels

Stainless steels are traditionally obtained through a sequence of steel melting, alloying and alloying in furnaces and casting into a desired shape and size for use in the downstream markets.

Figure 2-3. Worker pouring molten steel in cast [45].

During these processes, microstructural changes occur, leading to different crystallographic specificities of the obtained solid solutions: austenitic, martensitic and ferritic steels. From these microstructures, six types of steel have been developed: (1) ferritic stainless steels (FSS), (2) austenitic stainless steels (ASS), (3) martensitic stainless steels (MSS), (4) duplex stainless steels (DSS), (5) precipitation hardened steels, and (6) manganese-nitrogen (Mn-N) substituted austenitic stainless steels [46]. FSS, ASS and MSS have been suggested as materials for SOFC interconnects. These steels are reviewed below and summarised in Table 2-3:

i. Austenitic stainless steels (ASS) are the most produced type of steels (50% of the world's steel production is of austenitic type). The austenite solid solution is obtained by heating a Fe-Ni alloy above 750ºC and subsequently cooling it, leading to an FCC crystalline structure [40]. Different grades of ASSs exist, such as high temperature ASSs, developed for the temperature range exceeding 550°C. Whilst the Cr content of these steels is similar to that of ferritic steels (17-25%), they contain more nickel (8-20%), which improves their oxidation resistance for application around 800°C. In addition, their high carbon content results in good malleability and strength. However, several features diminish their viability for interconnect applications: firstly, they have the highest CTE amongst stainless steels (15 to 18 x 10^{-6} K^{-1}) in the temperature

range 25°C to 1000°C [17,39,47] but are also prone to carbon dusting (formation of carbides in the alloy) in hydrocarbon containing environments, because of their solubility and diffusivity for carbon, as revealed by Toh *et al*. [48] and Grabke [49] Finally, the presence of nickel shifts ASS to the higher end cost wise [24].

ii. Contrary to ASS, martensitic stainless steels (MSS) are the least produced category of steels [50]. They are obtained by rapid cooling of an austenitic solution, during which carbon is trapped in a somehow distorted matrix giving these steels a body-centre-tetragonal (BCT) microstructure known as martensite [51,52]. MSSs such as the popular AISI 410 steel typically contain 12-15% of chromium, a 'good combination of mechanical properties' and very little Ni [52]. However, due to their lower chromium content, they do not compare to FSS and ASS in terms of corrosion resistance. As such, they are most commonly used for high temperature applications where moderate oxidation resistance is required. No studies reported their suitability for SOFC interconnects, but their maximum service temperature before large amount of scaling was reported as 650°C, which suggests that they are unsuitable for operations above this temperature [17,53].

iii. Ferritic stainless steels (FSS) are traditionally obtained through slow cooling of austenite, resulting in a body-centre-cubic (bcc) crystallographic structure. FSS vary in chromium content, but the ones that have been developed and commercialised for SOFC interconnect purposes contain between 17% and 28% of chromium [33]. These steels possess good ductility, workability and lower cost compared to ODS alloys and ASS [21]. However, they contain very little carbon (≤0.015%, thus the ferrite microstructure) and as a result have less strength [17]. This can however be improved by annealing, where the metal is heated and cooled slowly, which has the effect of strengthening it [40]. Ferritic steels are reportedly as corrosion resistant as ASS [50]

and their ASR results show higher electrical resistance compared to ODS alloys, mainly due to the presence of Fe impurities. Similarly to ceramic interconnects, ferritic stainless steels are alloyed to improve their properties; manganese, a key element, is added to reduce the formation of volatile chromium species by forming oxides of spinel type (i.e $MnCr_2O_4$, $MnCrO_3$) above the chromia passivation layer; molybdenum and tungsten are added to enhance the CTE compatibility [24]; silicon, added in small amounts, is thought to improve the corrosion resistance of the steel. The use of FSS for high temperature SOFC comes with its challenges: an excessive growth of the chromium oxide scale, which in turn leads to an increase of the contact resistance, and SOFC cathode poisoning through volatilisation of chromium species.

Table 2-3 Comparison of high temperature alloys for SOFC interconnect applications [17].

Alloys	**Matrix structure**	**TEC x10^{-6} K^{-1} at 800°C**	**Oxidation resistance**	**Mechanical strengths**	**Manufacturability**	**Cost**
CrBA	Bcc	11.0-12.5	Good	High	Difficult	Very expensive
FSS	Bcc	11.5-14.0	Good	Low	Fairly ready	Inexpensive
ASS	Fcc	18.0-20.0	Good	Fairly high	Ready	Inexpensive
FeBSA	Fcc	15.0-20.0	Good	High	Ready	Fairly expensive
NiBSA	Fcc	14.0-19.0	Good	High	Ready	Expensive

Despite these minuses, FSS are currently favoured as planar SOFC interconnect materials, thanks to their outstanding CTE compatibility with the ceramic electrode and electrolyte

materials of the fuel cell, easiness to fabricate with shape flexibility, potential for microstructural development, and lower cost [21].

Powder Metallurgy Production of Stainless Steels

Over the last decade, powder metallurgy (PM) of metallic interconnects has emerged as an advantageous and easier alternative method to traditional machined stainless steels [54]. The manufacturing method, already used since the 1940s to produce stainless steel components (martensitic, austenitic and ferritic stainless steels), has been increasingly and successfully used to fabricate metallic interconnect plates including Ducrolloy (Cr-$_5$Fe-1Y_2O_3) and Crofer 22, producing near-net shape products with fast production rates, specific properties, reduced costs, less machining steps and scrap materials [55–61]. PM of stainless steels generally consists of four primary operations as shown in Fig. 2-4: (i) powder mixing where the elemental powders are either simply blended in mixers or pre-alloyed by melt atomisation through water or gas jet, (ii) compacting of the powder mix into a die of desired shape and size at a chosen pressure, and (iii) sintering of the pellet and further machining into parts [62]. Sintering is at the centre of this manufacturing method, whereby the alloy powder particles are heated in a reducing atmosphere to create solid-state bonding and strengthening between the powder particles [63].

The composition variation of ferritic alloys developed for interconnect purposes across the years is summarised in Table 2-5. Type 441/K41 is an economic ferritic stainless steel (17-18% chromium content by weight) which has showed improved oxidation resistance compared to lower grade ferritic stainless steels, such as 409, 439 and 439 [64]. However, when tested for long time operation at 850°C in a typical SOFC cathode side atmosphere (air + 3% H_2O), its corrosion performance was deemed insufficient [65], due to its high silicon content and absence of reactive elements (RE). Other developed Fe-Cr alloys not mentioned

in Table 2-5 include ZMG232 G10 (Hitachi Metals) and E-Brite (ATI Allegheny Ludlum) which both exhibited substantial Cr volatilisation during oxidation tests at 850°C making them highly unsuitable for interconnect purposes [66]. Currently, the most commonly used ferritic steel is Crofer 22H, a successor of Crofer 22APU, both manufactured by Thyssenkrupp VD. Compared to other ferritic steels, the Crofer type contains La, which was shown by the manufacturer to improve the steel oxidation resistance and oxide scale adhesion in both oxidising and reducing SOFC atmospheres at 800°C [67]. With the service life for a fuel cell stack expected to exceed 80,000 hours, more steels with slow oxidation kinetics and high strength need to be developed and tested.

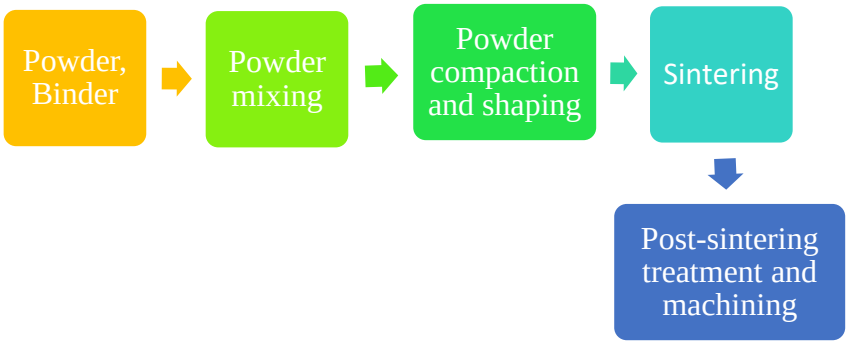

Figure 2-4 Chart of the general PM process route.

2.2.3 Sinterability of Chromium Powder

Sintering, defined as the forming of materials from metals/ceramic powders applying thermal energy, aims to create solid-state bonding and strengthening between the powder particles, thereby increasing the material compact strength [61,62]. Sintering involves heating to a temperature below the melting point of the main constituent of a pressed pellet (known as a green compact) and is sometimes carried out in a reducing atmosphere (hydrogen, dissociated ammonia, vacuum and sealed containers) to minimise oxide formation and limit impurities,

and to remove existing oxides, lubricants and binders used in pelletising. Sintering of stainless steels is normally conducted between 1150 and 1300°C.

Two main types of sintering methods may be acknowledged: solid-state sintering and liquid phase sintering (which includes reactive and activation sintering). In the latter, different phases are incorporated to improve the densification of the material, increase the sintering rate and improve the particle bonding. Solid-state sintering, the most commonly used approach for metals and alloys, does not necessitate any substance addition aside binder and lubricant as the sintering process occurs through self- atomic diffusion (for a single component system) caused by capillary forces and surface tension existing between the powder particles [68]. On a microstructural level, the process takes place in different steps, as illustrated in Figure 2-5. Initially, particles bond at contact points, which grow into 'necks' by diffusion, creating rounded pore interconnections between the particles. These pores reduce in size, which may cause shrinkage of the green compact depending on its density obtained after pelletising. With the pores reducing, grain boundaries develop between the necks, and strength, density, ductility and thermal and electrical conductivities of the green compact increase. Powder parameters and process variables affecting the properties of the sintered products are summarised in Table 2-5.

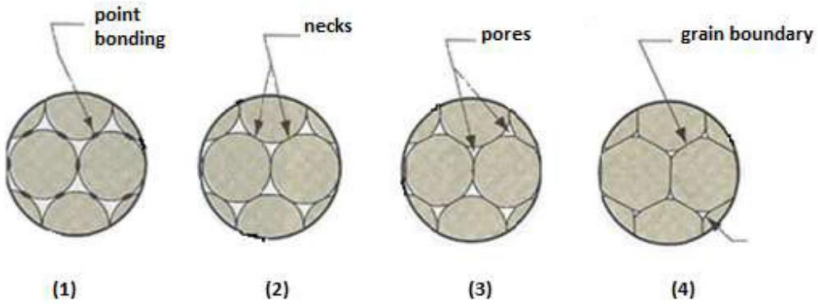

Figure 2-5. Sintering stages at a microscopic level [69].

The theory of sintering was first proposed by Sauerwald [70,71] , who described the process as a two-step mechanism, involving (i) adhesion followed by (ii) recrystallisation of the

powder particles. Sauewarld [71,72] explained that adhesion of the particles is due to the atomic attraction, whilst recrystallisation, which causes microstructural changes such as shrinkage, takes place at the recrystallisation temperature, which should be at least half of the melting point (T_m) of the sintered component [71,73].

Table 2-4. Powder parameters and process variables influencing the sinterability of alloys [32,74].

Process Variables	Compaction pressure, sintering temperature, pressure heating and cooling rate, sintering atmosphere, removal of binders/lubricants.
Powder Parameters	Stable particle structure, particle size distribution, no agglomeration, powder composition (lowest possible oxide content), low impurities concentration.

Until recently, studies have mainly focused on the sinterability of austenitic steel powders [74]. Only few studies have been conducted on the sintering behaviour of pressed stainless steel powders, which highlighted the affinity of chromium for oxygen and thus the need for a suitable sintering method [74].

Sintering of stainless-steel powders aims to impart strength in the compacts, by increasing their density. However, sintering of chromium alloyed steels has proven to be difficult and published literature scarce, due to the formation of chromium stable oxides and carbon diffusion during slow heating [75,76]. Once formed, the layers of oxides and the diffusion of the carbon present can hinder sintering by preventing the development of necks during heating to the sintering temperature [75,76]. In addition, sintered chromium powder is known to be brittle. Bouscaren studied [76] the sinterability of chromium at 1200°C where he

reported the brittleness of sintered chromium, which he linked to the presence of carbon and nitrogen. The author concluded that rapid heating (approximately 20 minutes but not less) hindered the diffusion of carbon and this was beneficial to the sintering process. The author also investigated the effect of porosity on the compacts, where he found that higher porosity effectively led to the interparticle and intergranular recrystallisation theorised by Sauerwald [71], observable by the presence of coarser interconnected pores [76].

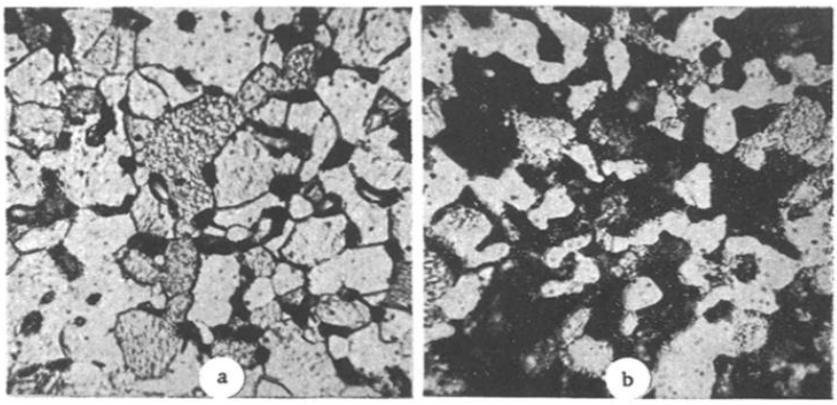

Figure 2-6. Micrographs of sintered chromium with (a) 15% and (b) 40% porosity *[76]*.

Table 2-5. Composition of developed ferritic steels for SOFC interconnects.

Alloy	**Concentration (wt. %)**																**Reference**
	Cr	Fe	C	N	S	Mn	Si	Al	W	Nb	Ti	La	P	Ni	Cu	Mo	
Crofer 22 APU	20-24.0	bal.	0.03	-	0.02	0.30 to 0.80	0.50	0.5	-	-	0.03 to 0.20	0.04 to 0.20	0.05	-	0.5	-	[52]
Crofer 22H	20-24.0	bal.	0.03	0.04	0.006	0.30 to 0.80	0.10 to 0.60	0.1	3.0	1.00	0.20	0.04 to 0.2	0.05	0.5	0.5	-	[51]
Sanergy HT	22.0	bal.	-	-	-	≤0.50	≤0.30	-	-	0.75	0.75	-	-	-	-	1.0	[53]
AISI 441/K41	17.5-18.5	bal.	≤0.30	-	≤0.015	≤1.00	≤1.00	-	-	0.4 to 1.00	0.10 to 0.60	-	≤0.04	-	-	-	[49]
460FC	22.3	bal.	0.007	-	-	≤1.00	0.09	-	-	≤ 0.5	?	-	-	-	-	-	[54]

2.3 Metallic Interconnect Degradation

This section introduces the thermodynamic science which underlies the mechanisms of oxidation and subsequent oxide growth observed in high temperature alloys in SOFC operation. The current understanding of the degradation mechanisms which affect chromium rich alloys is reviewed.

2.3.1 Thermodynamic Fundamentals

The foundation of protection for high temperature alloys is rooted in the Gibbs free energy (G) [77] (which describes the available energy in a chemical reaction which can be used for work. For the chemical oxidation of a metal (M), the formation of oxide MO_2 can be described as:

$$M + O_2 = MO_2 \quad \text{Equation 2-1}$$

where O_2 is the oxidant.

The change in Gibb's free energy, which dictates the likelihood for a chemical reaction to occur, is generally written as:

$$\Delta G = \Delta G^{\emptyset} + RTln\frac{a_{MO_2}}{a_M a_{O_2}} \quad \text{Equation 2-2}$$

where $\Delta G^{\emptyset}$ (kJ/mol) is the free energy of the species at standard conditions, R is the gas constant ($J.K^{-1}.mol^{-1}$), a_i is the thermodynamic activity of this species, that is the ability to participate in a reaction, and T is the temperature (K). It follows that if:

- ΔG is negative ($\Delta G < 0$), the reaction is said to be thermodynamically possible.
- ΔG is positive ($\Delta G > 0$), the reaction is said to be thermodynamically impossible.
- ΔG is null ($\Delta G = 0$), the system is in a minimum energy-state termed equilibrium, and no further reaction can occur.

The oxidation of most alloys (with exceptions like Mn in Fe, or Fe in Cu) has a non-ideal solution behaviour for which activities *a* rather than concentrations are used. This is due to the fact that the metal is not in its pure condensed phase, therefore its activity is reduced.

As the reaction proceeds, the energy gradient which provides the driving force for the reaction will decrease to zero, known as the equilibrium point to which an equilibrium constant *K* is associated, given in Eq. 2-3. The activities of the metal and its oxides are generally taken as unity, while that of the oxygen is taken as its partial pressure.

$$K = \frac{a_{MO_2}}{a_M a_{O_2}} \frac{1}{p(O_2)} \quad \text{Equation 2-3}$$

where $p(O_2)$ is the oxygen partial pressure.

Finally, it follows that the standard Gibb's free energy of formation of most alloys may be written as:

$$\Delta G^{\emptyset} = -RTln\frac{1}{p(O)_2} \quad \text{Equation 2-4}$$

The partial pressure, also known as the dissociation pressure, is a useful indicator of the stability of oxides as used in the Ellingham diagram, plotting the standard Gibb's free energy against a range of temperatures for various oxides (Fig. 2-7). It follows from the graph that the value of $\Delta G^{\emptyset}$ increases as the temperature increases, such that oxides become less stable and are more prone to reaction; this is due to the entropy (amount of disorder in a system) which increases as the reaction proceeds, leading to oxide instability.

Base metals Fe, Ni and Co therefore have highly unstable oxides (also the higher the dissociation pressure, the less thermodynamically stable is the oxide) as compared to elements Cr, Si, Al […] which are significantly more stable. These elements, when added to the base metals, form a stable oxide which protects the alloy by selective oxidation. Above

the dissociation pressure $p(O_2)$, the oxide will remain stable and provide a continuous protective layer, whereas a decrease below $p(O_2)$ would result in the dissociation of the oxide.

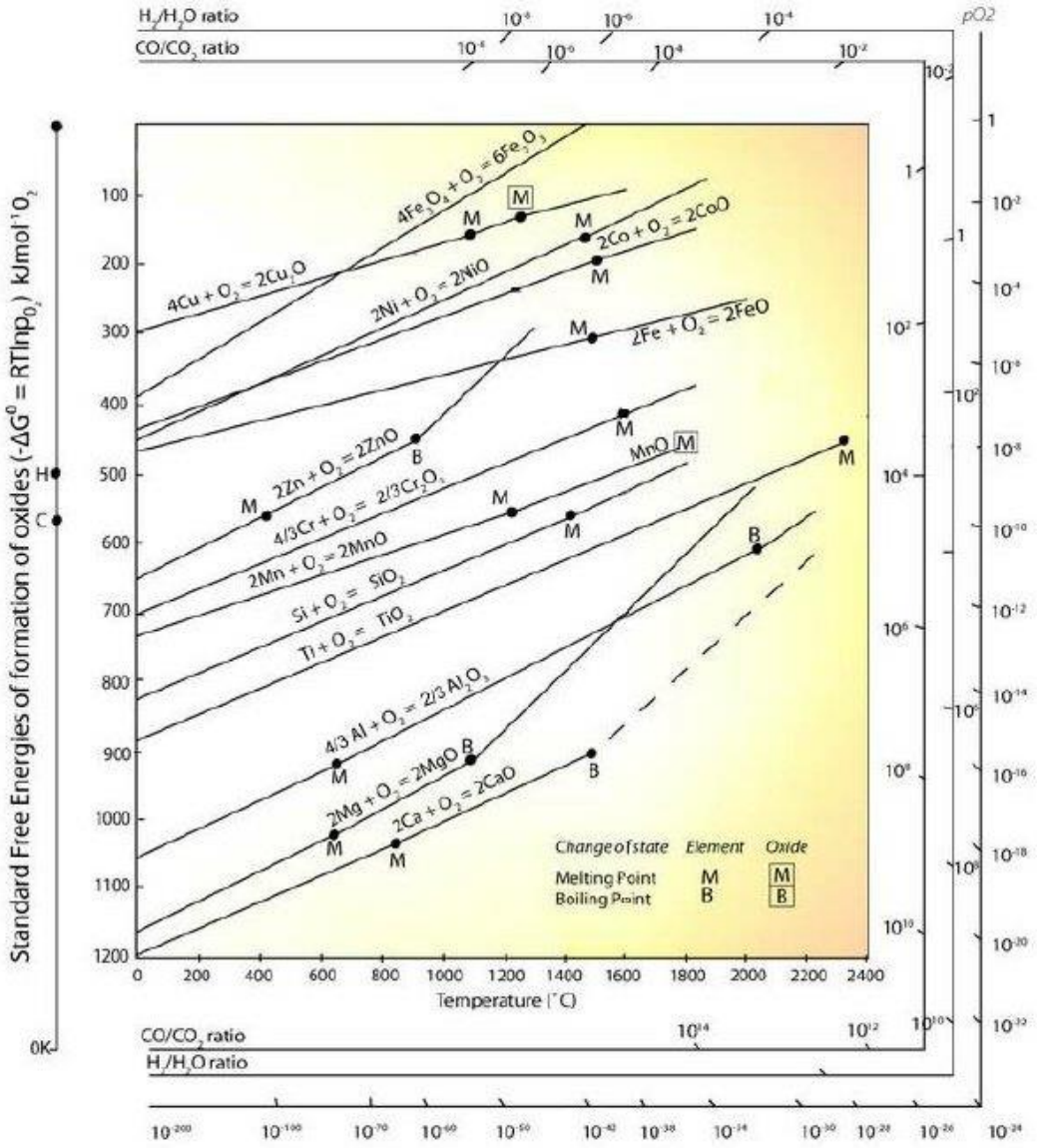

Figure 2-7. The original Ellingham diagram [78].

2.3.2 Oxide Scale Formation

The idea of a protective oxide scale growing on an alloy implies that a preferential oxidation of a component takes place. More generally, oxides of all active components (including the base metal) may initially simultaneously form, which is not the case for selective oxidation. Considering an oxide-free alloy surface consisting of a base Metal M and an alloying element

B exposed to an oxygen rich environment, the selective oxidation of B (that is, the preferential oxidation of solute B over metal M) takes place in three stages illustrated in Figure 2-8.: Oxide nuclei formation, formation of a continuous oxide layer, and finally growth of the layer, as comprehensively summarised by authors [79–83].

Providing that the oxygen partial pressure is sufficiently low and that the base metal shows enough solubility for the oxidant gas, oxygen molecules adsorb onto the metal surface. These molecules dissociate into oxygen atoms, which dissolve into the external surface of the base metal lattice. As the dissolution occurs, a concentration gradient develops.

When the equilibrium concentration for oxidising the solute element B, which is chromium in the case analysed in this thesis, is reached, a reaction occurs on 'random' nucleation, marking the beginning of the oxidation.

$$2Cr_{(s)} + \frac{3}{2}O_{2_{(g)}} = Cr_2O_{3_{(s)}}$$ Equation 2-5

Oxide nuclei of the form BO_n precipitate from the solid solution and grow along the so-called internal oxidation zone. This process, known as 'internal oxidation' marks the initial oxidation of the alloy where the rate limiting procedure is the oxygen adsorption [80,84]. Cr_2O_3 polycrystalline nuclei consisting of several individual crystals cover the surface, forming a homogenous oxide layer [85,86]. Two categories of oxides are hence distinguished: the n-type and the p-type oxides. In the n-type oxides excess metal or cations are conducted, electrical charges are conveyed by electrons in the conduction band, while in the p-type oxides, excess anions are conducted via electron holes in the valence band. This also determines the direction of scale growth and depends on the type of defects (atom vacancies) found in the oxide crystal structure.

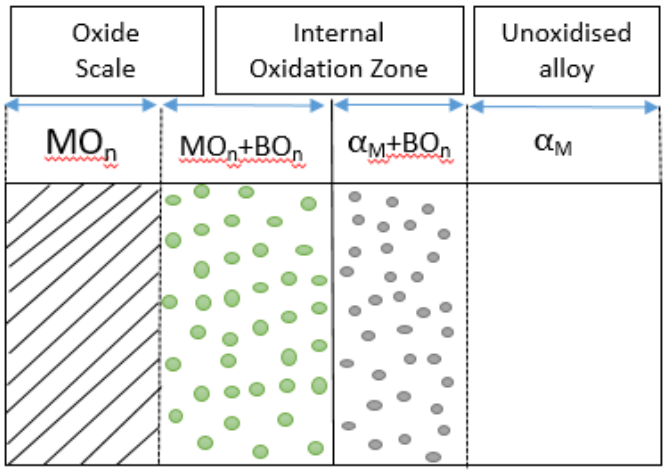

Figure 2-8. Schematic diagram of outward growth of external oxide scale (drawn, not to scale).

2.3.3 Oxide Scale Growth: Solid-State Diffusion

The two reactants are now separated by a dense thin film. A porous film is not out of the question, but unusual for chromia forming alloys; The adherence of oxide films is defined by the Pilling-Bedworth ratio (PBR) (which is the ratio of the volumes occupied by the metal and its corresponding oxide) [87]. The PBR of selected elements was reported in Table 2-6. Metals such as magnesium (Mg) with a PBR<1 will form a porous non-protective oxide prone to spallation and cracking, whereas chromium, with PBR of 1.99 is destined to form a protective scale [87]. Since metals and alloys are made of atoms bound together in an ionic crystal lattice, any further growth of this scale is only possible through solid-state diffusion of either cationic (metal) or anionic (oxygen) ions through the oxide film layer [88].

Table 2-6. Pilling–Bedworth ratio PBR of selected elements (extracted from [87]).

Element	**Oxide**	**PBR**
Ca	CaO	0.64
Mg	Al_2O_3	0.81

Al	Al_2O_3	1.28
Pt	PtO	1.56
Fe	FeO	1.70
Mn	MnO	1.79
Cr	Cr_2O_3	1.99
Co	CoO	1.99
Fe	Fe_2O_3	2.10
Si	SiO_2	2.15

Diffusion in a system is defined as the process by which macroscopic quantities flow from a high concentration region to a lower concentration region of that system by means of random molecule motion. Thus, for a binary system of molecules A and B where the concentration of molecule A is higher on one side (Figure 2-9), random thermal motion causes the molecules A to flow in the direction of the lower concentration, until the species concentration is uniform throughout the system.

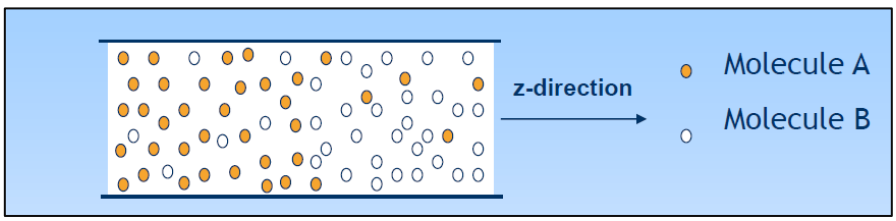

Figure 2-9. Schematic diagram of a diffusion process (drawn, not to scale).

Metals and alloys are made of atoms bound together in a crystal lattice. The lattice contains imperfections, known as defects, in which atoms can jump. Diffusion in solids is thus due to the presence of these inherent defects, including point or lattice defects, line defects, and

surface defects [89]. These in turn cause different diffusion mechanisms, namely lattice diffusion, grain boundary diffusion, and surface diffusion.

Lattice diffusion, also called volume or bulk diffusion, is the result of two types of defect sites, as pictured in Figure 2-10:

- Interstitial defect sites, where two atoms are temporarily dislocated to allow the diffusing atom to jump from one interstitial site to its neighbouring site. The temporary distortions of the moved atom define the energy barrier (activation energy) needed to be overcome by the diffusing atom.
- Vacancy defect sites, where the atom jumps over its nearest vacancy creating less distortion as compared to interstitial sites. However, since the energy to create a vacancy needs to be accounted for, the resulting activation energy may be as high as that of interstitial sites.

Experimentally, lattice diffusion can be measured via isotope tracers (to measure self-diffusion of crystal components), electron probe micro-analysis (to measure the penetration and diffusion of foreign ions), or sectioning methods.

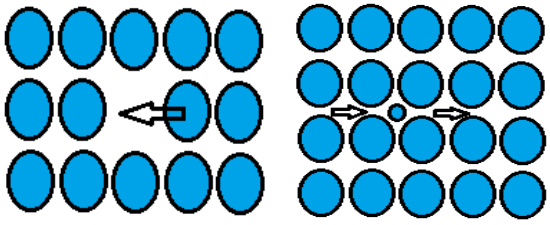

Figure 2-10. Vacancy (left) and interstitial (right) defects diffusion (drawn, not to scale).

Grain boundary and dislocation are terms used to designate the interface between two grains of crystallites in a polycrystalline material where a lattice ‘mismatch’ is observed. Grain boundary diffusion is a faster process in polycrystalline materials, due to a lower activation

energy as compared to that needed for lattice diffusion. This type of diffusion is difficult to experimentally analyse as qualitative measurements are not easily obtained. Line and surface defects can be responsible for diffusion. In fact, it is generally believed that grain boundaries, dislocations and surface diffusion are faster processes in polycrystalline materials as compared to lattice defects [80]. Grain boundary diffusion has been proposed for chromia scales due to incoherent boundaries between the oxide nuclei (that is the grain boundaries), exhibited by the polycrystalline structure of Cr_2O_3 scales at high temperature. Analysis of diffusion profiles is often the method used in investigating the growth mechanism of chromia scales [90]. Upon diffusion through and oxidation of polycrystalline Cr_2O_3 and alloys in specific conditions, diffusion coefficients are determined both in the bulk (D_b), and along the grain boundary (D_{gb}) and oxidation kinetics curves are established.

Diffusion in solids is much slower than in liquids and gases, which means that the analytical tools required are more sensitive. This explains the relative lateness in diffusion studies in metals and alloys (end of 18th century); Balogh and Schmitz [91] share that diffusion in metals and alloys remains a complex subject, translated by a lack of diffusion data for many metallic systems. Grain boundary diffusion paths, for example, were only acknowledged in the late 1900s, and although certain grain boundary diffusion coefficients have been calculated, interdiffusion within the grain boundaries is still itself poorly understood. Yet, this diffusive path is believed to be predominant in the case of chromia forming alloys [90,92,93]. Anionic diffusion will lead to a scale growth inward towards the metal, while a cationic diffusion will lead to an outward scale growth.

Diffusion in solids underpins a range of processes of long-term stability and aging of materials, which should motivate further research. Compiled knowledge can amongst others be found in [91,94,95]. Early studies of growth mechanism of Cr_2O_3 scales were somehow contradictory. Whilst Kofstad *et.al* [85] and Lillerud *et.al* [86] found that bulk diffusion of

chromium ions was dominant over oxygen diffusion in Cr_2O_3 polycrystals, Sabioni *et.al* [96] reported higher oxygen ion bulk diffusion coefficients compared to chromium ions.

In an effort to clarify these opposing results, Tsai *et.al* [90] analysed the diffusion profiles of a Ni70-Cr30 alloy at temperatures between 800°C to 900°C, investigating both bulk and grain boundary diffusion. The authors found that the bulk diffusion coefficients of oxygen and chromium were similar, while along the grain boundaries, chromium ions diffused faster than oxygen ions. Tsai's D_{gb} values however, do not agree with Sabioni's *et.al* [96,97] and Wood [79] but are closer to Lobnig's work [98]. All cited authors, except Sabioni, found that both in the bulk and along the grain boundary, the diffusion of chromium ions was faster than that of oxygen. So far thus, the majority of the research in this area, though scarce, has concluded that the growth of the chromia scale is mainly due to the outward diffusion of chromium from the steel. These discrepancies in diffusivity values echoed on the reliability of tracer diffusion experiments, with no recent published studies on the topic.

2.3.4 Chromium Volatilisation

The growth mechanism of Cr_2O_3 is based on key factors such as the composition of the alloy and its manufacturing method, the solubility of O_2 in the alloy, the environmental conditions (temperature and oxygen partial pressure), and the concentration of the alloying elements. Under high temperature, the chromia scale is oxidised by the cathode air into chromium (VI) gaseous species, either chromium trioxide (CrO_3) in dry atmosphere, and chromium oxyhydroxide ($CrO_2(OH)_2$) in humid atmosphere, as given below [6,99]:

$$2Cr_2O_{3_{(s)}} + 3O_{2_{(g)}} = 4CrO_{3_{(g)}} \qquad \text{Equation 2-6}$$

$$Cr_2O_{3_{(s)}} + \frac{3}{2}O_{2_{(g)}} + 2H_2O = 2CrO_2(OH)_{2_{(g)}} \qquad \text{Equation 2-7}$$

These Cr (VI) volatile gases are the source of three degradation mechanisms, which result in long term degradation of interconnect and cathode components, inducing in turn the decreased performance of the SOFC stack:

a. **Poisoning of the cathode:** as the Cr volatile species come into contact with the cathode of the SOFC, the cathode active sites get poisoned [16,100–102]. This topic is an active area of research, as diverging opinions have emerged on the mechanism of deposition of these gases on the cathode (Figure 2-11). Park *et al.* [103] studied the cathode contamination for different cathode materials (LSM, PrSM, NdsM and BSCF). Their findings indicated that for all but the NdSM cathode, chromium deposited near the cathode/electrolyte interface. The authors supported the mechanism of reaction between the chromium vapour and oxygen vacancy observed on the YSZ electrolyte, facilitating the chromium deposition. Hart *et al.* [104] focused their work on the composite LSM/YSZ cathodes, showing the decomposition of the cathode material was due partly to the reaction of Cr (VI) with Mn_3O_4 as well as the reaction of Cr (VI) with the LSM phase, both reactions forming the spinel oxide $MnCr_2O_4$. They also reported less oxygen reduction at the triple phase boundary. Temperature variation has been investigated by many authors. Supported by studies by Jiang *et al.* [28], it is generally accepted that increasing the operating temperature has the effect of increasing the degradation of the cathode materials via the increasing volatisation of chromium species. Yet, Windisch *et al.* [105] recently reported that decreasing the temperature would only decrease the degradation by a factor of 2 (operating temperature range of 650°C to 800°C). Further studies by Kaun *et.al* [106] and Kim *et al.* [107] reported an increased cathode degradation with decreasing temperature from 800°C to 700°C, while Paulson [102] even recorded cathode degradation at temperatures as low as 600°C. These paradoxical findings critically point out the

relevance of temperature as a reliable variable for influencing cathode poisoning. Nevertheless, it needs to be pointed out that different SOFC cathode compositions will result in different reactions with chromium species and therefore degradation rates. This underpins that temperature alone is only one of the decisive factors.

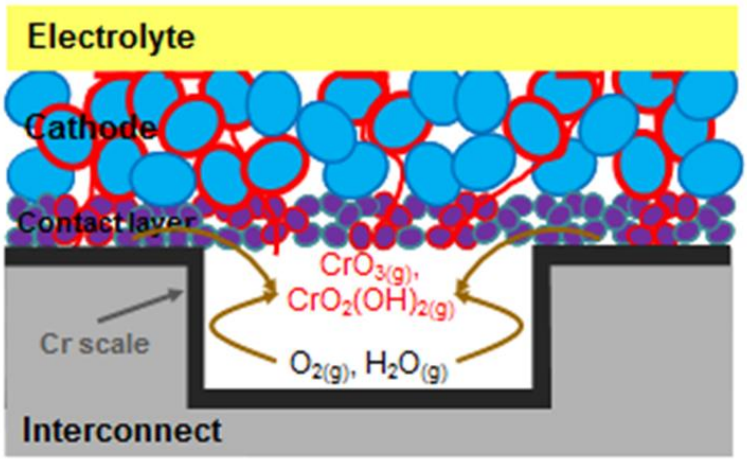

Figure 2-11. Schematic diagram showing chromium species volatising to the cathode from the interconnect oxide scale (drawn, not to scale).

b. **Increased ASR:** the Cr_2O_3 scale can grow to micrometres thickness during the service lifetime of the stack. Thickening of the scale induces a considerable increase in ASR, hence reducing the performance of the fuel cell. Öztürk *et al.* [55] compared the ASR of PM prepared and wrought crofer 22 APU (Figure 2-12), and found that even though the ASR of PM prepared samples was initially higher (40 $m\Omega.cm^2$), it stabilised to the machined Crofer 22APU sample values (below 15 $m\Omega.cm^2$) after 500 hours, in agreement with other studies [81–83].

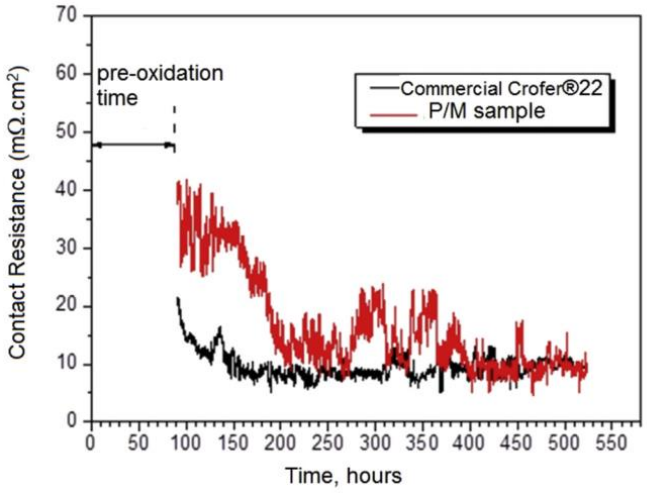

Figure 2-12. ASR ($m\Omega.cm^2$) values of the PM and wrought Crofer 22APU samples at 800°C in air [55].

c. **Depletion of chromium reservoir:** This degradation has received less attention than the cathode poisoning, mainly because it spreads over years of operation [21,111]. The formation of the volatile chromium gases is only possible through the oxidation of the chromia scale formed on the interconnect alloy. This leads to a depletion of the alloy chromium reservoir to regenerate the oxide layer and prevent its spallation or breakaway; as the chromium deficiency grows, a less protective scale may be formed leading to an increased corrosion rate [111].

2.3.5 Mitigation Methods

Various methods have been developed to reduce the vaporisation of chromium species and control the oxidation kinetics of scales grown: protective coatings, surface treatments and alloy development. Comprehensive reviews of these methods may be found in [37,47].

To be effective, applied coatings should (i) reduce oxide growth kinetics, (ii) increase oxide scale conductivity, (iii) improve oxide-metal adhesion, and (iv) retain volatile chromium from diffusing out of the scales [37]. Four categories of coating materials have been developed: reactive element oxides (REOs), conductive perovskites, MAlCrYO coatings and

spinel coatings, which are considered the most promising, due to their ability to mitigate Cr volatilisation. Spinel coatings are composites of general formula AB_2O_4 where A and B are cations in octahedral and tetrahedral sites [47]. Manganese-cobalt (MnCo) and copper manganese oxide (CuMnO) are prevalent coating systems and can be deposited using different methods (magneton sputtering, electroplating, and electrophoretic deposition, wet powder spraying, thermal spraying, and chemical vapour deposition). In fact, $CuMnO_4$ has reportedly shown the highest obtainable electrical conductivity, 225 Scm^{-1} at 750°C [112]. Doping MnCo with Cu on the other hand showed improved sinterability, electrical conductivity, and TEC match, followed by $MnCo_2O_4$ (60 Scm^{-1} at 800°C) [112]. Grolig *et al.* [64] claimed that applying a reactive element based coating also led to a decrease of chromium volatilisation. Based on this knowledge, Sandvik Materials technology developed Sanergy Sandvik HT steel (SSHT) containing zirconium. Oxidation studies carried out at 850°C [111] and 750°C [113] demonstrated that the addition of cobalt (Co) and cerium (Ce) coatings improved the oxidation resistance of the SSHT steel by growing a Co-rich spinel oxide on top of a $(Cr, Mn)_3O_4$ oxide. However, at 750°C, mass loss was prevalent due to chromium evaporation, as early as 500 hours, making it unsuitable for intermediate temperature operating SOFCs.

2.4 Modelling

In the present work, modelling and simulation have been used to predict the oxidation behaviour of selected ferritic stainless steels under experimental SOFC conditions. This section reviews modelling techniques which have been used in SOFC and their applicability to the endeavoured work.

2.4.1 Introduction to Modelling and Simulation

In general, experimental studies in SOFC primarily aim at developing materials and fuels, whilst numerical studies focus on the physico-chemical processes, as well as the electrochemical phenomena occurring inside the stack. This enables a deeper insight into the cell's components, - via the simulation of processes, the investigation of individual aspects of these processes, and the prediction of material behaviour - while offering a certain flexibility and manoeuvrability on parameters and variables, which is difficult to achieve through experiments only. As regards the life expectancy of high-temperature SOFCs (>80,000 hours), real-time experimental testing of interconnects could be a time-consuming endeavour. High temperature accelerated testing methods are often used instead to predict the service lifetime of interconnects but are thought to affect the phase stability, oxidation mechanisms and kinetics of alloy-coating systems, compromising the reliability of the method [114]. Combining experimental and numerical studies is thus an effective approach to maximise the results of research (Figure 2-13.).

Modelling is the idealised mathematical translation of a real physical process. Simulation on the other hand, is the model in operation, whereby variables and constraints are input and varied to study the response of the modelled system. Simulations and experiments are used as model validation techniques, where we simulate the model under known input conditions and compare the model output with the system's experimental results [115].

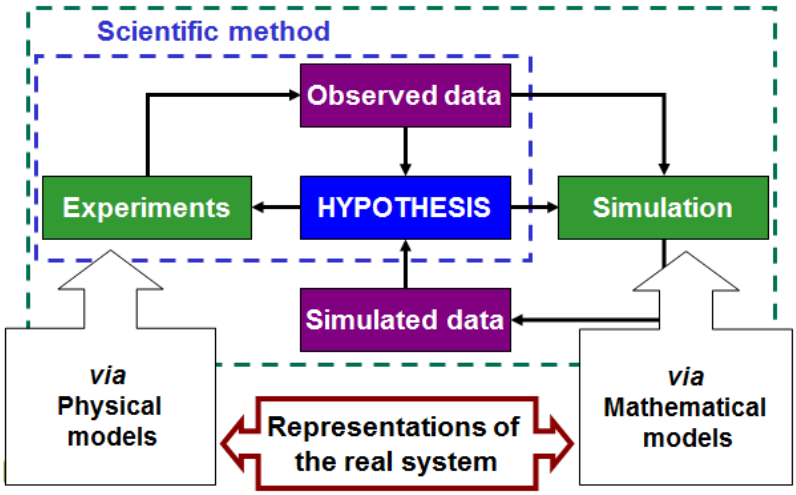

Figure 2-13. Schematic diagram of modelling and simulation methodology [115].

2.4.2 Modelling Approaches Relevant to SOFC Interconnects

Modelling has long been used throughout the development of SOFCs to support material design and process optimisation. Modelling for SOFC applications can be loosely divided into two categories, which correspond to whether a stack is considered (cell-to-cell and stack modelling), or whether processes are analysed at a more localised level. Cell-to-cell and stack modelling are perhaps the most encountered type of studies in the fuel cell community. These models are mostly concerned with cell performance, fuel utilisation and stack response to various changes (i.e. design, materials, reactants and/or operating conditions) [116–119]. The models often start with geometrical representations of the system in zero to three dimensions which embody the computational simulation of the processes occurring by means of electrochemical and transfer phenomena equations, considering mass, heat, or momentum transfer within the cells. Numerical methods, including finite differences (FDM), finite element (FEM), finite volume (FVM), collocation methods, or marching schemes are normally used to numerically solve the governing equations of the concerned processes [120]. The aim of these models is to picture the system performance in terms of voltage, current density, temperature, velocity and reactant and product concentrations as functions of

time and space [119]. In the past decade, comprehensive reviews of these types of models have been published, addressing planar and tubular SOFC configurations [117,119,121]. They mostly reported results on polarisation losses, mass/energy/momentum/charge conservation, transport and diffusion through porous media, and electrochemical phenomena, as well as reactions in the positive-electrolyte-negative (PEN) assembly. Practically, these models are often built using Computational Fluid Dynamics (CFD) supported packages such as COMSOL, ANSYS Fluent, STAR-CD or MATLAB-SIMULINK which are used for both model conception and simulations.

While the information collected through mathematical modelling is valuable in terms of cell optimisation and stack design, local processes such as degradation mechanisms occurring within the cell, which often play an important role for the overall performance of the unit, are often grossly simplified, if even not represented at all. However, another class of modelling study exists, known as Computational Thermodynamics and Kinetics (CTK). CTK models aim to analyse local phenomena occurring in the fuel cell components [120,122]. These models regroup a wider range of approaches, again dependent on the time and length scale of the mechanism's studies, and have been used to study various SOFC degradation mechanisms:

i. ab initio molecular dynamics (MD) and ab initio methods (such as Density Function Theory (DFT) Ab Initio), which are concerned with the electronic structure of atoms and their interaction. Main focus has been on catalyst and electrode poisoning, redox reactions as well as electrolyte conductivity [123–129];
ii. Molecular Dynamics and Monte Carlo methods: similarly to the above, physical interactions of atoms are used to simulate electrolyte ion exchange and conductivity, and anode poisoning using ab initio and statistical modelling [51,128–131];

iii. Discrete element and phase field methods: these have been used to model microstructural evolution of SOFC electrodes and electrolyte [132–135];

iv. Lattice Botlzmann method (LBM): this approach uses microstructural and mesoscopic data to simulate fluid flow and its averaged macroscopic behaviour [136]. In SOCF, LBM has found its use in modelling the physics of fluid flow in the anode as well as the electrochemical performance of the whole SOFC [137–139];

v. Finite Element, finite volume and finite difference methods (FEM, FVM, FDM) are numerical approximation methods, whereby differential equations representative of processes are solved [117]. The methods differ by the approach undertaken to generate solutions: whilst FDM predicts point values of a solution by using time and spatial discrete points as a basis, FVM involves solution-averaging within specific control volumes. FEM, for its part, uses finite-sized geometrical elements to approximate solutions from sets of obtained discrete values.

vi. CALPHAD (Coupling Phase Diagrams and Thermochemistry) method described in section 2.5.4, is potentially an insightful, phase-based approach which has not been widely used in the fuel cell community as yet. Darvish [140] analysed the formation of sulphur dioxide (SO_2) in LSCF cathodes and Povoden [141,142] completed a thermodynamic assessment of chromium-oxygen (Cr-O) and lanthanum-chromium-oxygen (La-Cr-O) compounds for SOFC;

As previously mentioned in Section 2.4 of this chapter, the oxidation of chromium alloys entails the diffusion process of reactive elements, the growth of the oxide, and the evaporation of chromium gases. Figure 2-14. and Fig. 2-15 outline the time and length scale characteristics of degradation mechanisms in SOFC and subsequent modelling and simulation methods. As the figures show, corrosion processes fit in the mill-seconds/metres range; however, if defects and grain boundaries are included, the length and time scale can extend to

the nano range. First-principle calculations (ab initio, DFT), MD, MC and phase field simulations have not extensively been used to treat diffusional and oxidation problems of reactive element in steels. Finite differences and CALPHAD methods accounted for the most published works and are reviewed in the next two sections.

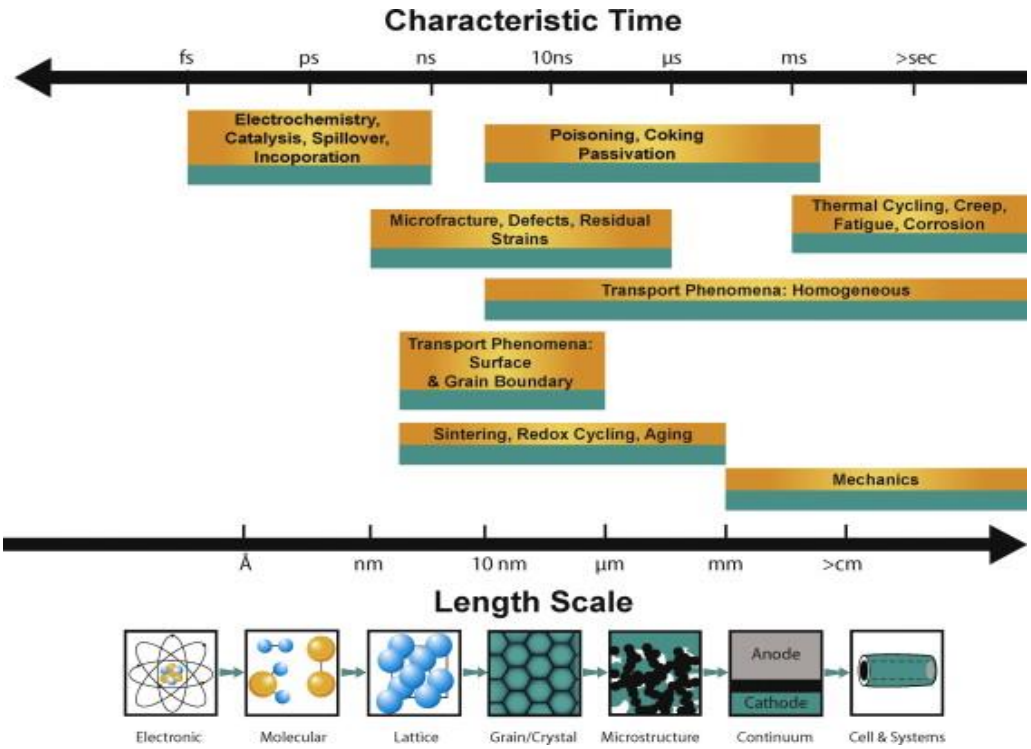

Figure 2-14. An overview of the time and length scales characteristic of functional and degradation processes in SOFC systems [119].

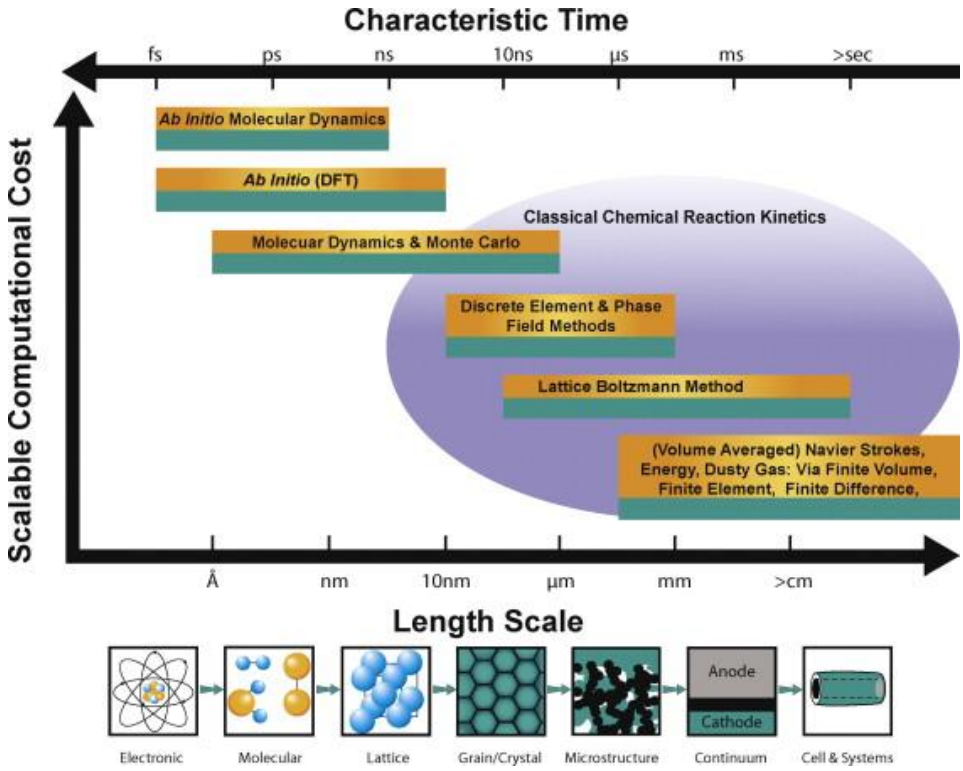

Figure 2-15. Various modelling and simulation methods applicable for the SOFC [119].

2.4.3 Finite Differences

The pathway to the mathematical understanding of metal and alloy oxidation was paved by Carl Wagner's theory of parabolic oxidation rate [143] elaborated in the early 1930s. Considering a diffusion-limited growth of an oxide on a metal at high temperature, Wagner assumed that a local equilibrium was established at the oxide/metal interface. This was based on the idea that the component concentration either side of the interface was that needed to create a phase equilibrium and was valid if a steady-state growth of the oxide prevailed. This assumption enabled him to predict a parabolic time-dependence of the oxide thickness as shown in Eq. 2-8. It also allowed for the straightforward calculation of a parabolic corrosion constant, self-diffusion coefficients, as well as the magnitude, temperature, and oxygen partial pressure dependencies for the oxidation of copper (Cu), nickel (Ni), cobalt (Co), and iron (Fe). Parabolic oxide growth is given by the following relationship:

$$x = \left(2k_p t\right)^{1/2} \qquad \text{Equation 2-8}$$

where x is the oxide thickness, k_p is the parabolic corrosion constant, and t is time.

This theory, whilst still generally accepted, is however limited due to the fact that most alloys do not simply obey a parabolic law where a local equilibrium prevails at the oxide/alloy interface, mainly because the concentration of the oxidising alloy is likely not to be constant as assumed by Wagner, but rather a function of time elapsing. This was firstly shown by Whittle *et al*. [83], who developed the first alloy diffusion-oxidation numerical model involving the use of the finite difference method on a spatial domain. In this well-known approach, the diffusion differential equations of unknown points of a time and spatial continuum are approximated by difference quotients known as finite differences (see Chapter 4 for a more in-depth description). The resulting algebraic equations propagate the solution forward from one-time row to the next in a step-by-step fashion.

Whittle *et al*.'s [144] precursor work investigating the high temperature (>1000°C) oxidation of Ni-Cr, Fe-Cr, and Fe-Al alloys showed that for different oxidation rate constants, other rate laws, including linear, logarithmic and cubic could prevail, resulting in different concentration profiles in the alloy (Fig. 2-16). Similarly, several experimental studies showed that in practice, purely parabolic growth of Cr_2O_3 is rarely observed due to either stress accumulation in the scale, resulting in spalling or slower grain boundary diffusion [24,145–148].

The simulated calculation of reactant concentration profiles at the oxide/alloy interface in Whittle *et al.'s* work [144] (Figure 2-16 and Figure 2-17) showed a sharp decrease during initial oxidation for all rate law scenarios. This is explained by the fact that the maximum outflow of reacting species occurs during the early stages of the oxidation reaction. The authors also showed the importance of four constants affecting the concentration profiles,

which should thus be realistically chosen in a simulation: (i) the ratio ξ, (=k_p/D) (where D is the diffusion coefficient of the diffusing specie) must be selected such that the concentration of the selective oxidising species at the oxide/alloy interface never drops to zero, as this concentration is crucial to the ongoing oxidation behaviour of the material, (ii) the dimensionless position of the alloy/oxide interface at time zero, η, chosen such as the oxidation rate does not tend to infinity at time zero, (iii) the ratio of the oxide molecular volume to the atomic volume of the alloy or Pilling-Bedworth ratio, δ, (iv) the ratio of the concentration of reactant in the oxide to that in the bulk alloy, ε, particularly in the case of chromia forming alloys. However, this model was built with the assumption of a constant diffusivity (i.e. the diffusivity is independent of the alloy compositional changes), which is unlikely to be true for most metals and alloys due to the concentration and temperature dependency of this parameter [149].

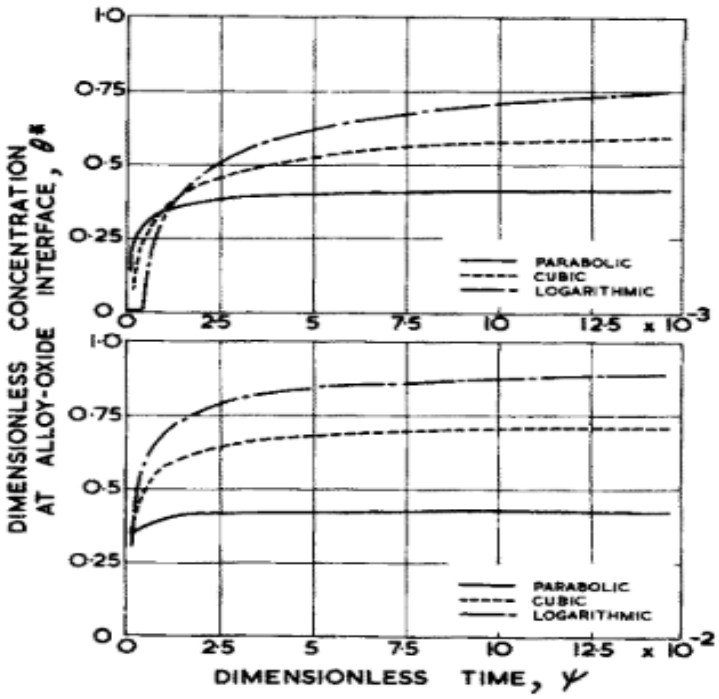

Figure 2-16. Dimensionless concentration of A at the alloy/oxide interface as a function of dimensionless time for different rate laws [144].

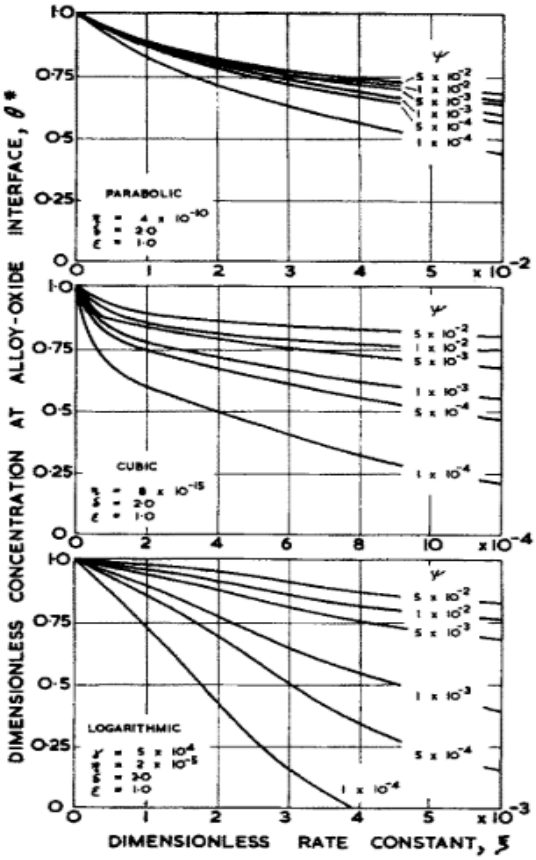

Figure 2-17. Dimensionless concentration of A at the alloy/oxide interface as a function of oxidation rate ξ for different laws [144].

Yet, during the 25 years following the pioneering work of Whittle *et al*. progress in modelling slowed, probably in anticipation of more computer power. In 2000, Nesbitt [29] employed finite differences coded in FORTRAN and created COSIM (Coating Oxidation and Substrate Interdiffusion Model), an innovative one-dimensional model investigating diffusional interactions between a protective coating (MCrAl where M is nickel, but can be substituted for Co or Fe) and a superalloy, suffering thermal cycling oxidation, as schematically represented in Figure 2-18. This work was novel in that in addition to using finite differences for diffusion modelling, the authors accounted for the spallation of the alumina (Al_2O_3) layer, caused by thermal cycling. As such, a spalling model was developed, predicting the rate of Al consumed during each cycle [29], which served as an input to the assumed parabolic kinetics of the diffusion-oxidation problem. In addition, the concentration

dependency of the diffusion coefficients was accounted for through polynomial expressions of the coefficient derivatives. However, the model did not account for a spinel and other oxide formation arising from Cr diffusion.

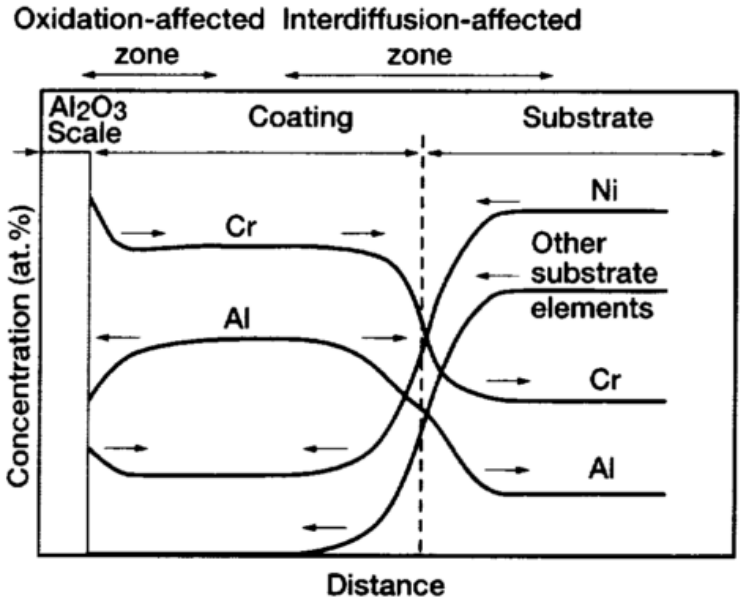

Figure 2-18. Concentration profiles after oxidation exposure and diffusional transport [29].

Krupp *et al*. [150] modified the Nesbitt method to predict the time/number of thermal cycles before the cracking of an alumina oxide scale grown on Ni-base superalloys, by making use of the stress model developed by Evans *et al.* [151], as well as finite differences coupled with thermodynamic data available in the software library ChemApp. Their COSP model (Cyclic Oxidation Simulation Program) defined the time of failure as the transition from external to internal oxidation, leading to the formation of a non-protective oxide. Similarly, Nijdam *et al*. [152] built a one-dimensional model for the oxidation of a ternary alloy system, applied to the oxidation of a y-NiCrAl alloy. The model coupled the use of thermodynamic modelling via Thermo-Calc software (to determine oxide phase formation, chemical potential gradients, and activities) with finite difference for diffusion modelling to determine the composition-depth profiles in the alloy and amount of oxide phase formed over time. Whilst the diffusivity remained constant, this model, by accounting for system phase equilibria showed, just like

Whittle *et al.*'s work the importance of the initial growth of the oxide, often rapid. The authors reinforced that the rate of oxidation at early stage (taken in this case as a combination of cubic and linear oxidation rates) determines the phase composition of the developing layer, leaving a parabolic rate to govern an already established, steady-state alloy composition (Figure 2-19.) [152].

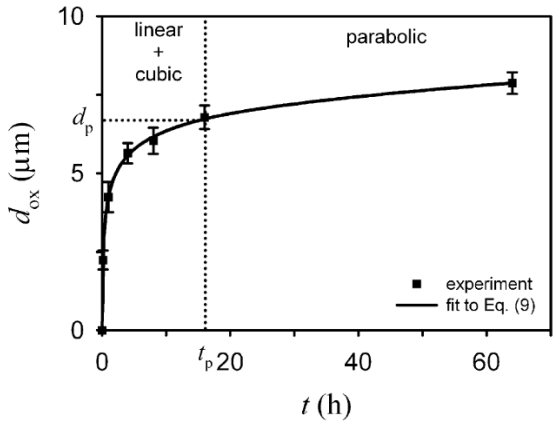

Figure 2-19. Measured and predicted α-Al_2O_3 oxide layer thickness as a function of oxidation time for the thermal oxidation of a γ-Ni27-Cr-9Al alloys at 1200ºC and pO_2=2x10^4 Pa [152].

Pragnell and Evans [30] then used this knowledge to analyse 2-D ribs and corners geometries. The authors created ODIN (Oxidation, depletion and interdiffusion), another depletion model for the selective oxidation of a component in a FeCrAlY ternary alloy, again using a power law to define the oxide growth. However, unlike Nesbitt's COSIM model, oxide spallation and recession of the oxide/metal interface were assumed to be negligible. In addition, the concentration dependency of the diffusivities was not accounted for. This did not prevent the authors to satisfactorily compare their results with experimental oxidation tests. Fig.2-20 shows a comparison of predicted and measured Al depletion profiles on different regions of the FeCrAlY alloy during up to 72 hours of oxidation in air at 925°C [30]. With a reasonable fitting trend, the authors highlighted the enhanced depletion suffered by the edges, proving the possibility of more localised prediction. Equally importantly, this work emphasised the importance of experimental validation.

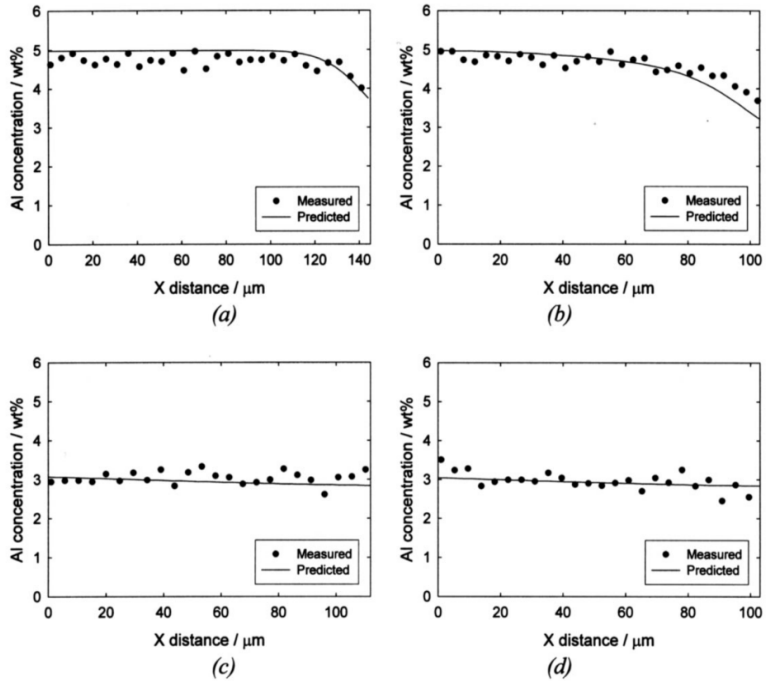

Figure 2-20. Experimentally measured and numerically predicted Al depletion profiles at 900°C after 2 hours (a) along mid-plane, and (b) into section corner, and after 72 hours (c) along mid-plane, and (d) into section corner [30].

Models discussed so far essentially describe non-concentration dependent cases, i.e. constant diffusivity of species. However, in the case of chromium, studies have shown that grain boundary diffusion is much faster than lattice diffusion [85,86,90], resulting in a quicker depletion of chromium concentration underneath the oxide layer and explaining the diffusivity dependency on concentration. To account for grain boundaries, an effective diffusion coefficient is often used, which is an average of both lattice and grain boundary diffusion. Hanson *et al*. [153] examined the influence of grain boundary diffusion in a rather sophisticated 2-D model, based on a control volume–based finite difference solution of Fick's 2nd law, in which the mesh used incorporates grain boundaries perpendicular and parallel to the alloy/oxide interface. However, their approach was to pair the grain boundaries to interdiffusion and self-diffusion coefficients obtained experimentally, as based on the Fisher type model [154] rather than using effective coefficients.

Figure 2-21. shows the Cr depletion profile (from a ternary FeCrNi alloy isothermal oxidation) obtained from the model compared to that of a 1-D Wagner analytical solution. As the figure shows, the two profiles are very different, as the former increases with the temperature, the latter decreases. Cr content at the oxide/alloy interface in the 2-D model is higher after 692 hours of oxidation than at 346 hours, which according to the authors is explained by the fact that at high temperatures, the distance between oxide/alloy interface and the grain boundaries are shorter leading to higher diffusivity, while at lower temperatures, slow bulk diffusion overtakes effective diffusivity. This diffusivity, like in the previous papers, was assumed to be constant. The discrepancy with Wagner's model was not explained and no experimental data was included for comparison.

Generally, a finite difference method is the preferred route for the macroscopic modelling of alloy diffusion and oxidation and has more recently been coupled with the use of thermodynamics and kinetics developed databases and programmes. Published work remains scarce for SOFC interconnect alloys but the applicability of the approach has been proven.

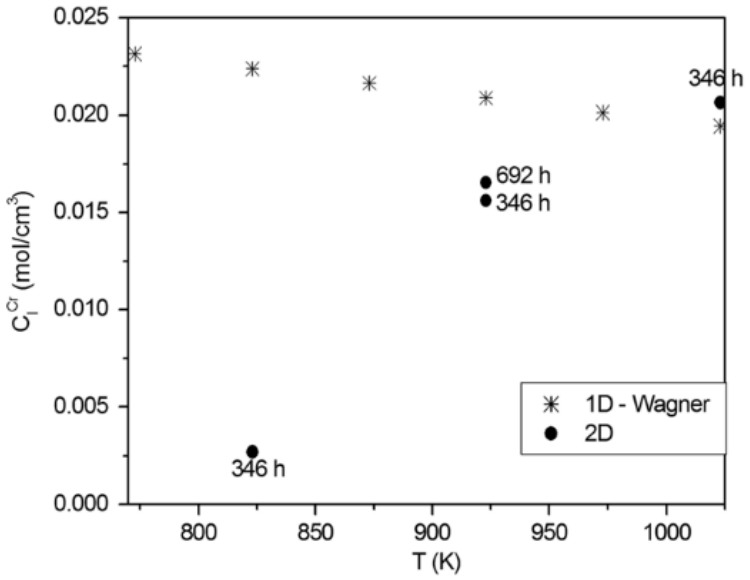

Figure 2-21. Calculated Cr at the alloy/oxide interface using Wagner 1-D analytic model [30].

2.4.4 CALPHAD

The CALPHAD method originated in the 1970s through a great contribution of the SGTE (Scientific Group Thermodata Europe). CALPHAD is a phase-based method, which models the underlying thermodynamics and phase equilibria of a system through the use of self-consistent databases containing compiled phase thermodynamic and kinetic data of elements and compounds [155]. By definition, a phase is a part of a system having a homogenous composition and is physically different from other parts of the system. Phase diagrams can then provide extensive information on a system by graphically describing the relationships between variables (temperature, pressure, etc.) and composition and thus allow the prediction of phase transformation in multicomponent alloys. Due to the complexity of most alloys, experimental construction of even partial regions of such diagrams can be laborious.

As a process proceeds, the system evolves from an unstable to a stable state known as the equilibrium. This stability is measured using the system's Gibb's free energy (G), defined as:

$$G = H - TS \quad \text{Equation 2-9}$$

where H is the enthalpy, T the temperature in Kelvin and S the entropy of the system.

At equilibrium, the system will aim to minimise its Gibb's energy to the lowest possible value ($dG=0$). Phase diagrams, therefore, are generated by total Gibb's energy minimisation of each phase (for constant values of temperature, pressure, mole or weight, or site fraction of components). In the CALPHAD method, the overall aim is to generate a description of the system through modules able to calculate complex homogenous and heterogeneous phase equilibria and thus allow the prediction of multicomponent system properties [122]. Several software packages combining a self-consistent framework - such as SOLGAS, Thermo-Calc, FACTSage, MTDATA, GEMINI, HSC, Pandat, Workbench, and JmatPro - have been developed towards these ends [156]. The information gathered in the form of phase diagrams,

phase stabilities, or mobility can then be used to perform kinetic simulations of various kinds (inter-diffusion in compound materials, interdiffusion in coating/substrate compounds, growth or dissolution of individual particles, homogenisation of alloys, etc.) using developed software programs such as DICTRA, MICRESS and PrecipiCalc [156]. Among these, the Thermo-Calc/DICTRA software package has emerged as the leading tool for materials modelling and simulation of alloys where Thermo-Calc is used as the basis of DICTRA. Throughout the years, Thermo-Calc has continued to develop its abilities releasing a new generation of the software in 2013 [157]. DICTRA's development dates from the 1990s, but the simulation software was only integrated in Thermo-Calc in 2014.

As with finite differences, published CALPHAD work related to SOFC metal interconnects remains scarce, mainly because of insufficient data having been compiled for metals and oxygen diffusion through a chromium oxide scale, impeding the kinetic simulation of oxidation. Computational methods are limited in that few software programmes can address the problem, and developing databases is a long-term task which is yet to be completed. The approach that has been generally taken consists in combining different tools, interfaces and techniques in order to maximise efficiency.

Yuan [32] carried out the modelling of Al depletion from a MCrAlY (here being CoNiCrAlYSi) coating deposited onto nickel base alloys in both isothermal (900, 1000, 1100°C) and thermal cycling (100 to 1000°C) conditions. This was based on an oxidation-diffusion model developed using MATLAB & DICTRA. The model incorporated modelling of surface oxidation and coating-substrate inter-diffusion to predict the useful life of MCrAlY coatings. The diffusion was simulated by using a homogenisation model from the DICTRA software, following a trial - and - error series of various homogenisation models. A diffusion blocking effect in the coating and at the coating/interface (by pores and internal oxides), usually modelled by changing the diffusion coefficients in the coating and substrate, was

integrated by modifying the simulated diffusion time (up to 5000 hours). The Al depletion near the surface of the alloy was modelled simply via Wagner's parabolic law. The homogenisation model gave good prediction on the composition profiles upon diffusion, especially using the 'rule of mixture' (sub-model selection in DICTRA). Similarly, the predicted formation of an OBDZ (outer-β-depletion zone) and IBDZ (inner-β-depletion zone) was in accordance with experimental results, where β was found to be a dominant phase. The results showed that considering the diffusion blocking effect gave more accurate results, closer to the experimental observations. For example, the calculated β phase consumption without the diffusion blocking occurred too fast compared to the experimental results.

This study was limited by the sole account for alumina growth, excluding other oxide formation, impact on the microstructure and life-time service of the coatings, as well as a straight assumption of parabolic growth. While the parabolic growth is in theory valid for metals and alloys, it does not accurately represent the growth rate of real systems, and more development is needed in order to use the diffusion blocking effect for longer oxidation times. While none of these limitations were addressed in the subsequent work of these authors, the model was tested in different super-alloy coating systems with satisfactory predictability of results [158].

Recently, Larson *et al.* [159] made a solid advancement by combining a modified version of the homogenisation model implemented via finite volume, with in-house thermodynamic and kinetic databases to model the oxidation of pure iron, in particular the evolution of the hematite (Fe_2O_3), magnetite (Fe_3O_4), and wustite (FeO). As stated by the authors "diffusion in oxides is inherently much more difficult to model due to the often very narrow existence intervals of the oxides, the large non-linear kinetic variations, and the importance of grain boundary diffusion".

Only few published reports have attempted to numerically model Cr evaporation. Zwetanova [160] used the CALPHAD approach to determine the amount of Cr species reaching the cathode following its volatilisation at 850°C. The authors proposed the use of quantum calculation methods embedded in HyperChem to calculate the radius of the evaporating gas molecules and subsequently the diffusion coefficient according to Maxwell-Stefan diffusivity. The result enabled them to calculate the Cr amount in an LSM/YSZ cathode-electrolyte element after 1000 hours of operation as 79.10^{-6} g.cm^{-2}.

Computational chemistry methods have the potential to be used for useful life prediction of metals and alloys based on phase transformation, but the lack of databases for chromium oxide thermodynamical data means that modelling its oxidation and subsequent oxide formation requires more development in that area.

2.5 Summary

Current research supports that Cr_2O_3 forming ferritic stainless steels are the best match to serve as interconnection materials in SOFC planar designs [21,22,24,27,37,161]. Along with their corrosion resistance, they respond relatively well to the interconnect requirements, as discussed in Section 2.2. Long term, cyclic oxidation studies of chromium, responsible for the formation of a protective chromia scale, are needed, emphasising on the effect of porosity, oxidation temperature, humidity, and flowrate of cathode air, to understand the influence of these parameters in the formation of the oxide scale. The equilibrium partial pressure of oxygen for the formation of a stable Cr_2O_3 passivation layer is lower than that typically occurring in the anodic and cathodic atmospheres, which means that oxidation occurs on both sides of the SOFC cell [162]. However, the $p(O_2)$ at the cathode being much greater than that at the anode (between 10^{-22} and 10^{-17}, depending on the operating

conditions), the consequences of the degradation mechanisms are mainly observed on the cathode side of the SOFC.

The Cr_2O_3 scale which forms on the surface of interconnects as a result of the interaction with oxygen at the cathode grows to micrometres thickness during the stack lifetime (>80,000 hours) and is responsible for degradation mechanisms within the fuel cell stack. This is due to demanding operating conditions (high operating temperature, humidity, presence of oxygen) on the air side of the fuel cell. First, the thickening of the scale induces an increase of the stack electrical resistance; secondly, Cr gaseous species evaporate from the scale and interact with the cathode, altering the electrode composition and creating new phases. This second mechanism is often referred to as "cathode chromium poisoning". In addition, the CTE of this growing oxide scale does not match that of the alloy, which causes the metal to spall after thermal cycling and cooling hence reducing the lifetime of the alloy. This third degradation process is however minor and not being actively investigated as the depletion of Cr from the steel spreads along years of operation [21]. All three degradation mechanisms have the consequence of shortening the service lifetime of SOFCs. Despite these challenges, metallic interconnects are still preferred over their ceramic counterpart, mainly due to the latter's unsuitability for economic mass production, caused by complex manufacturing requirements.

Mathematical modelling has extensively been used towards the development of fuel cell technology. Its flexibility allows for the time-efficient investigation of deep, complex issues as well idealised scenarios hardly achievable in laboratory conditions. The most developed models have focused on the bigger picture, that is cell and stack performance in terms of mechanical stresses, current density or potential, in response to parameter variations. However, modelling publications for certain SOFC component-level degradation mechanisms are rare. This is the case with the degradation of metallic and in particular chromium alloys used as interconnect plates, which after long exposure to an SOFC

environment see their electrical resistance increase, as a result of thick oxide scale formation. One way to understand the long-term effectiveness of coatings on metal interconnects is to increase the understanding of the coatings-substrate interactions. Coupling thermodynamics and phase equilibria modelling of phase changes in alloys with macroscale modelling of diffusion and chemical reactions seems promising, provided that thermodynamic databases containing chromium-based oxide phase descriptions are developed. Future models should make use of concentration dependent diffusion coefficients, which is only possible, if experimentally, these are determined for SOFC operating conditions. Implicit treatment of diffusional phenomena is more appropriate than an explicit approach, as it does not suffer from instability and thus results in more accurate solutions. Validation with experimental data is a prerequisite, as this is required to calibrate the models in order to achieve accuracy of the models for the life expectancy of fuel cells.

Chapter 3 Materials and Experimental Methodology

'But still try, for who knows what is possible' – Michael Faraday

This chapter explains the experiments carried out in this thesis, focusing on the oxidation behaviour of pure chromium and ferritic stainless steels under selected SOFC operating conditions. Detailed experimental procedures are reported on the preparation of chromium pellets by powder metallurgy, their sintering and oxidation test conditions. Similarly, details are given on the steel substrates used, their surface preparation and coupled oxidation-evaporation exposure tests. Finally, characterisation methods used for analysing the specimens' physical, microstructural and chemical properties are described, including PSD, SEM, EDS, XRD and UV-VIS and the theory behind each explained.

3.1. Chemicals, Materials, Pellets and Samples Preparation

3.1.1 Chromium Powder

High purity chromium powder was purchased from Sigma-Aldrich Ltd., UK, (catalogue No.266299) with a manufacturer stated composition of Cr ≥99%. Traces of contaminant were determined by scanning electron microscopy (SEM) and are tabulated in Table 3-1. A raw powder was chosen over commercial pellets to focus on the sinterability of chromium and its effect on the subsequent oxidation behaviour of chromium under SOFC conditions. First, the laboratory pelletisation process of chromium was optimised to determine the suitable amount of pressure. Then its sintering performance with the addition of polymer binders was investigated, focusing on two key sintering parameters, ramping-up and holding time. Finally, the chromium pellets were oxidised under various conditions to investigate the growth of chromium oxide under different atmospheres.

Table 3-1. Contaminant traces identified in the Cr powder; Cr concentration 93.05wt. %.

Element wt.%	Al	O
Cr Powder	5.21	1.74

3.1.2 Fabrication of Chromium Pellets

Fig. 3-1 summarises the fabrication of the chromium pellets. Typically, to prepare a sample pellet, Cr powder was mixed with a binder (paraffin wax or Polyvinyl Alcohol (PVA)) (SIGMA Aldrich, UK), in an amount of 3wt. % of the powder weight. This amount was found to be sufficient to produce solid compacts. The 10% and 20% concentrated PVA solutions were prepared by dissolving respectively 10g and 20g of PVA powder in 100 ml of deionised water and mixing the solution with a magnetic stirrer at 60°C for two hours and

allowing to rest overnight prior to use. The paraffin wax slabs were melted at 60°C and used immediately to prevent solidification. For both binders, the wet mix was then dried under vacuum at 100°C for 15 minutes. The dry mix was ground using a mortar and pestle to create irregular shaped particles, thereby improving the strength of the pellets upon compaction. Finally, the powder was sifted through a metal mesh sieve into the die base of 8 mm diameter and cold pressed twice using a single acting hydraulic press for two minutes, schematised in Figure 3-2. The optimisation of the fabrication of the chromium pellets with the hydraulic press is reported in Chapter 5. Glycerol (SIGMA Aldrich, UK) was used as an internal lubricant to facilitate the ejection of the formed pellets. Binder-free pellets were fabricated for comparison. The pellets were made using a similar process, whereby the powder was ground, sifted and pelletised.

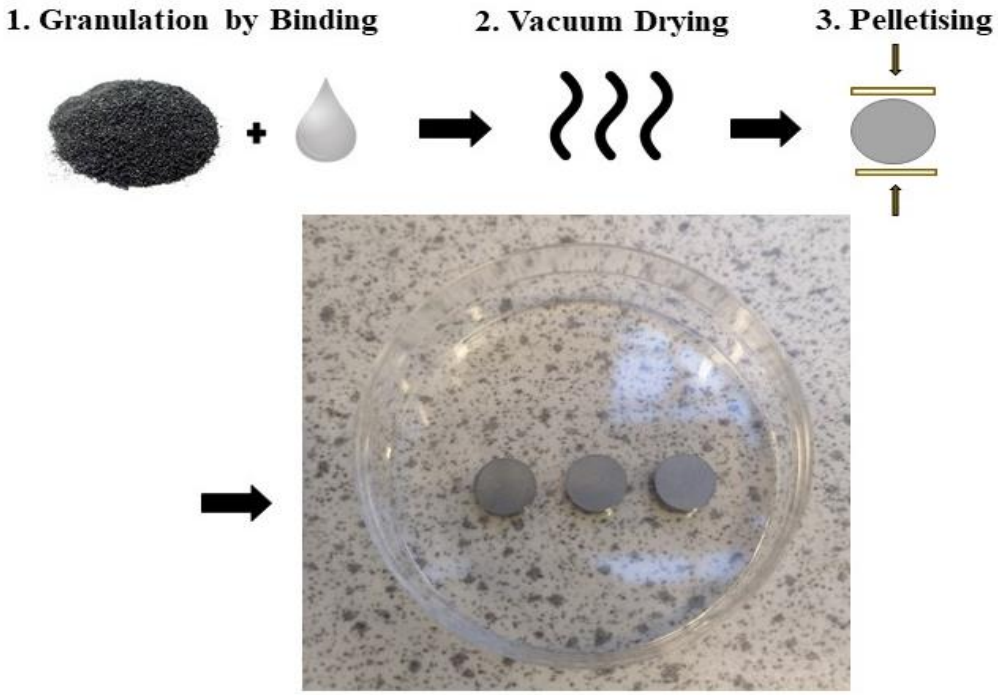

Figure 3-1. Chromium pellets laboratory fabrication process.

3.1.3 Steel Substrates

Crofer 22H and K41 grade stainless steels plates were supplied by VDM Metals and Aperam, respectively. These steels were selected by the SCORED 2:0 project due to their use in current commercial stacks (see Chapter 2). Their as-received nominal compositions are summarised in Table 3-3. Firstly, the effect of surface preparation on oxide layer growth was investigated; grinding and ultrasonic cleaning, two typical sample preparation methods were performed to compare the influence of surface treatment on the growth of the oxide layer. In a second study, the oxidation of these steels under SOFC operating temperature, notably 700°C, was of interest to investigate the growth of the oxide, and comparatively evaluate the oxidation kinetics under different scenarios, including dry oxidation and increased atmospheric humidity content. Thirdly, a comparative study of the evaporation of Cr gases from the steels was undertaken (Section 3.3.2).

Table 3-2. Composition of stainless steels studied as supplied by the manufacturers (Given by SCORED project 2.0 partners).

Element	**Fe**	**Cr**	**C**	**Si**	**Mn**	**P**	**S**	**Ti**	**Nb**	**N**	**Al**	**W**	**Cu**	**La**
wt.%														
K41	Bal.	17.8	0.015	0.6	0.3	-	-	0.65		-	-	-	-	-
Crofer 22H	Bal.	20.0 to 24.0	0 to 0.03	0.1 to 0.6	0.3 to 0.8	0 to 0.05	0 to 0.006	0.02 to 0.20	0.2 to 1.0	0 to 0.03	0 to 0.1	1.0 to 3.0	0 to 0.5	0.04 to 0.20

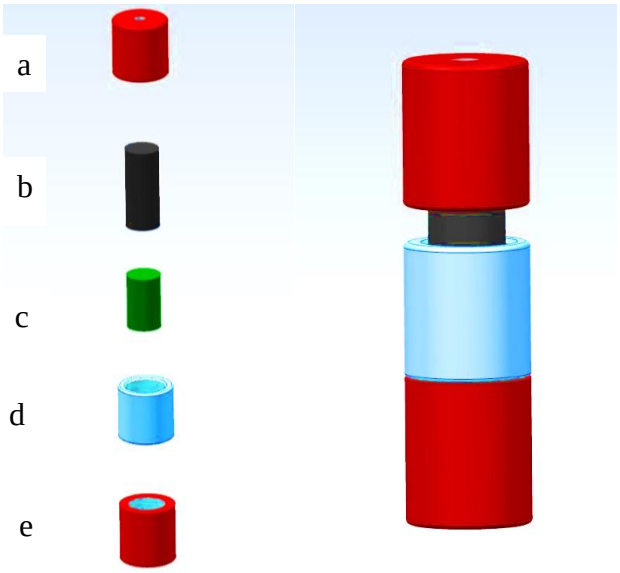

Figure 3-2. Schematic of the die set used for pellets sintering in parts (left) and assembled (right) (a) and (e) top and bottom steel sleeve (b) and (c) pushing rods, (d) opened steel cylinder.

3.1.4 Sintering of Cr Pellets

Sintering of green compacts was carried out in dry hydrogen, in a horizontal quartz reactor illustrated in Figure 3-4. Sintering in hydrogen was chosen to remove oxides, impurities and encourage the strengthening of the compacts. The furnace was flushed with the sintering gas, dry hydrogen, before usage. In the furnace, triplicates of samples were placed on an alumina sample holder plate downstream of the inner glass tube and a flow restrictor made of silicon carbide (SiC) (Norton, UK) was inserted normally to homogenise the feed flow and minimise natural convection. The compacts were gradually heated to 1150^{o}C in hydrogen flowing at 30ml/min and held for a period of time before cooling. Details of the different sintering scenarios (binder and ramp up/down and holding time) examined are summarised in Table 3-3. Post-sintering linear shrinkage, bulk and true density values of the samples were measured to compare the densification of the pellets. The microstructure of the pellets was analysed by SEM to assess the grain growth and overall morphology.

Table 3-3. Tabulation of chromium pellets sintering cases.

Sintering gas	Binder	Ramp up	Holding time	Ramp down
Hydrogen	PVA, 20%wt	10 °C/min	30 min, 1 hour, 2 hours	10 °C/min
Hydrogen	PVA, 10%wt	10 °C/min	30 min, 1 hour, 2 hours	10 °C/min
Hydrogen	Binder free	10 °C/min	30 min, 1 hour, 2 hours	10 °C/min

3.1.5 Preparation of Steel Samples

For all experiments, the received Crofer 22H and K41 plates were cut into 2 cm x 2 cm x 0.2 cm coupons using a Mach water jet cutting machine (Flow, UK), whereby a hair-thin pure waterjet stream is used to cut through the material [163], limiting damages and deformation.

3.1.5.1 Influence of surface finish on oxide growth

Crofer 22H samples were used for this study. The steel coupons were used to investigate the effect of sample preparation on the oxidation behaviour in SOFC conditions. Triplicates of the steel were either rinsed in ultrapure water (18.2 MΩ cm, Milli-Q® ultrapure water system), ultrasonically treated in >99 vol% acetone $(CH_3)_2CO$ for 15 minutes (U300, Ultrawave, UK), or ground with silicon carbide (SiC, Norton UK) paper of grit sizes P800 and P1200 to remove damaged surface regions and existing oxides as summarised in Table 3.4. All samples were further cleaned ultrasonically in acetone alcohol (Fisher Scientific UK), to remove any surface impurities, and then dried under flowing nitrogen.

3.1.5.2 Steels for oxidation and evaporation study

Triplicate coupons of Crofer 22H and K41 steels were used for exposure tests, of which results are reported in Chapter 5. Following the results of the effect of sample preparation, the samples were polished with P800 and P1200 SiC papers to compare the maximum growth attainable, rinsed with IPA and dried with nitrogen. Prior to testing, the samples underwent

SEM/EDS analyses, and their weight was recorded using a micro balance (Cubis micro-Balance, Sartorius, UK).

Table 3-4. Details of the sample preparation methods.

Method	Details
Chemical Cleaning	Samples immerged in acetone and placed in the ultrasonic bath of 40 KHz for 15 minutes.
P800 Grinding	Grinding for 2-3 minutes on the surface and around the edges of the steels using SiC paper of 800 grit.
P1200 Grinding	Grinding for 2-3 minutes on the surface and around the edges of the steels using SiC paper of 1200 grit

3.2 Experiments and Set-up

The fabricated chromium pellets and steel samples were tested using a horizontal split tube furnace fitted with an automatic three term PID Cal 9500 programmer (Vecstar Limited, UK). Each test was repeated two or three times and the error bars represent standard deviation of measurements. The test system is shown in Figure 3-3 to Figure 3-5.

3.2.1 Coupled Oxidation and Volatilisation

The oxidation and volatilisation experiments of chromium pellets and ferritic steels were carried out using the denuder tube described in 3.2.2. The set-up (Figure 3-3 and Figure 3-4) consisted of an outer tubular quartz glass reactor, with an internal diameter of 50 mm into which an inner glass tube of 42 mm internal diameter was inserted to support the samples and the denuder tube. The glass setup, placed in the horizontal furnace was completed with a removable quartz glass cap held with clamps on the upstream of the tube. Each glass element

was fitted with a hole of 7 mm diameter into which the 60 cm long denuder tube was inserted.

The coating reagent inside the tube, Na_2CO_3 was used to collect the volatile chromium $CrO_2(OH)_2$, via the reaction shown in the equation:

$$Cr_2(OH)_{2(g)} + Na_2CO_{3(s)} \rightarrow Na_2CrO_{4(s)} + H_2O_{(g)}$$ Equation 3-1

Samples were oxidised for up to 1000 hours at 700°C in flowing compressed air at 1000ml/min with water vapour content of 0, 3 or 10 vol%. The water vapour was achieved by either bubbling the gas through deionised water or using a Controlled Evaporator Mixer (CEM) (Bronkhorst LTD, UK). For each experiment, samples were removed periodically to measure their mass change. The denuder tube was rinsed regularly with 15 ml of distilled water to dissolve the formed Na_2CrO_4. The collected solutions were analysed with a ultraviolet visible spectrophotometer, described in section 3.3.6 to quantify the amount of evaporated Cr species over a period of time. During coupled oxidation-evaporation tests, the mass change of samples was periodically measured whilst chromium gas production was periodically evaluated in parallel.

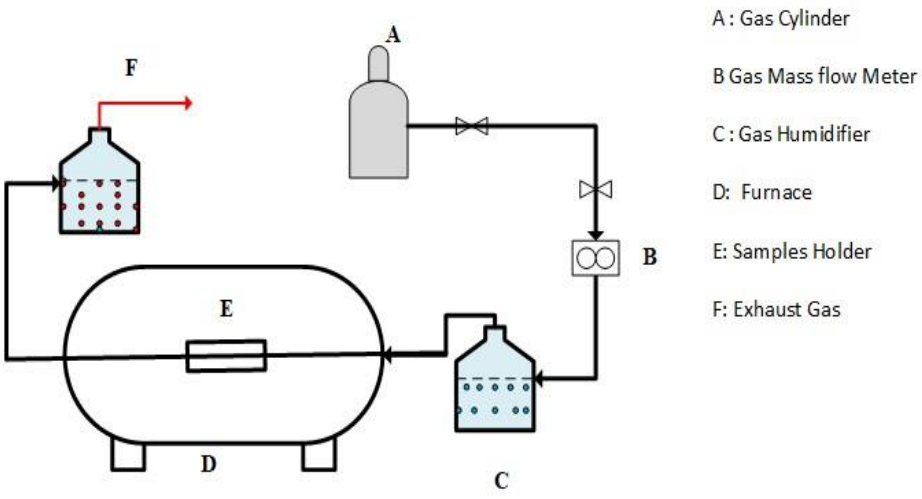

Figure 3-3. Exposure testing system. (drawn, not to scale).

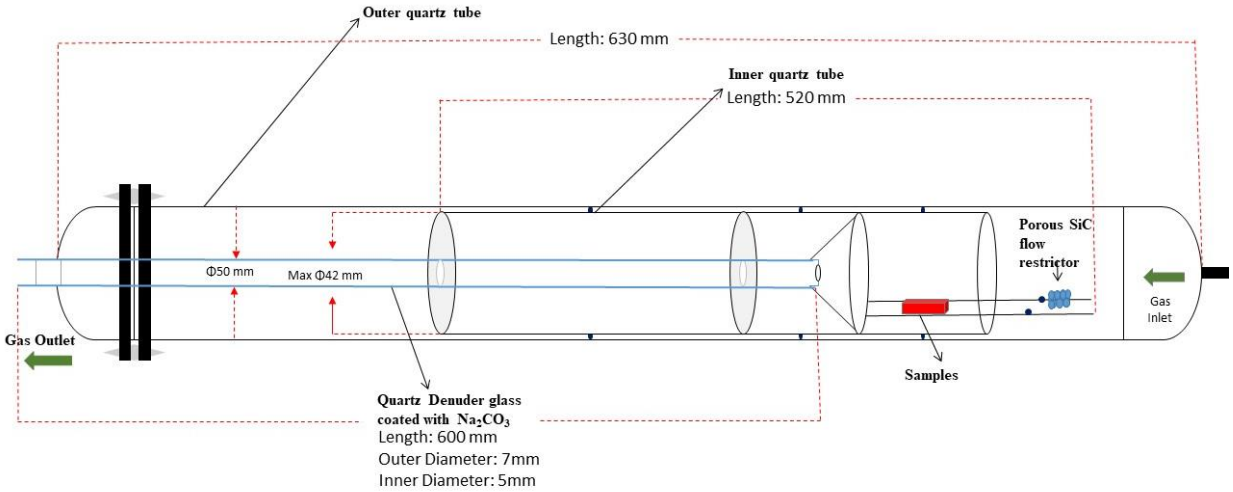

Figure 3-4. Schematic diagram (not to scale) of the built rig used for sintering and exposure tests. The set-up consisted of three tubes made of quartz: an outer glass, and inner glass holding the samples and a denuder glass coated with Na_2CO_3 (drawn, not to scale).

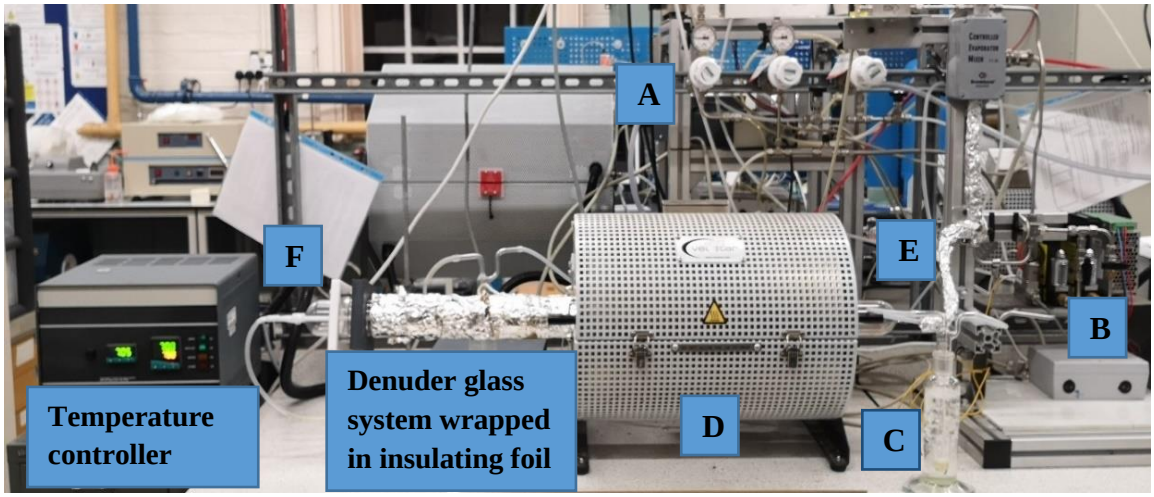

Figure 3-5. Annotated sintering and exposure tests system from Fig. 3-4.

3.2.2 Preparation of Coating Solution and Denuder Tube

For the coupled oxidation-evaporation exposure tests described in section 3.2.1, a quartz glass cylindrical tube with open ends, known as a denuder tube, was used to collect the evaporating chromium gas $CrO_2(OH)_2$. This technique, developed at Chalmers University of Technology by Froitzheim *et al.* [2] has been extensively tested and used to collect volatile

chromium (IV) [33,64,66,105,111]. The method relies on the formation of a solid coating, Na_2CO_3, on the inside walls of a glass tube which collects evaporating Cr during exposure to oxidation conditions. To prepare the coating, a solution was made by dissolving the required amount of solid sodium hydroxide (NaOH) with methanol (CH_3OH) and magnetically stirring for at least 8 hours, ensuring the total dissolution of NaOH. This solution was then piped into the inner walls of the denuder glass tube and blow-dried to solidify (the tube was rinse inside out with ethanol and DI water and dried in a laboratory oven). Finally, a stream of carbon dioxide (CO_2) was passed through the coated tube for one minute (or until the disappearance of the reaction produced steam) to produce the collecting solid reagent Na_2CO_3, via the reaction:

$$NaOH_{(l)} + CO_{2(g)} \rightarrow Na_2CO_{3(s)} + \uparrow H_2O_{(g)} \qquad \text{Equation 3-2}$$

As previously mentioned, the tube was replaced regularly, and the evaporated chromium trapped in the tube was collected by rinsing the tube DI water (15 ml).

3.3 Material Characterisation and Analysis

The physical, microstructural and chemical properties of the chromium pellets and ferritic stainless steels Crofer 22H and K41 were characterised using the various methods. SEM-EDS were used to analyse the microstructural changes in sintered and oxidised chromium pellets as well as oxidised steels. Laser light diffraction was used to measure the particle size distribution of the chromium powder, whilst gas displacement pycnometry was used to determine the density of the chromium pellets pre - and post - sintering. Tensiometry was used to measure contact angle changes post-exposure of as-received and pre-treated steels samples. Finally, ultraviolet-visible spectrophotometry was used to determine the amount of volatile chromium from the exposed steels.

3.3.1 Particle Size Distribution

The particle size distribution (PSD) of the as-received chromium powder was confirmed using laser light diffraction technique (Chapter 4). PSD is a widely used particle size analysis method, whereby the intensity of laser light passed through a particle is measured, which is directly related to the size of the particle. The quantification, internal to the software, is based on the Mie scattering theory [164], which proposes that the light scattering is proportional to the second power of the wavelength and is thus better suited for particle sizes greater than the light wavelength [164,165].

$$E_{Mie} = 0.434Bc\pi\left(\frac{2\pi}{\lambda}\right)^{v-2}E(\lambda) \qquad \text{Equation 3-3}$$

where E is the Mie scattering, c is the concentration factor that varies with turbidity, v is known as the Junge's exponent and B= 0.68 in the visible spectrum.

The Cr powder particles were sized with a Malvern Mastersizer 2000 (Malvern Instruments, UK) built for a particle size detection in the range 0.02 to 2000 microns. Cr powder was added to a dispersion unit in sufficient amount to achieve the required obscuration. In order to keep the particles suspended and homogenised, the suspension was continually recirculated inside the external dispersion unit. A recirculation speed of 2000 rotation per minute (rpm) was found to be sufficient. To calculate the particle size, the software called for an input of the refractive index of the material (3.13 in the case of chromium) and dispersant (1.33 for the deionised water used). All sizing measurements were executed three times, and the average result reported.

3.3.2 Chromium Pellet Density and Porosity

Density and porosity are reliable indications of sintering quality. The density and porosity of pre-sintered and post-sintered Cr pellets were determined and reported in chapter 4 by gas displacement pycnometry. Pressurised helium is fed into one of the two vessels of the gas

pycnometer (Acupyc II 1340, Micrometrics Instrument Corporation) (Figure 3-6.) containing the weighed pellet. The envelope density (measured using a digital calliper), necessary to calculate the sample porosity was input into the software. By applying the ideal gas law (PV=nRT) and detecting the pressure difference between the empty chamber and the void volume of the chamber containing the sample , the instrument determined the sample volume V_x (sum of the volumes of the solid material and closed pores within the pieces) [166], and calculated the true density and percent porosity (Eq.3-4 and 3-5). Each measurement was performed three times, and the averaged data reported for each sample.

$$V_x = \frac{(P_{sys}V_s + P_{sys}V_r - P_sV_r)}{P_{sys} - P_s} \qquad \text{Equation 3-4}$$

$$\%\, Porosity = \frac{(V_x)}{V_B} x100 \qquad \text{Equation 3-5}$$

where P_{sys} is the pressure of the system, V_r the volume of the empty chamber, V_s the sealed sample chamber, P_s the pressure within the sealed sample chamber and V_B is the bulk volume of the sample measure with a calliper.

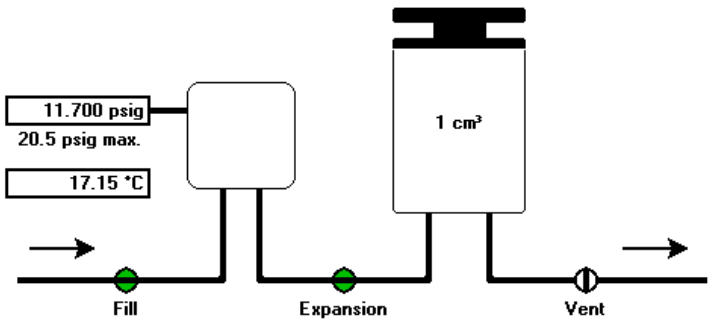

Figure 3-6. Schematic diagram of the gas pycnometer in use (taken from equipment in operati on).

3.3.3 Tensiometry

The contact angle θ, defined as the equilibrium of a droplet under the influence of three interfacial energies (Eq. 3-6) was measured pre-and-post-exposure of Crofer 22H to compare

the degree to which each of the sample preparation methods had an effect on the growth of the oxide layer. Results were reported in Chapter 5.

$$\gamma_{SV} - \gamma_{SL} = \gamma_{LV} cos\theta + \pi \quad \text{Equation 3-6}$$

where γ_{SV} and γ_{SL} are the interfacial surface tensions of the solid/gas interface, and solid/liquid interface, respectively, γ_{LV} the surface tension of the liquid, π the spreading pressure, and θ the measured equilibrium contact angle.

Measurements were carried out at room temperature using a volume changing method. A Sigma700 optimal tensiometer (Dyne technology, UK) was used, consisting of a screw-thread micrometre onto which a needle-syringe system was fitted to deliver a water droplet on the sample surface. As the droplet grew onto the surface (Figure 3-7.), the forces exerted by the liquid were used by the software to measure the advancing and receding contact angles, as the volume of the droplet was gradually increased and then decreased. The built-in software measured these angles via a high magnification camera.

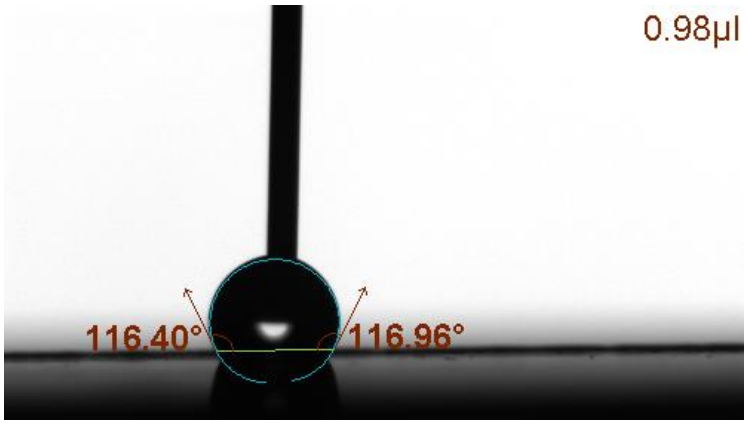

Figure 3-7. Schematic of the live dynamic contact angle measurement using volume changing method, showing the angles measured on each side of the droplets and the volume of the droplet (0.98 µl).

3.3.5 Energy Dispersive Spectroscopy (EDS)

Energy Dispersive X-ray Spectroscopy (EDS) integrated with SEM was used to analyse the compositional distribution of samples before and after sintering and exposure tests to various conditions in chapter 4 and 5. The spectra of elemental distribution across the samples was acquired using a Quantax 70 EDS detector (Bruker, UK) and the data acquisition was performed for 180 seconds, using an accelerating voltage of 15kV.

3.3.6 Ultraviolet–visible Spectrophotometry (UV/VIS)

Spectrophotometry relies on the principle that every chemical substance absorbs and reflects light over a specific wavelength range and thus stands as a method of measuring the intensity of that light and subsequently the concentration of a chemical compound. Due to the maximum light absorbance of chromate in solution having been identified as 373 nm wavelength [167], UV/Vis spectrophotometry was used, which produces light over 185 to 400 nm wavelength in the UV range and 400 to 700nm in the visible range.

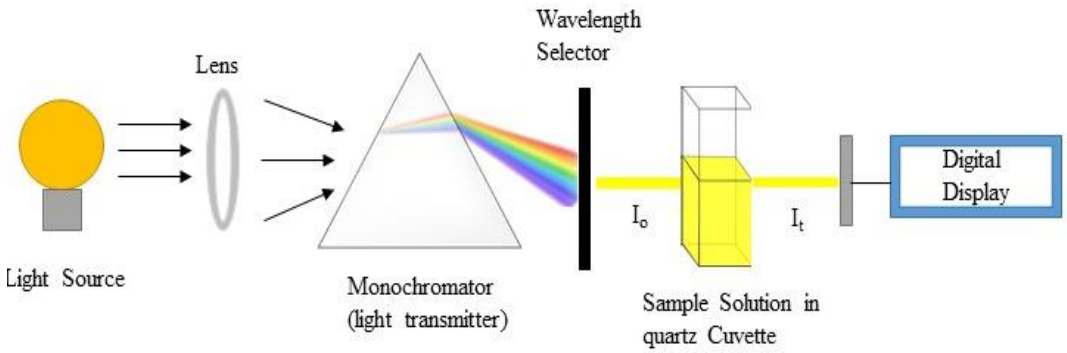

Figure 3-8. Schematic diagram of a spectrophotometer working principle.

During the coupled oxidation-evaporation tests of chromium pellets in chapter 4 and ferritic stainless steels in chapter 5, volatile $CrO_2(OH)_2$ was trapped by a denuder tube (see section 3.2.1) and rinsed regularly in ultrapure water. A double beam UV/visible spectrophotometer

(Aquarius 7500 CECIL-CE, Cecil Instruments Ltd, UK) was used to quantify the total amount of Cr evaporated for each periodical denuder tube replacement. The set up consisted of a chamber into which two small quartz cuvettes containing ultrapure water and the sampled Cr solution were placed, respectively. As the light passed through the solution, the intensity of light absorbed by the sample was measured, which was then used to calculate the concentration of chromium species collected (Figure 3-8). For each time sampled solution, the analyses were repeated thrice, and the average data was reported.

Chapter 4 Optimisation of Low Porosity Chromium Pellets

« Même si j'ai peur le soir, moi j'ai besoin de croire que mes efforts seront récompensés »

This chapter focuses on producing low-porosity chromium pellets at a low sintering temperature, destined for exposure testing under SOFC cathode operating conditions in Chapter 5. Binder-free and binder containing chromium pellets were fabricated by optimising the cold isostatic pressing of pure chromium powder. The pellets were then sintered in pure hydrogen gas at 1150°C. The influence of varying sintering times was analysed using the porosity, density and micrographs of the Cr pellets before and after sintering. This also conducted to evaluate the potential effect of low temperature sintering parameters on the oxidation of chromium.

4.1. Introduction

Most current alloys used for interconnect applications are of chromium-forming alloys [21,168] which are alloyed with 17 to 25 wt.% of chromium [66,169]. The use of ferritic stainless steels (FSS) as interconnect materials has induced a growing interest in the oxidation behaviour of elemental chromium in alloys, which offers the potential for oxidation and corrosion resistance by forming a protective chromium oxide layer (Cr_2O_3). In past decades, however, research mainly studied the oxidation behaviour of chromium in the range above 900^{o}C, in either dry air or gas mixtures such as Ar-O_2 [147,170]. Studies on Cr-based interconnects have highlighted the importance of additional factors affecting the kinetic behaviour of chromium in these alloys such as manufacturing methods (powder metallurgy or traditional machining), surface treatment (nitriding, cleaning, heat treatments, etc.), presence of moisture, and operating condition-induced stress [47,75,147,171]. This study focuses on the sinterability of chromium powder, which is used in steel interconnects fabricated using powder metallurgy (PM), whereby raw powders composing the metal or alloy are mixed and compacted in shaped dies to form pellets known as green compacts. The sintering process involves heating the green compacts to a temperature below their melting point and holding this temperature for a determined period. The temperature selected should be at least 60% of the melting temperature of the element with the lowest melting point. Sintering is normally carried out in a reducing atmosphere (H_2 or Ar-H_2, N_2-H_2) to minimise oxide formation and to reduce existing oxides, lubricants and binders used in pelletising. It was suggested that in PM, sintering, which aims to increase the material's compact strength [19] is the most important step for the oxidation resistance of the steels. This is reportedly due to the fact that highly porous parts resulted in faster oxidation rates, caused by accelerated kinetics [73,172]. High density and low porosity sintered parts are, thus, the desired properties. Little research has been conducted on the sintering of ferritic stainless-steel elements. Considering that

chromium is essential to the growth of the oxide protective layer, understanding its sinterability is important. An early study was published on producing high porosity sintered chromium at 1200°C [76] using fast heating rates, resulting in highly porous samples (>30% porosity). Therefore, a method for producing low porosity chromium parts will be proposed with significant emphasis on optimising the pressability and sintering of pure chromium pellets. This was achieved by comparing applied pressure force, heating profiles, holding times and binder addition to evaluate their impact on the density, porosity and microstructure of the pellets.

4.2. Optimising Chromium Pellets Preparation

4.2.1 Chromium Powder Selection and Characterisation

The observed characteristics of the base chromium powder used are reported in this section. The selection of powder characteristics (size, shape composition) is an important feature in pellet making as it influences the result of the pelleting process. Metal powders can have a spherical or irregular shape, but irregular particles are often preferred as their plastic deformation is believed to lead to greater strength and structural integrity of the green compact [68]. As a result, irregularly shaped powder particles were chosen (Figure 4-1). Initially, 100 mesh size chromium powder (149 μm) was selected but did not show good pressability into compacts, even at a higher compaction force (up to 15 metric tons) and with binder addition. This was believed to be because of the coarseness of the powder and thus, a smaller powder size of 325 mesh (44 μm) was selected.

The chromium powder specified by the supplier (Sigma Aldrich Ltd) reportedly contained ≥99% of pure Cr with trace metals; this was analysed by SEM-EDX (see Chapter 3 for technique description). The EDX scan revealed the presence of contaminants including a

small amount of elemental manganese (Mn) and a greater amount of aluminium (Al), as well the presence of surface oxides as affirmed by the oxygen content (Table 4-1 and Figure 4-1). The powder morphology was analysed by SEM and the micrographs are presented in Figure 4-1. The irregularly shaped grains were characterised by a coarse surface marked with nodules. Table 4-2 reports the size distribution of the supplied chromium powder measured by dynamic light scattering (DLS), as well as the powder density determined by pycnometry (see Chapter 3 for description of DLS and pycnometry techniques). The median diameter (D50) of this commercial powder was 39.6 µm (Figure 4-2) (that is, 50% of the amount of particles have diameters smaller and larger than this value), with a relatively high specific surface area of 0.221 m^2g^{-1}. D10 and D90 refer to the amount of particles which have diameters below 10.81 and 80.52 µm, respectively.

Table 4-1 Chemical composition, as given by the supplier and based on EDX.

As-Received Cr powder	**Chemical composition [wt.%]**			
	Cr	Al	O	Mn
	91.04	5.90	2.51	0.55

Table 4-2 Particle size Distribution of the powder-based on DLS.

As-Received Cr powder	**Particle size distribution (µm)**		
	D10	**D50**	**D90**
	13.81	39.63	80.52
	Powder density ($g.cm^3$)		
	8.417		

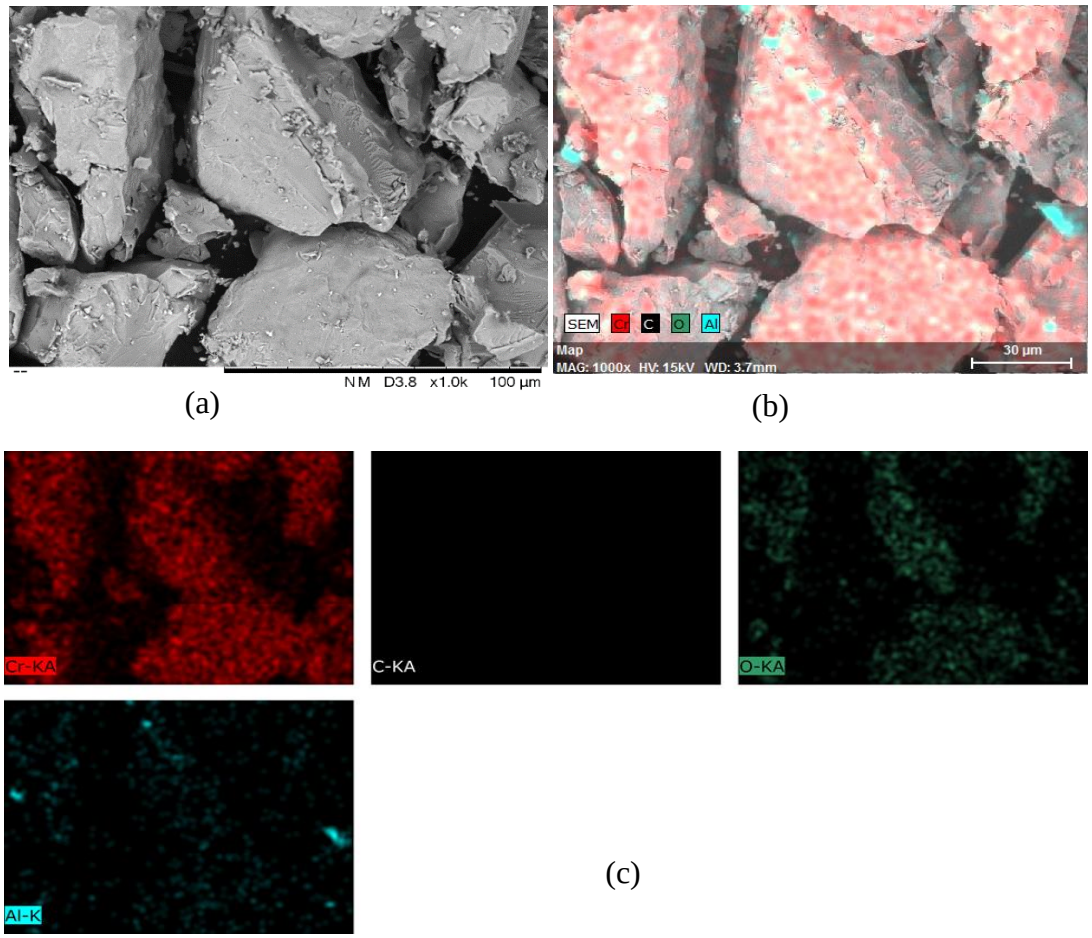

Figure 4-1: (a) SEM image of Cr powder (c, b) EDS element mapping analysis and (c) corresponding EDS mapping analysis. (c) shows elemental mapping of Cr (red), aluminium (light blue), carbon (black) and oxygen (green). Scale bars are shown in white at 100 µm and 30 µm.

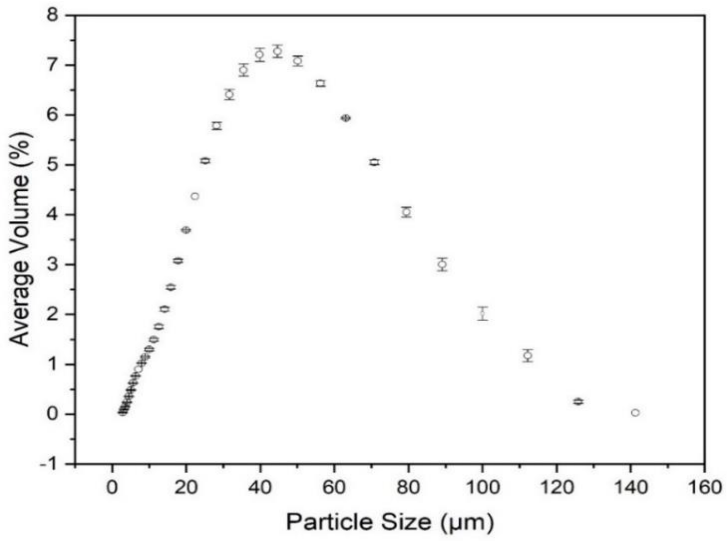

Figure 4-2 Size distribution of Cr powder determined using DLS.

4.2.2 Comparison of Binders on Green Compacts Density and Porosity

Binders are generally added to enhance the compressibility of powders and increase the strength of green compacts (see Chapter 2). However, by doing so they also reduce cohesive forces among the powder particles, thereby inducing more porosity in the compacts [73]. Two organic polymer binders, namely paraffin wax and polyvinyl alcohol (PVA), were added to the powder samples in amounts of 4 wt. % of the Cr powder sample weight. Melted paraffin wax along with 10 wt. % and 20 wt. % solutions of PVA were used. The preparation of these binders is detailed in Chapter 3.

The powder samples were compacted into round green compacts of 0.8 cm diameter and 0.13 cm thickness. The resultant densities and porosities of the green pellets were measured and are tabulated in Table 4-3.

Table 4-3. Effect of binder on density and porosity of green compacts.

Type	**Green density ρ_g (g/cm^3)**	**% of Powder density (%ρ_t)**	**Porosity (%)**
No binder	7.07	83.99%	14.37
Paraffin wax	7.13	84.70%	28.80
PVA 10 wt.%	7.11	84.46%	17.14
PVA 20 wt.%	6.94	82.44%	14.33

*All densities stated in the table were of average value for three compacts with an error bar less than ±0.01

The green densities and porosities of the Cr pellets post compaction were added for comparison. All green pellets showed increased density post compaction (above 80%) and appeared to be brittle upon contact. Overall, the pellets demonstrated similar densities, and varying porosities. It can be seen that the compacts with added paraffin wax achieved the highest green density of 7.13 g/cm^3, but equally the highest porosity of 28.80%. The second

highest porosity was obtained with 10% PVA, which was lowered by approximately 3% by doubling the concentration to 20% PVA. Pellets prepared with 20 wt. % PVA and binder-free pellets showed the lowest porosities, with binder-free pellets achieving a higher green density of 7.07 $g.cm^3$ against 6.94 g/cm^3 for 20 wt. % PVA pellets. Due to the high porosity showcased by pellets containing paraffin wax, only the PVA (10 and 20 wt. %) binder was selected and investigated alongside pellets without a binder.

4.2.3 Effect of Cold-Pressing on the Density of PVA and Binder-free Green Compacts

To investigate the pressability of chromium powders, compacts with no binder and with added PVA in amounts of 3 wt. % were pressed using a uniaxial hydraulic press, as described in Chapter 3. The true density of the pellets post compaction was measured to examine the pressability of chromium and determine the suitable compaction pressure to be used in pelletising Cr powder throughout this work. The developed compressibility curves for binder-free pellets and pellets containing 10 wt. % PVA are shown in Figure 4-3 and Figure 4-4.

The green density of the compacts with no binder increased with increasing applied force (Figure 4-3); at the same time, the rate of densification reportedly slowed. At four tons of compaction pressure, the green compacts reached a density of 7.109 g/cm^3; the increment to five tons resulted in approximately 0.04% higher green density. Because high compaction may cause tooling wear, four tons were selected and used throughout this work for pelletising. Inversely, the green density for pellets containing a binding agent decreased with higher compaction force, as shown in Figure 4-4. This may be due to fine particles of the binder elastically sitting in between the powder grains moving the latter apart when the pressing force is released, thus leading to a reduction in density. The density continuously decreased because of the greater compaction force, the farther the powder grains were relaxed

upon release. However, similar to the binder-free pressability test, for every increment of compaction force, the rate of densification slowed.

Therefore, from a pelletising perspective, chromium pellets with no added binder were denser than PVA binder containing pellets, which showed a decrease of density throughout.

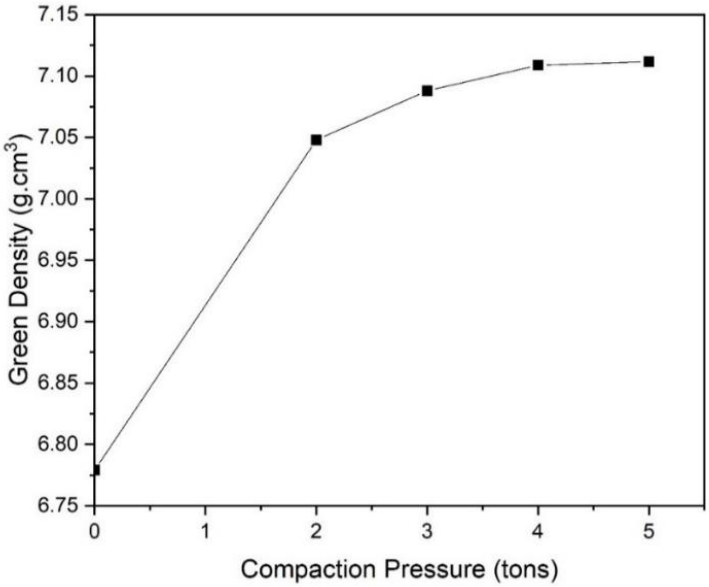

Figure 4-3. Compaction force curve for binder free Cr pellets.

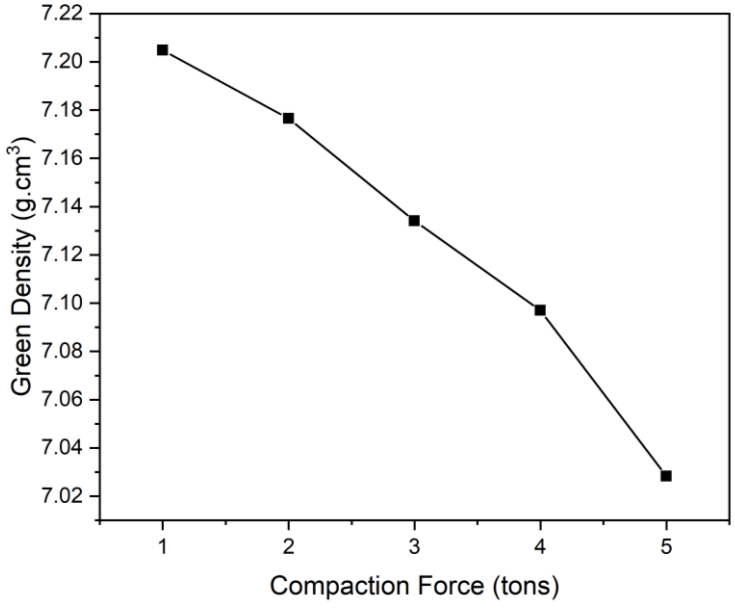

Figure 4-4. Compaction pressure curve for Cr pellets containing 10 wt.% PVA.

4.3 Sintering Behaviour of Chromium

Sintering consists of thermally processing powders or compacts whereby particles bond through atomic motion, which results in solid, more compact and stronger material (see Chapter 2). Sintering results are influenced by key parameters including particle size, ramping-up rate, sintering temperature, and holding time. Two opposed mechanisms compete in densification [68]. Densifying particles are led by grain boundary diffusion, lattice diffusion and plastic flow and achieve neck growth, densification and shrinkage of the particles. On the other hand, coarsening, shrinkage and high porosity opposed the densification effect (Fig. 4-5) [68].

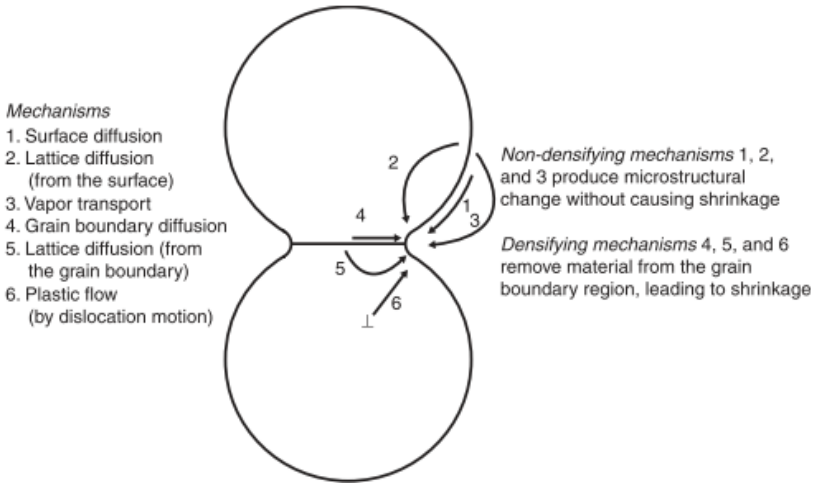

Figure 4-5. Densifying and non-densifying mechanisms observable between two sintered particles [68].

The sintering behaviour of binder-free and binder (10% and 20% PVA) containing chromium pellets was studied in relation to these key factors and their effect measured through true density, shrinkage, and porosity changes. As previously mentioned, true density corresponds to the density of the material excluding the pores. The densification factor is a useful measure

of the sintering process as it expresses the relative change in porosity in relation to the starting porosity [173]:

$$\psi = \frac{(\varepsilon_s - \varepsilon_g)}{\varepsilon_g} \qquad \text{Equation 4-1}$$

where ε_s is the sintered true porosity and ε_g is the green true porosity of chromium powder, here calculated by gas pycnometry.

Previous work by Fedorchenko and Solonin reported successful sintering of Cr pellets at 1200ºC [76], that is, 60% of the chromium melting point. In this work, a temperature of 1150ºC was used, which corresponds to the maximum temperature allowed by the furnace available.

Figure 4-6. shows the temperature profiles used for sintering Cr pellets. At the start, a stream of hydrogen gas was passed to create a reducing atmosphere. Hydrogen gas with a dew point of -20ºC was flowing at 30 ml/min to prevent oxidation of the Cr pellets. Samples were then heated up to the target temperature of 1150ºC using different ramping up rates: 50ºC/min, 10ºC/min, and 1°C/min. The samples were held for different periods: 30 minutes, one hour, and two hours before cooling down.

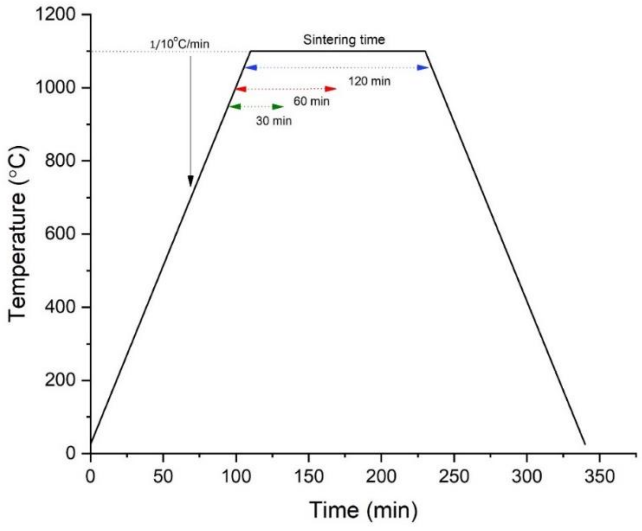

Figure 4-6. Temperature profiles used for sintering Cr pellets (not to scale).

4.3.1 Sintered Cr Pellets containing 20 wt. % PVA at 10°C/min

The sintering results of pellets containing 20 wt. % PVA, sintered at a ramping up of 10°C/min, are summarised in Table 4-4 Figure 4-7 plots the change in sintered density for Cr pellets as a function of sintering time. The density results are tabulated in Table 4-4, alongside the densification factor and porosity change. The results show that, overall, sintering at 10°C/min led to a lower density across all holding periods. However, as sintering time increased, the densification ratio also increased (Table 4-4). The highest densification was obtained after two hours of sintering whereby the porosity of the samples decreased for the first time and an apparent shrinkage of the specimen was noticed. Shorter holding periods produced appreciably higher porosity, particularly for pellets sintered for 30 minutes, whereby the porosity increased by 27% (Table 4-4). Overall, a longer holding time of two hours slightly reduced the loss of density and eventually led to less porosity in the pellets.

Table 4-4. Tabulation of green and sintered true density and relative densification for pellets sintered at different sintering times in hydrogen at 1150°C with 20 wt.% PVA and heating at 10°C/min.

Sintering time	Green true density ρ_g (g/cm^3)	Green porosity (%)	Sintered true density ρ_g (g/cm^3)	Sintered Porosity (%)	Densification factor
30 minutes	7.169	16.79	6.857	21.37	-0.272
1 hour	7.0925	13.92	6.946	14.38	-0.033
2 hours	7.100	14.69	6.995	14.62	0.004

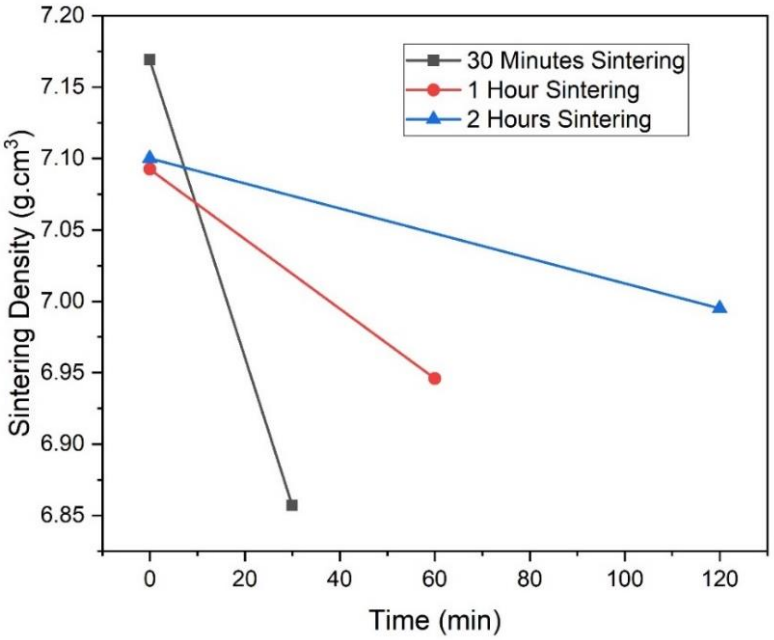

Figure 4-7. Sintered density for 20 wt.% PVA Cr pellets sintered at 10^{o}C/min.

In Figure 4-8., scanning electron micrographs of the sintered samples show observable particle bonding, which occurred during sintering 20wt.% PVA Cr pellets. Necks appear to have grown at the particle contact points (circled in red). The neck ratio X/D, a dimensionless parameter of the neck diameter (X) over the particle size (D), is fundamental in monitoring the sintering process. The results show that neck growth was very slow at 30 minutes of sintering and neck regions started to appear more noticeably after one hour of sintering, proving that the particle size enlarged as sintering progressed [173]. The necks appear to have a concave shape, which suggests that particle enlargement is the result of mass transport at the pore surfaces, where atoms are transported towards the neck. As grains grow but reduce in number, denser but also greater shrunken samples are obtained after two hours of sintering.

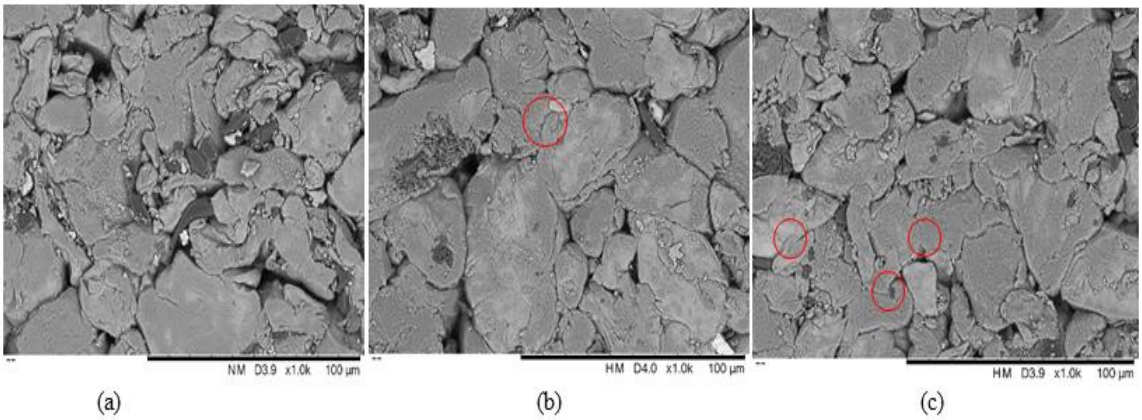

Figure 4-8. SEM of 20% PVA Cr pellet after sintering in hydrogen at 10^{o}C/min ramp-up rate for (a) 30 minutes, (b) 1 hour, (c) 2 hours.

The quartz glass utilised in these experiments was used at its maximum normal working temperature of 1050°C. The pellets were sintered using a 10°C/min ramp rate, as suggested by [76], who stated that rapid heating would be more effective. The results showed that densification of the pellets occurred at a holding time of two hours but did not occur at 30 minutes or one hour holding times. Also, the porosity increased during these sintering times, with only a small decrease after two hours of sintering. Furthermore, during the repeated cycle tests, the outer glass suffered from the appearance of multiple cracks, a sign of its devitrification. Consequently, the heating profile was changed to 1°C/min.

4.3.2 Sintered Cr Pellets of 10 wt.% PVA at 1°C/min

The sintering results of compacts containing 10% PVA and sintered at a ramp-up rate of 1°C/min are shown in Figure 4-9 and summarised in Table 4-5 The results show that the true density of chromium pellets containing 10 wt. % PVA was greater than those containing 20 wt.% PVA sintered for the same period of time. Although the pellets containing 10 wt.% PVA showed a much higher initial true density, they achieved much greater densification as portrayed by the densification factors determined (Table 4-5). These results showed that PVA

with a concentration of 10 wt. % was a better binder compared to 20 wt.%. The highest densification and lower porosity for these samples were obtained after two hours of sintering, with a porosity of 11% and a sintering density of 6.868 $g.cm^{-3}$, that is, 81% of the initial chromium powder density.

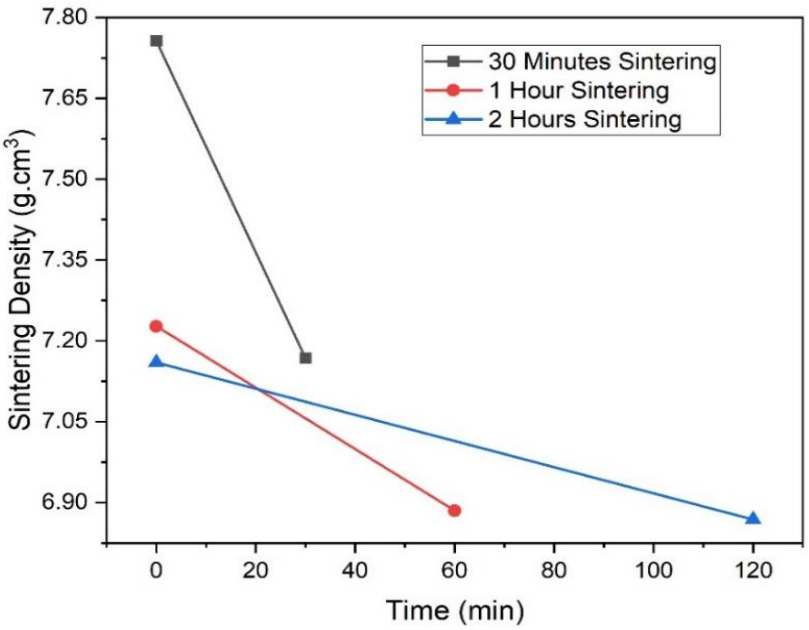

Figure 4-9. Sintered density for 10 wt.% PVA Cr pellets sintered in H_2 at 1°C/min.

Table 4-5. Tabulation of true densities and densification for pellets sintered at different sintering times in H_2 at 1150°C with 10% PVA and heated at 1°C/min.

Sintering time	Green true density ρ_g (g/cm^3)	Green porosity (%)	Sintered true density ρ_g (g/cm^3)	Sintered Porosity (%)	Densification factor
30 minutes	7.756	21.0	7.167	14.19	0.324
1 hour	7.938	24.5	6.052	12.46	0.491
2 hours	7.160	22.8	6.868	11.41	0.499

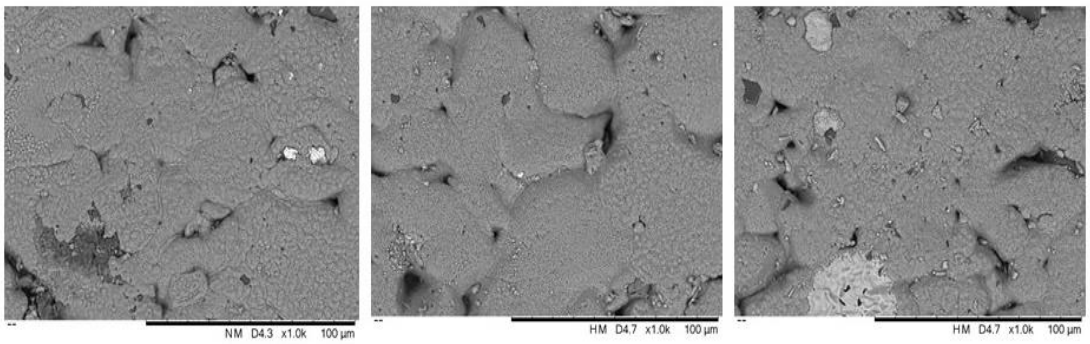

Figure 4-10. SEM of 10% PVA Cr pellet after sintering in hydrogen at 1°C/min ramp-up rate for (a) 30 minutes, (b) 1 hour, (c) 2 hours.

Scanned electron micrographs of the sintered samples are shown in Figure 4-10. The images mirror the density and porosity results determined by SEM. Across all holding times, the particles appear to have congregated into large clusters, which is a result of neck growth at contact points. The necks present an accentuated concave shape and appear to be smoother than those of 20 wt.% PVA pellets. Physical measurements of the pellets pre- and post-sintering revealed that the particles had swollen. After two hours, the particles are still somewhat visible, but the clusters have enlarged. Conclusively, sintering with 10 wt.% PVA led to the densification of the pellets with a porosity ranging between 11 and 15%.

4.3.3 Sintered Binder-free Cr Pellets at 1°C/min

The effect of holding time and ramp-up rate on the density and microstructural characteristics of binder-free Cr pellets was investigated for the three holding periods, at 1150°C and 1°C/min ramp-up. Across all holding times, in comparison to binder-containing pellets, binder-free samples exhibited a much higher density (Table 4-6).

This arises from the fact that in general, the presence of binders in metal powders impedes the progression of sintering [76]. The evolution of porosity in the pellets demonstrated that the achieved porosity in binder-containing pellets was dependent on the holding time; after a

holding time of two hours, binder-free pellets exhibited a lower porosity, that is, 30% less compared to 30-minute holding periods. The evolution of sintering density as a function of holding time is shown in

Figure 4-11 and densification factors summarised in Table 4-6. Similar pellets containing 20 wt.% PVA binder and sintered binder-free pellets exhibited a lower density than green pellets. The densification obtained during one hour of sintering was lower to that obtained at a holding time of 30 minutes and two hours. Here, the influence of sintering time is not analogous to binder-containing pellets. As shown in Figure 4-12, pellets sintered for one hour appear less dense with a densification factor of 0.27, compared to 0.35 and 0.38 for 30 minutes and two hours sintering, respectively.

Table 4-6. Tabulation of green and sintered true density and relative densification for free pellets sintered at different sintering times in hydrogen at 1150°C with no binder and heated at 1°C/min.

Green true density ρ_g (g/cm^3)	**Green porosity (%)**	**Sintered true density ρ_g (g/cm^3)**	**Sintered Porosity (%)**	**Green true density ρ_g (g/cm^3)**	**Relative densification**
30 minutes	7.637	22.94	7.148	14.78	0.35
1 hour	7.113	16.28	6.903	11.80	0.27
2 hours	7.158	16.57	6.801	10.24	0.38

Contrary to binder-containing pellets, SEM micrographs reveal neck growth and particle enlargement from 30 minutes sintering time with less apparent grains and smoother neck regions, as the particles converge into a polycrystalline solid.

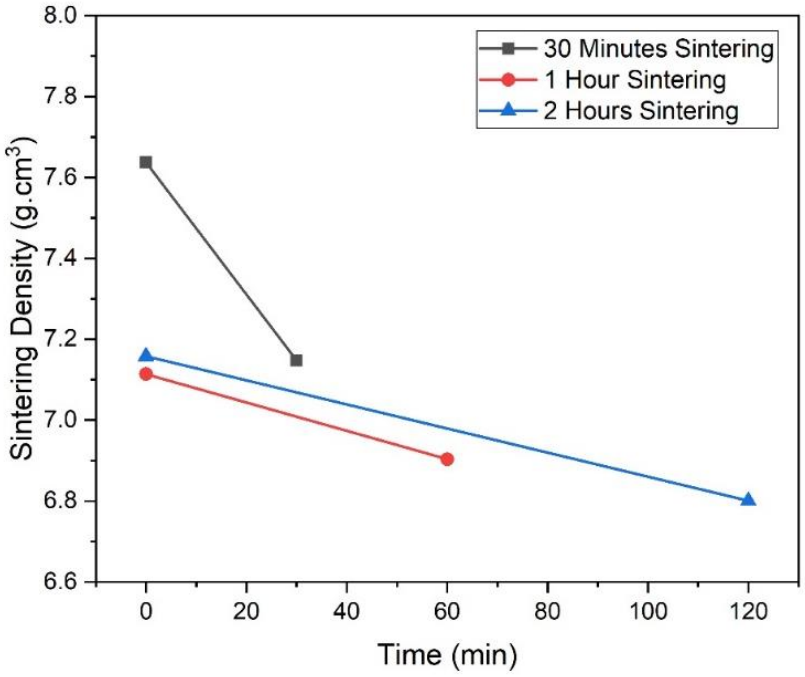

Figure 4-11. Sintered density for binder-free pellets sintered at 1°C/min.

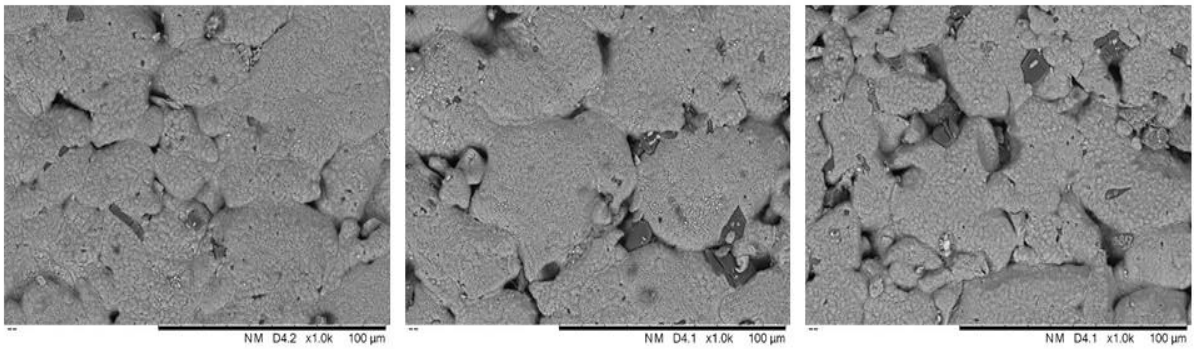

Figure 4-12. SEM Cr binder-free pellets after of sintering in hydrogen at 1ºC/min ramp-up rate for (a) 30 minutes, (b) 1 hour, (c) 2 hours.

4.4. Conclusive Remarks

The isothermal sintering of pure chromium at 1150°C in purely reducing (H_2) atmosphere was investigated to produce low porosity chromium pellets and reveal the influence of variables affecting the density, porosity and microstructure of chromium pellets.

1. During the pelletising of chromium compacts, binder-free pellets achieved a higher density and lower porosity than their binder-containing counterparts. Paraffin wax produced pellets twice as porous as PVA pellets. Although exhibiting a slightly higher porosity, pellets pressed with an addition of 10 wt. % PVA has a similar density to binder-free Cr pellets.
2. During the sintering of pellets in dry hydrogen with added 20 wt.% PVA, non-densifying mechanisms were found to prevail, with pellets exhibiting shrinkage and increased porosity, except for those held for two hours. Quantitative and microstructural analyses revealed that the rate of heating (10°C/min) to the isothermal holding temperature, in addition to causing equipment failure, did not lead to dense pellets.
3. Pellets sintered with added 10 wt.% PVA and a lower rate of heating (1°C/min) were shown to be significantly lower in porosity and higher in density than their 20 wt. % PVA counterparts. SEM micrographs showed particles entwined with each other into large clusters, with smooth neck regions separating them. Holding times of one and two hours showed similar porosity and density results, with the lowest porosity (11%) and a density (6.868 g/cm^3) obtained after two hours of sintering.
4. Pure chromium also exhibited good sinterability with low heating-up rate of 1°C/min. The highest density (6.801 g/cm^3) and lowest porosity (10.24%) were obtained after two hours of isothermal holding.

Thus, overall paraffin wax should not be used as binding agent to achieve low porosity chromium pellets. Despite its well-known brittleness, pure chromium has shown good pressability and sinterability behaviour. At the pelletising stage, binder-free chromium pellets were denser than PVA binder containing pellets, which also showed a loss of density with increased applied force. During sintering, pure chromium pellets achieved a high density, comparable to that of 10 wt. % PVA containing chromium pellets, which performed better than their 20 wt.% PVA Cr pellets counterparts. Most importantly, pure chromium achieved the lowest porosity for the same holding time and heating-up rate (two hours, 1°C/min). These findings infer that at 1050°C in pure hydrogen, high density and low porosity sintered chromium pellets are best obtained without the addition of a binding agent, but this comes at the expense of a longer holding time (two hours).

Chapter 5 Oxidation of Chromium and Chromium Rich Steels under SOFC operating Conditions

« Traverser les montagnes, les rivières, s'il le faut les tempêtes du désert, pour toi je donnerai ma vie »

This chapter aims to study the chromium oxide growth and chromium evaporation from pure chromium sintered pellets and two ferritic stainless steels, Crofer 22H and K41, at 700°C. The study will also investigate how pre-treatment methods affect the oxidation kinetics of the steels. Finally, the reaction rates will be determined and used as input values to the model that will be presented in Chapter 6.

5.1. Introduction

Increasingly, ferritic stainless steels (FSSs) are being used as the materials for solid oxide fuel cell (SOFC) interconnects. This is due to their oxidation resistance at high temperatures, coefficient of thermal expansion (CTE) compatibility with the ceramic fuel cell components, availability, low cost, and good malleability in the fabrication process [21]. FSSs contain chromium (Cr), which, in the presence of air, is converted to chromium oxide, also called chromia (Cr_2O_3). This forms a passivation film protecting against oxidising and corrosive environments. It was established that a reservoir that is higher than 17 wt.% [Cr] in Cr-alloys is necessary for the SOFC interconnect applications in the temperature range of 700°C to 850°C [17,174]. However, the excessive growth of the oxide and chromium evaporation remains a technical challenge for the chromia forming alloys, as this leads to the degradation of the interconnect and negatively impacts SOFC cathode performance, as discussed in Chapter 2, section 2.3.4 [99].

In the SCORED 2.0 project that was described in Chapter 1, Crofer 22H, fabricated by ThyssenKrupp VDM, and K41, produced by Aperam, were the ferritic stainless steels that were supplied as part of the project and selected for oxidation and evaporation studies. The initial Cr concentration in those steels varied between 18 and 22 wt.% (see Chapter 3). The pure chromium pellets that were prepared and sintered in Chapter 4 were also exposed to dry and wet air oxidative atmospheres. A study of the literature showed that previous investigations on several FSSs, including Crofer 22H and K41, were conducted at 800°C and above. However, in line with the reduction of the SOFC operating temperature (Chapter 1), a further investigation of the oxidising chromium behaviour is necessary, as well as a test of the candidate materials at lower operating temperatures. This chapter addresses the oxidation behaviour of Cr and Cr-rich steels under SOFC cathode conditions at 700°C. The experiments were carried out in a horizontal tubular quartz furnace (see Chapter 3). In the

first part of this chapter, the oxidation results from sintered Cr pellets were exposed to dry and wet oxidising atmospheres to reveal the comparative behavioural kinetics of chromium at 700°C. The second part of this chapter focuses on the oxidation and evaporation of two selected Cr-rich alloys under humidified air exposure at 700°C.

5.2. Oxidation of Chromium Pellets at 700°C

5.2.1 Gravimetric and Evaporation Measurements in Dry and Wet Air

The isothermal oxidation kinetics, which are represented by the mass gain as a function of time and the rate of mass change as function of time for the fabricated sintered Cr pellets, are presented in Fig. 5-1 and Fig. 5-3. The pellets were exposed to 700°C with 1.0 L/min flow of synthetic dry air of composition 78% N_2 + 22% O_2 (termed 'dry air'), and in a typical SOFC cathode side environment, i.e. synthetic air with the addition of 3% H_2O (termed 'wet air') for a duration of up to 250 hours. Each data point represents the average of three samples after three tests. (i.e. the average of 9 data points).

From the inference of chapter 4 in terms of low porosity and high density, binder-free pellets were put forward for the exposure tests. However, 10 wt.% PVA containing Cr pellets were also briefly exposed to the conditions described above but showed almost identical results to the binder-free pellets, which suggested that after the sintering process, their small difference in density and porosity as compared to binder-free pellets did not affect the oxidation kinetics of the Cr pellets at 700°C. Therefore, only binder-free pellets results are presented here.

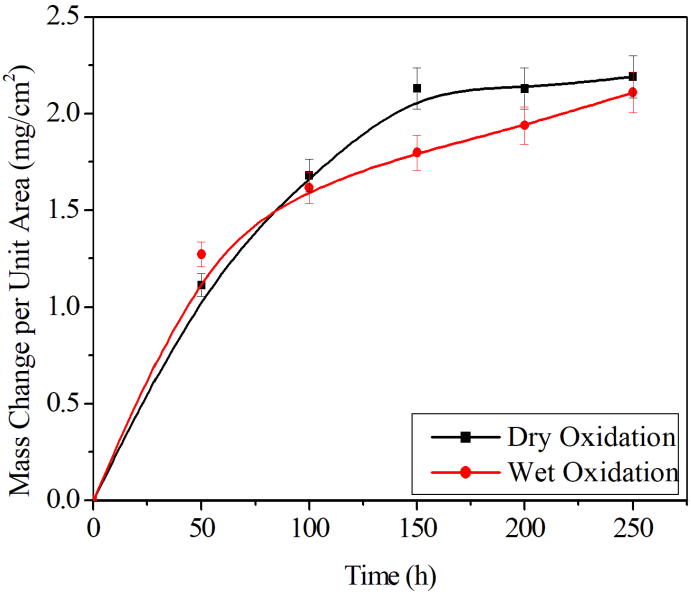

Figure 5-1. Discontinuous mass gain measurement for no-binder Cr pellets in dry air and wet air at 700°C for 250 hours.

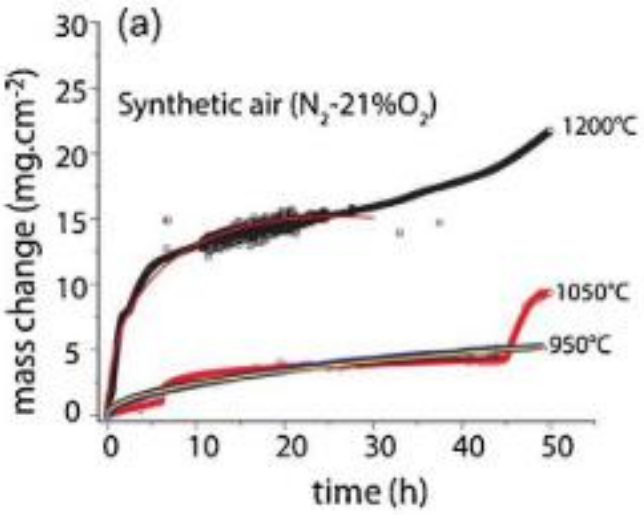

Figure 5-2. *Dorchech et.al* [147] mass gain curves during isothermal oxidation of chromium in dry air at 950°C, 1050°C and 1200°C.

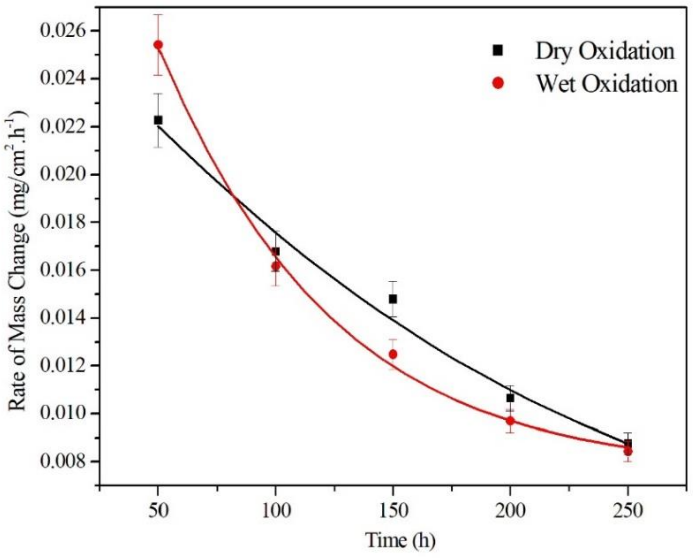

Figure 5-3. Rate of mass change of binder-free Cr pellets exposed to dry air and wet air for 250 hours at 700°C.

After 50 hours, the chromium pellets that were oxidised in dry air showed a lower mass gain of 1.11 mg/cm^2 in comparison to the paralinear mass gains of 4.49, 9.37 and 21.7 mg/cm^2 at 950°C, 1050°C and 1200°C, respectively, for the same amount of time (Fig. 5-2), as reported by Dorchech *et al.* [147]. Up to 150 hours, these pellets showed a strictly parabolic mass gain high rate of mass change (Fig. 5-3), which indicated that there was a formation of Cr_2O_3 on the pellets' surfaces. This was similar to the results of Ref. [175] after 24 hours of exposure in the same conditions. After 150 hours, the samples reached a near plateau and had an overall mass gain of 2.19 mg/cm^2 after 250 hours, which implied the finalisation of the passivation layer build-up where the Cr_2O_3 layer prevented further species diffusion.

Up to 100 hours, the chromium pellets that were oxidised in wet air exhibited a parabolic rate growth, which suggested that as with oxidation at higher temperatures [176], diffusion was the rate-determining step in the initial stages of the oxidation process of chromium at 700^{o}C.

The pellets displayed a slightly higher mass gain than the pellets that were oxidised in dry air up to 50 hours. However, the slope of the mass gain decreased following the first 50 hours of oxidation, which pointed at either a slowing down of oxidation, or, more probably a balance with chromic volatilisation. No mass loss was observed, which suggested an overall dominance of the growth of the oxide over its consumption. After 100 hours, a near linear mass gain was observed with a slightly lower overall mass gain than the pellets that were oxidised in dry air, as the values averaged 2.11 mg/cm^2 over 250 hours. This balance of the gain can be accredited to a continuous Cr diffusion and the resulting oxidation, which compensates for the Cr evaporation that was induced by the oxidation of chromia into a gaseous species. Opila *et al*. [177] confirmed that below 900°C, $CrO_2(OH)_2$ is the dominant forming species. This is expressed through the oxidation of chromia as follows:

$$Cr_2O_{3_{(s)}} + O_{2_{(g)}} + H_2O_{(g)} \leftrightarrow CrO_2(OH)_{2_{(g)}}$$ Equation 5-1

The positive mass gain balance that was obtained contrasts with results from Pujilaksono [175], who reported a negative balance in 60%O_2 + 40% H_2O at 700°C during the early stages of oxidation. Therefore, it can be inferred that pure chromium exposed to a lower humidity (dry air with 3% H_2O) develops a paralinear behaviour where the oxidation of Cr prevails over its evaporation. However, the presence of humidity accelerates the oxidation kinetics, as shown in the case of the aforementioned work [175], reflected in a breakdown of the protective oxide.

5.2.2 Morphology and Composition of Samples

The post-exposure sample surface micrographs using the backscattered electron mode and element quantification tabulation after isothermal oxidation in dry and humidified atmospheres are shown in Figure 5-4. and Figure 5-5., respectively. The element quantification was obtained through EDS mapping, and the values that were reported were

calculated using the average from three repeated experiments and three samples per test (9 data points) (table 5-1 and 5-2).

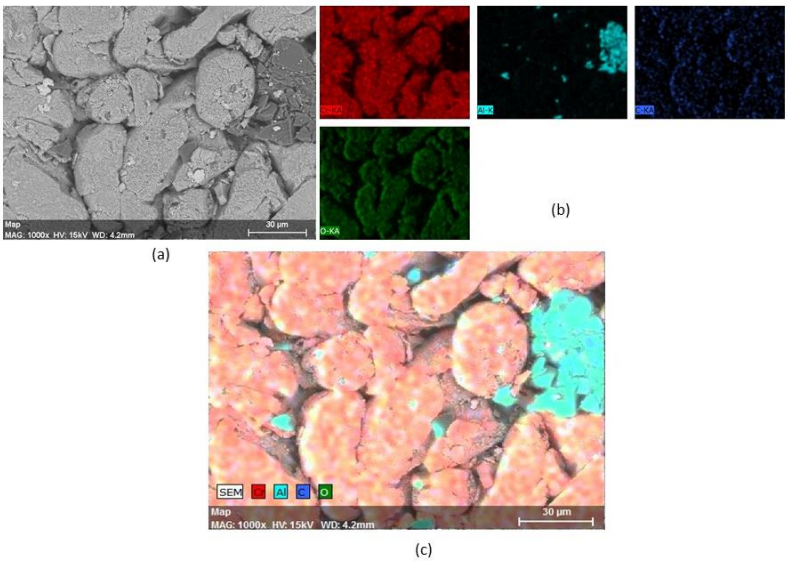

Figure 5-4. SEM images (a), EDS element mapping (b, c) after exposure of pure Cr pellets at 700 °C for 250 hours in dry air. (b) shows elemental mapping of Cr (red), aluminium (light blue), carbon (dark blue) and oxygen (green). Scale bars are shown in white at 30 µm.

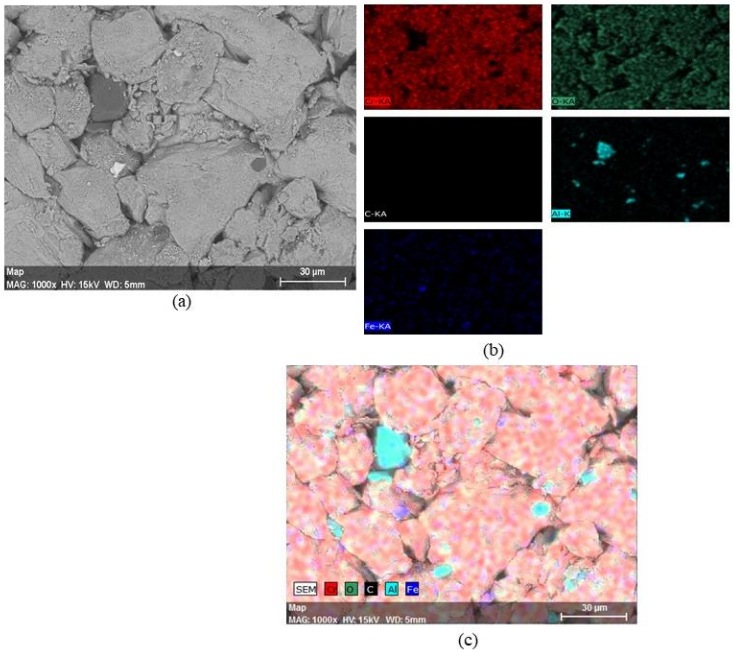

Figure 5-5. (a) Surface SEM images, (b, c) EDS element mapping, (c) and (d) element quantification tabulation after exposure of no binder pellets at 700°C for 250 hours in wet air.

(b) shows elemental mapping of Cr (red), aluminium (light blue), carbon (black) and oxygen (green) and iron (Fe). Scale bars are shown in white at 30 μm.

Table 5-1 Element quantification in Cr pellets tabulation after exposure at 700 °C in dry air (from surface SEM-EDS).

Element	**Normalised Relative Concentration [wt.%] Before Dry Oxidation**	**Normalised Relative Concentration [wt.%] After Dry Oxidation**
Chromium	53.71	66.52
Oxygen	32.09	24.25
Aluminium	11.20	4.96
Carbon	3.00	4.27

Table 5-2 Element quantification in Cr pellets tabulation after exposure at 700 °C in wet air (from surface SEM-EDS).

Element	**Normalised Relative Concentration [wt.%] Before Wet Oxidation**	**Normalised Relative Concentration [wt.%] After Wet Oxidation**
Chromium	69.18	59.50
Oxygen	25.23	31.98
Aluminium	2.83	3.30
Carbon	2.43	4.75
Iron	0.33	0.47

The grain structure of the metal is similar in both atmospheres, but varied grain to grain diameters were observed with measured diameters ranging between 24 μm to 37 μm, and 19

μm to 53 μm in in dry and wet air, respectively. After 250 hours, the oxide scales appeared smooth in both atmospheres and presented no evidence of cracks or scale spallation at this temperature. This is in good agreement with the 24 hours results that were reported in [175].

A distinct difference was observed between the amounts of chromium and oxygen in dry and humidified oxidising atmospheres. In contrast to dry oxidation, less chromium and more oxygen were apparent on the surface of the samples that were exposed to a humidified oxidising atmosphere. This could be accredited to the steam-induced evaporation of chromium as chromium oxyhydroxide $CrO_2(OH)_2$, which changed the oxidation rate from parabolic to paralinear. Similarly, there was an increase in the amount of aluminium (Al) and carbon (C) post-exposure on the humidified O_2 pellets surface. This pointed towards a transport of these species towards the pellet surface where accelerated kinetics prevailed. In addition, there were increased amounts of iron, which corroborated the thermodynamic modelling of the system that will be presented in Chapter 6, predicting iron oxide formation at 700°C.

5.2.3 Kinetics of Pure Chromium Oxidation

The denuder technique that was described in Chapter 3 was used to measure the vaporisation of chromium from pure chromium pellets at 700°C in wet air. The results were analysed using UV-spectrophotometry. The post-test analyses revealed that no evaporated chromium was collected during the dry air exposure, and due to the similarity of the mass gain results between the binder-free and binder-containing pellets during the exposure to wet air, only the binder-free pellets were tested.

The oxidation of metals or alloys is generally described as following a parabolic time dependence, as expressed by Pilling and Bedworth's equation [176]:

$$\left(\frac{\Delta m}{A}\right)^2 = k_p'' t + C \quad \text{Equation 5-2}$$

where Δm is the mass change of the oxidised sample, A is the surface area of the sample, kp" is the parabolic rate constant, t is the exposure time, and C is a constant.

However, it was shown that for chromium and Cr alloys, the observed oxidation was combined with the evaporation of Cr (III) gaseous species. This reportedly led to a combination of a simultaneous parabolic weight gain and linear evaporation rate of Cr over the exposed samples above 900°C [5, 6]. In the present study, the evaporation of the Cr was measured at 700°C in wet air. A similar paralinear behaviour was observed (Figure 5-1.), and balance of the expression of the oxidation kinetics in dry and wet air must account for the mass loss in vaporisation. This was mathematically expressed by Tedmon [7] as follows:

$$\left(\frac{\Delta m}{A}\right) = \left(k_p'' t\right)^{1/2} - k_v t \qquad \text{Equation 5-3}$$

where k_v the volatilisation rate constant.

The results of the Cr evaporation test of the binder-free pellets that were exposed to wet air are presented in Figure 5-6 and Figure 5-7. They show the plot of the Cr evaporation per unit area and Cr evaporation rate as a function of time under isothermal conditions, respectively. As it can be seen on Figure 5-7, after 100 hours, the evaporating Cr rate levelled off and the amount of Cr collected approximated linearity (Figure 5-6). This settling of the rate implies that evaporation though may continue with time, will be low, which is why the experiments was limited to 192 hours. A total value of 0.107 mg/cm^2 of evaporated Cr was recorded after 192 hours of exposure. The Cr pellets initially showed a high evaporation rate, which slowed and settled with time. This contrasted with the higher mass gain that was observed after 50 hours (Figure 5-1.) of exposure. Therefore, the evaporation data is important because it determines the mass that was lost due to the Cr volatilisation during the oxidation of chromia (Eq. 5-1), and subsequently, establishes a more accurate mass gain profile of the Cr pellets.

Figure 5-8 presents the corrected mass gain curve for the Cr pellets in wet air over 250 hours, accounting for Cr mass loss by evaporation. The corrected mass gain was determined by adding the evaporated mass of Cr collected by the denuder tube from the overall measured mass gain of the samples. Since no Cr was collected in dry air experiments (section 5.2.1), the mass gain curve remained the same. The corrected mass gain for Cr pellets oxidised in wet air for 250 hours was estimated to be ± 2.00 mg/cm^2 instead of 2.19 mg/cm^2, which is a difference of 0.19 mg/cm^2. This demonstrates the limitations of sole mass gain measurements, in that the Cr loss through evaporation reduced the overall mass gain, which could lead to a modification of the overall kinetics in other oxidising conditions, allowing for a misinterpretation of the chromia growth. Not accounting for Cr evaporation, which has been the case in a number of publications [147,170,178][147,169,177] also questions the accuracy of published oxidation kinetics data.

The oxidation kinetics were determined by fitting the mass gain curves (Figure 5-1., and Figure 5-8) with Eq. 5-3. Regarding the pellets that were exposed to dry air, no mass loss was recorded during the exposure test, and the Cr collection denuder test revealed no presence of the chromium species. This confirmed that at 700°C, water vapour is necessary to induce the volatilisation of chromium species. The occurrence of a near plateau after 150 hours of isothermal exposure of the pellets prevented a calculation of the parabolic rate constant over the 250 hours of testing. Therefore, the parabolic rate constant k_p of pure Cr pellets in the dry air atmosphere at 700°C was estimated for the first 150 hours as 3.63 x 10^{-18} g^{2}cm^{-4} s^{-1} (or 1.90 x 10^{-9} gcm^{-2} s^{-1}). Pujilaksono *et al.* [179] reported mass gain curves up to 24 hours in dry oxygen (O_2), for which the k_p was estimated as 6.44 x 10^{-14} g^{2}cm^{-4} s^{-1} (or 2.54 x 10^{-7} gcm^{-2} s^{-1}), which is a magnitude difference of four, and Gulbransen et.*al* [178] estimated a k_p of 8.22 x 10^{-15} g^{2}cm^{-4} s^{-1} (or 2.87 x 10^{-7} gcm^{-2} s^{-1}), after two hours of the Cr pellets' exposure to dry O_2, which is a magnitude difference of three with the results presented here. Pujilaksono *et al.*

[179] affirmed that the k_p value discrepancies in this temperature range are due to the pre-treatment of samples. However, it was suggested that these values may be the consequence of the time dependency of k_p, which, in the case of pure chromium, appear to decrease as the exposure time increases. When converted to thickness, the overall average mass gain of the pellets that were oxidised in dry air corresponded to an oxide thickness of 75 µm after 250 hours. This is in good agreement with the EDS quantification in Table 5-1, which showed that post oxidation, the chromium content on the Cr pellets surface increased.

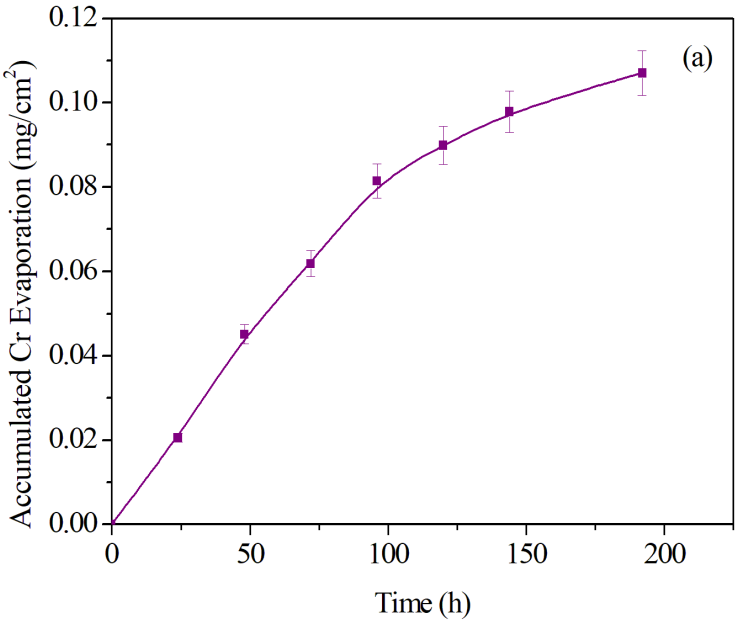

Figure 5-6 Accumulated Cr evaporation as a function of time for binder-free pellets exposed to 3 % H_2O wet air at 700°C exposed.

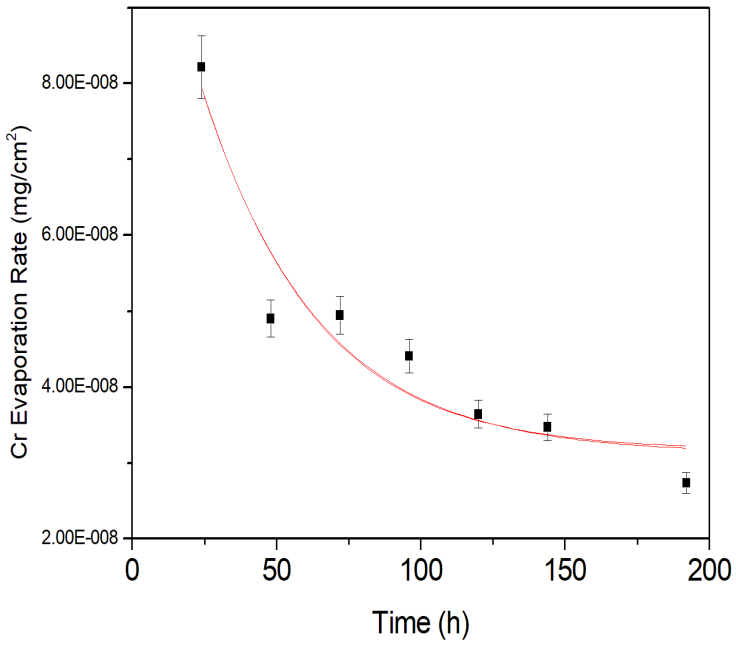

Figure 5-7 Cr evaporation rate as a function of time for the binder-free pellets exposed to wet air at 700°C (from Fig.5-6)

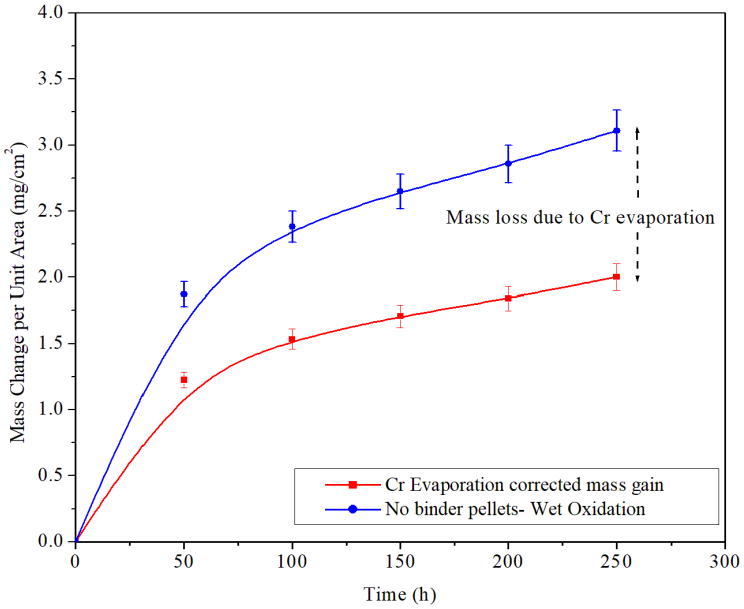

Figure 5-8. Corrected mass gain for binder-free Cr pellets in wet air at 700°C. The mass loss due to evaporation is highlighted.

The corrected mass gain of Cr pellets oxidised at 700°C in wet air presented in Figure 5-8, is supported by the previous Cr evaporation data (Figure 5-6 and Figure 5-7) which

demonstrated that a simultaneous mass loss due to Cr volatilisation was occurring during the oxidation, resulting in a lower mass gain profile measured. In addition, a higher mass gain after 50 hours of exposure was observed, in comparison with Cr pellets oxidised in dry air (Figure 5-1.), indicating that accelerated kinetics prevailed. This was in good agreement with observations from Pujilaksono *et al.* [179] in more humidified atmosphere (60 % O_2 + 40 % H_2O, 700°C). Thus, the parabolic rate constant kp of pure Cr pellets in wet air atmosphere at 700°C was estimated using the corrected mass gain curve (Figure 5-8) as 3.24 x 10^{-24} g^2cm^{-4} s^{-1} (or 1.80 x 10^{-12} gcm^{-2} s^{-1}), which was six orders of magnitude higher than the kp estimated in dry air atmosphere. The volatilisation rate constant (kv) was calculated from the linear slope of the accumulated Cr evaporation plot after 192 hours as 5.32 x 10^{-21} g^2cm^{-4} s^{-1} (or 7.30 x 10^{-11} $gcm^{-2}s^{-1}$), against 7.78 x 10^{-20} g^2cm^{-4} s^{-1} (or 2.79 x 10^{-10} gcm^{-2} s^{-1}) estimated by Pujilaksono *et al.* [179] after 24 hours. Pujilaksono *et al.* [179] determined k_v on the basis of the differential mass change in humidified and dry air atmospheres and estimated 1.2 x 10^{-6} $g^2cm^{-4}s^{-1}$ or (1.09 x 10^{-3} gcm^{-2} s^{-1}), which is a very fast evaporation. This method may be misleading, as different samples were used for each experiment, which may have increased discrepancies induced by sample preparation, impurities, structure of the chromium substrate, etc. [147]. In addition, the authors' estimation only covered 24 hours of pure Cr pellets oxidation in 60 % O_2 + 40 % H_2O, in which case a steady state had not been reached according to Figure 5-1 and extrapolation may be subjected to considerable error from fitting the data. The denuder tube method used here is more accurate as mass loss due to evaporation was directly measured via Cr collection, and a much larger timespan was considered. Besides this, the humidity level in Pujilaksono *et al.* [179] work was very high and unlikely for SOFC cathode operation. The summary observed properties are tabulated in Table 5-3, whilst the estimated rate constants of Cr pellets in dry and wet air at 700°C are summarised in Table 5-4.

Table 5-3. Comparative Measured Properties of Cr samples post-oxidation against literature at 700°C.

Materials	**Atmosphere**	**Temperature °C**	**Time h**	**Colour**	**Cracking or Spallation**	**Rate law**	**Reference**
Cr Binder-free pellets	Dry air	700	150	Grey-green	No	Parabolic	Present work
Cr Binder-free Pellets	Wet air	700	250	Grey-green	No	Paralinear	Present work
Cr Metal-strips	Dry (O_2)	700	6 hr	Straw	No	Parabolic	[178]
Cr Binder-free Pellets	Dry (O_2)	700	24h	-	No	Parabolic	[179]
Cr Binder-free Pellets	60 %O_2 + 40 wt.% H_2O	700	24h	-	No	Paralinear	[179]

Table 5-4. Comparative kinetic parameters determined for pure chromium oxidation against literature at 700°C

Materials	**Atmosphere**	**Temperature, °C**	**Time, h**	k_p **($g^2.cm^{-4}s^{-1}$)**	k_v **($g^2.cm^{-4}s^{-1}$)**	**Reference**
Cr Binder-free pellets	Dry air	700	150	3.63×10^{-18}	-	Present work
Cr Binder-free Pellets	Wet air	700	250	1.80×10^{-12}	5.32×10^{-21}	Present work
Cr Metal-strips	Dry (O_2)	700	6 hr	8.22×10^{-15}	-	[178]
Cr Binder-free Pellets	Dry (O_2)	700	24h	6.44×10^{-14}	-	[179]
Cr Binder-free Pellets	60% O_2 + 40 wt.% H_2O	700	24h	7.78×10^{-20}	1.1×10^{-6}	[179]

5.3. Influence of Surface Finish on Oxidation Kinetics of Crofer 22H

In oxidation testing of metal interconnects, samples are pre-treated to remove existing oxides and impurities. This step is important, as it creates a well-defined starting point that will influence the oxide growth and adhesion of a protective coating. Grinding and cleaning are the most frequently used preparation methods, but little evidence has been reported comparing their influences on the oxide growth experienced by steels exposed to high temperatures. Grinding involves the use of abrasive discs to descale the steel, also removing any damaged or deformed regions from the material. Cleaning, alternatively, is a degreasing method in which an ultrasonic bath of alcohol is used to remove contaminants from the surface of the steel through a cavitation process. Some published works report the use of grinding with silicon carbide (SiC, grit P600 to P1200) [39,175], while some report the use of degreasing in acetone [66,113,180], and others report the combination of both methods [110,181]. In this work, triplicates of water-jet-cut Crofer 22H coupons were treated by these two methods (see Chapter 3 for full details of the procedure) and subsequently oxidised at 700°C in wet air, with an air flow of l L/min for up to 200 hours. This was done to evaluate the influence of the grinding and cleaning sample preparation methods on the oxidation behaviour of steel.

5.3.1 Gravimetric Measurements

The continuous gravimetric measurements for the exposed Crofer 22H samples are presented in Figure 5-9 as an average of three tests. Samples ground with silicon carbide (SiC) grit P400 exhibited higher mass gain than samples polished with SiC grit P1200 and the highest mass gain overall. After 200 hours of exposure, SiC grit P400 ground steel recorded a total mass gain of 0.05 $mg.cm^{-2,}$ followed by SiC grit P1200 ground steel with a mass gain of

0.0345 mg.cm^{-2}. The steels chemically cleaned in an acetone ultrasonic bath recorded a total mass gain of 0.025 mg.cm2 after 200 hours. The lowest mass gain was achieved by samples tested 'as received', totalling 0.021 mg.cm^{-2}. This shows that the use of 'as received' samples for oxidation testing will result in the under-estimation of parameters, due to pre-existing (but undefined) oxide layers having formed under unknown conditions over arbitrary time spans.

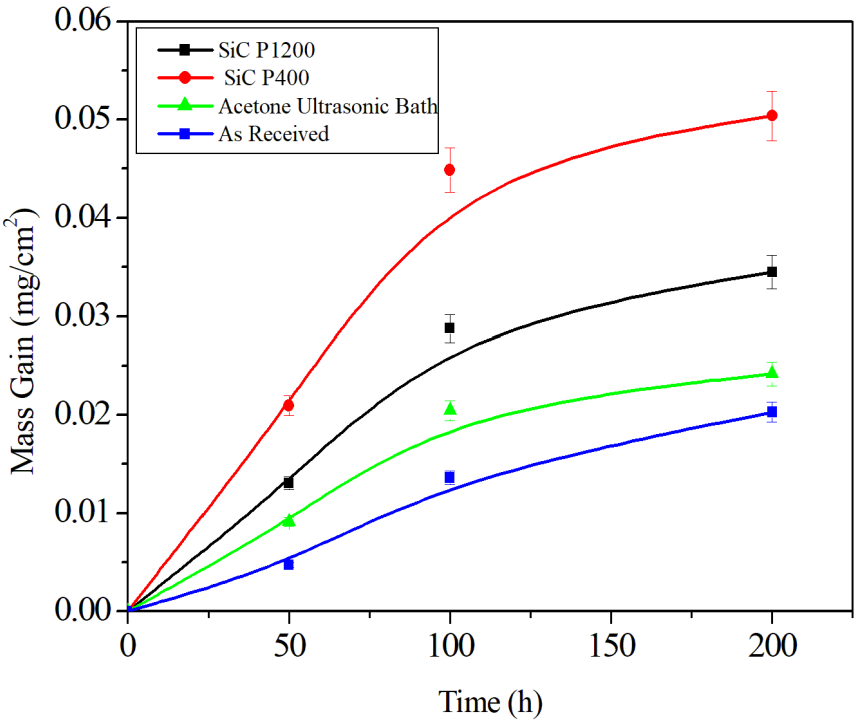

Figure 5-9. Comparison of mass gain profiles over time of Crofer 22H samples prepared with different surface treatment methods.

5.3.2 Contact Angle Analysis

The effects of the different preparation methods used on the steel samples on the contact angle of water are shown in Figure 5-10. To recall, the contact angle reflects the wettability of a solid surface, which in turn provides an indication of the cleanness of the samples post preparation-treatments (see Chapter 3 for method description). The SiC ground and 'as received' samples exhibited lower contact angles post exposure, with 80.03°, 40.99° and

31.80° for grit P1200, P400 and ‘as received’, respectively. In contrast, Crofer 22H samples ultrasonically cleaned in acetone exhibited a higher contact angle post-oxidation. The contact angle of P400 ground samples decreased by slightly more than half, while that of P1200 ground steel degraded by approximately only 6%. Inversely, the contact angle of acetone cleaned steels increased by approximately 16.61%.

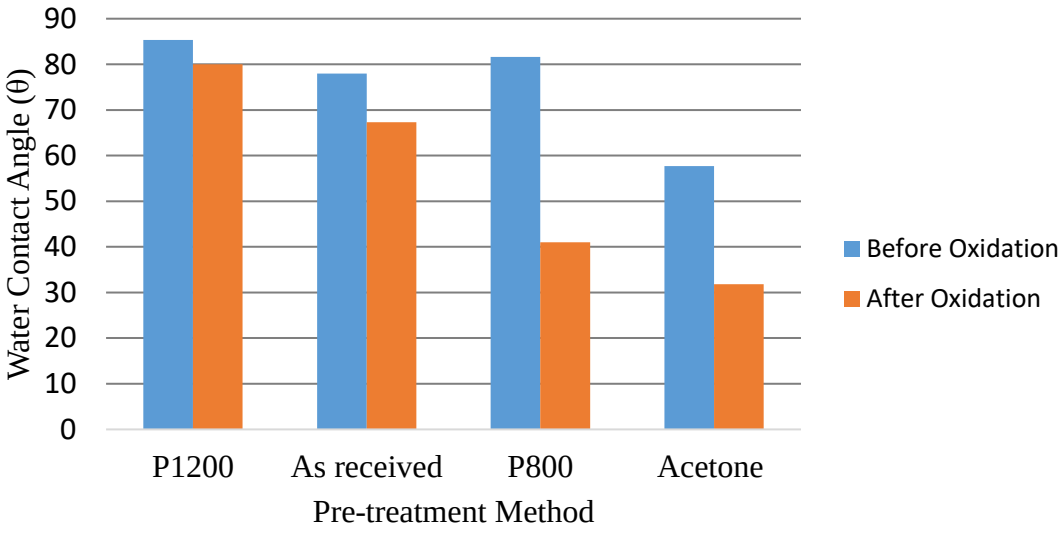

Figure 5-10. Comparison of contact angles of Crofer 22H treated with different preparation methods, against before and after 200 hours oxidation in wet air.

5.3.3 Microstructural Analysis

Surface SEM analyses of the Crofer 22H samples post-oxidation at 700°C in wet air are presented in Figure 5-11, with corresponding EDX mapping analyses. Surface spallation was observed on the ‘as received’, non-treated oxidised samples. EDX mapping analyses revealed the surfaces to be covered in $MnCr_2O_4$ spinel crystals, with spalled void areas enriched with manganese (Mn). The edges of these areas were composed of different oxides, $MnCr_2O_4$ and $(Fe, Cr)_2O_3$, with traces of non-conductive silicon (Si). Oxidised samples prepared via

acetone ultrasonic bath and SiC grinding were covered with carbon (C) rich fragments (5.82 wt.%), which appeared to have detached from the surface. These carbon debris appeared to be due to the aforementioned preparation methods rather than the initial carbon content of the steel (0 to 0.030 wt.%). While the debris were still present after the initial hours of oxidation (200 hours), the observed detachment from the surface suggested that they might spall off during the later stages of oxidation. However, they may cause misleading results in terms of the measured weight gains of the samples and, thus, also in calculating the oxidation kinetics. The surface of SiC grit P1200 ground samples appeared smooth, while SiC grit P400 ground samples showed patches of oxide nodules; these may be linked to surface defects caused by the abrasion. Grabke [49] reported that grinding results in dislocations and development of a grained microstructure directly beneath the surface. Overall, there was some indication that for the purpose of oxidation testing, where measuring oxide kinetics is the aim and accelerated mass gain is required, grinding the sample surfaces with SiC grit P1200 is the most effective preparation method, to which a final polish with diamond paste could be added to obtain a mirror finish surface. This step should be followed by a degreasing and cleaning step, in an alcohol such as acetone or ethanol, to remove carbon and other existing impurities. It is inferred here that using ‘as received’ samples is not recommended for accelerated oxidation testing, due to the possibility of spallation occurring earlier in the oxidation process and the generally unrefined surface conditions.

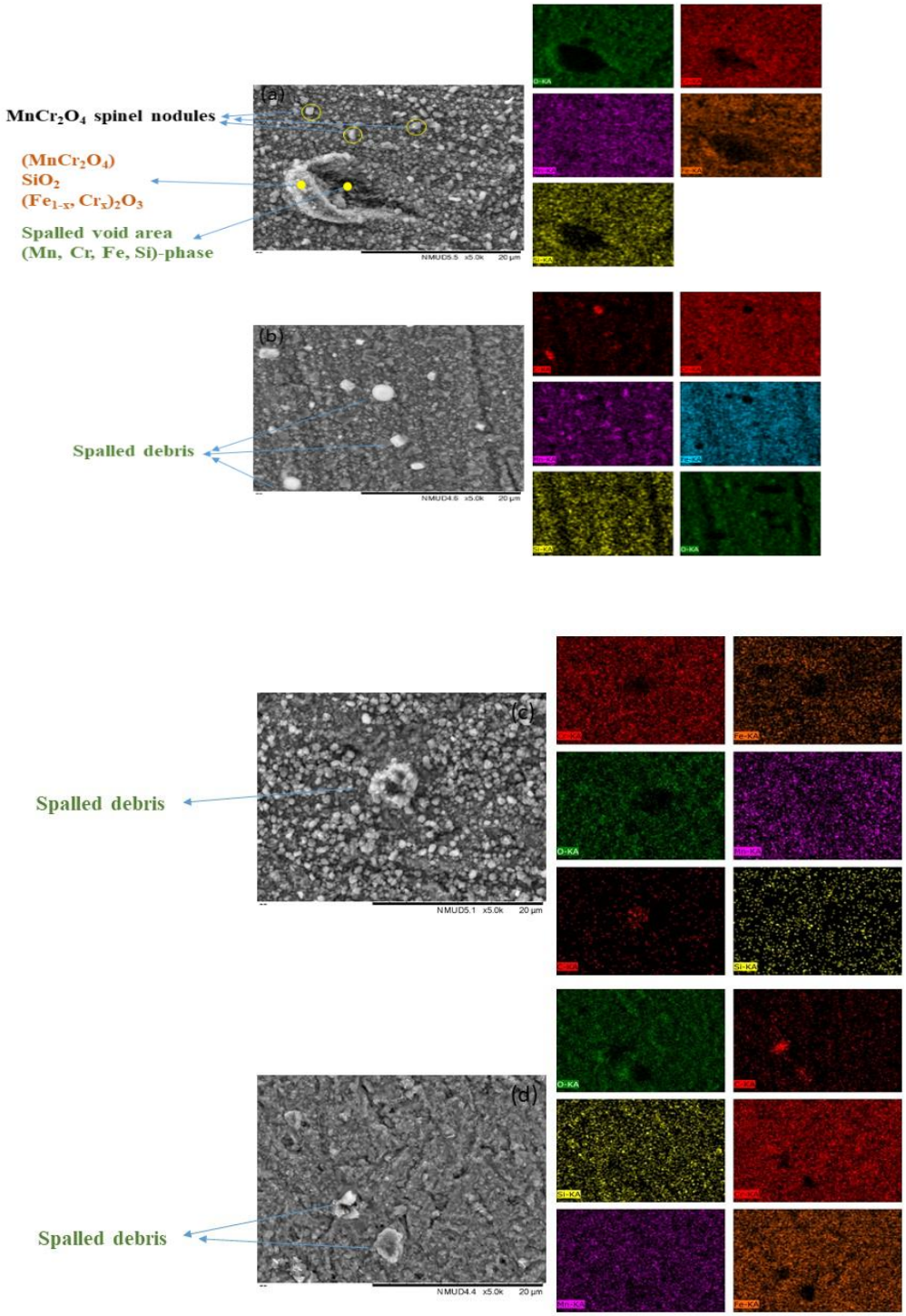

Figure 5-11. Surface plan SEM of Crofer 22H samples pre-treated (a) 'as received', (b) cleaned in ultrasonic acetone bath, (c) ground by SiC P400, and (d) SiC P1200. (a, b) shows elemental mapping of Cr (red), aluminium (light blue), manganese (purple) carbon (red) and oxygen (green) and iron (Fe). (c, d) shows elemental mapping of Cr (red), manganese (purple) carbon (red) and oxygen (green). Scale bars are shown in black at 20 µm.

5.4. Evaluation of Oxidation and Cr Evaporation of Crofer 22H and K41 at 700°C

As part of the project SCORED 2.0, SOFC interconnect candidates Crofer 22H and K41 were selected for long-term discontinuous oxidation study. These high chromium ferritic steels varied between 17 and 24 wt.% in Cr concentration (see Chapter 3) and had been previously investigated by a number of authors at temperatures above 700°C. In the following study, Crofer 22H and K41 ferritic steels were exposed isothermally to 700°C with 1.0 L/min of wet air for a duration of up to 1000 hours.

5.4.1. Gravimetric and Evaporation Measurements

The isothermal oxidation kinetics of the steels in the aforementioned conditions are presented in Figure 5-12 and Figure 5-13, showing the mass change and mass change rate of the samples during the exposure, respectively. It can be clearly seen from Figure 5-12 that both steels experienced a very rapid initial mass gain after only approximately 100 hours of exposure. Up to 500 hours, both steels showed a roughly parabolic oxidation behaviour with mass gains of 0.0958 mg/cm^2 and 0.0967 mg/cm^2 for Crofer and K41, respectively. K41 displayed a higher mass gain rate than Crofer 22H, suggesting it experienced a faster reaction during the initial stages of oxidation. However, at 500 hours, the mass gain rate of Crofer 22H steel caught up with that of K41 steel, after which both steels revealed a change from parabolic to linear-like oxidation behaviour; this kinetic change could be attributed to the presence of humidity and subsequent Cr volatilisation.

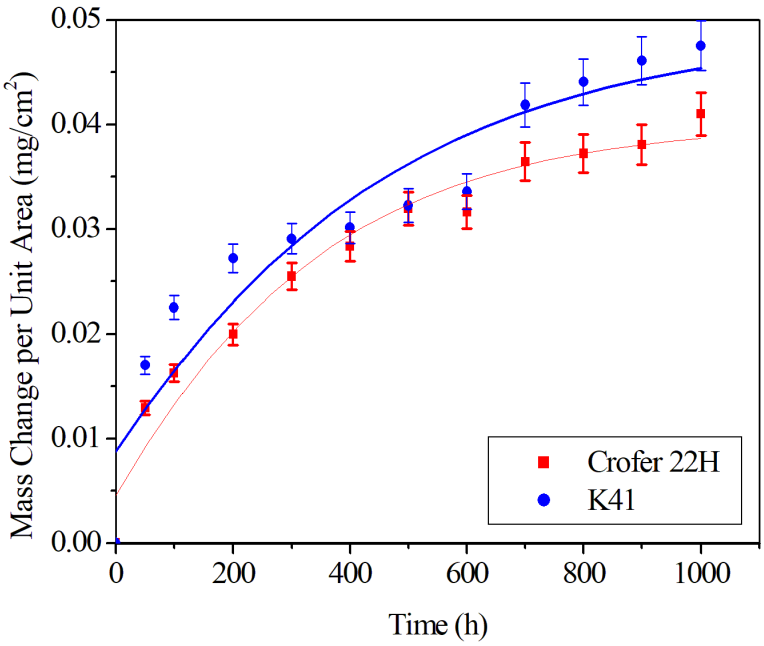

Figure 5-12. Discontinuous mass gain measurements of Crofer 22H and K41 in wet air at 700°C for 1000 hours.

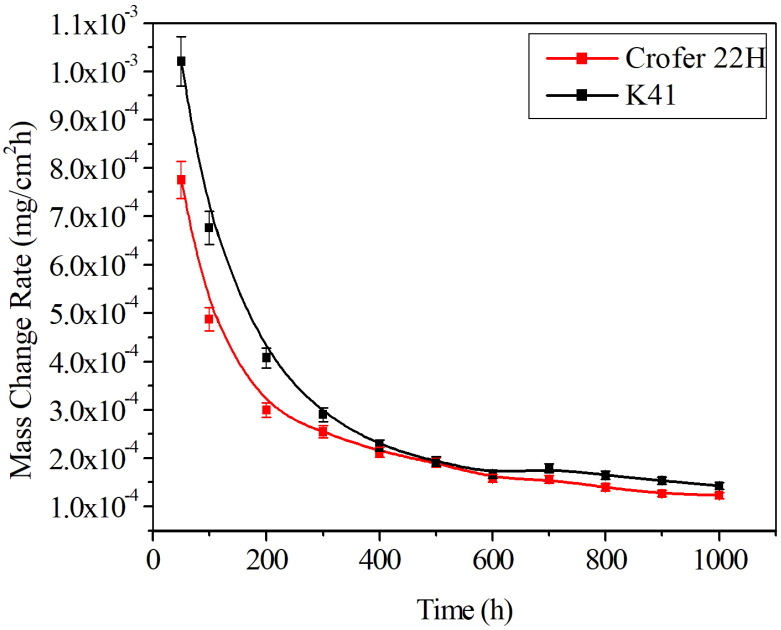

Figure 5-13. Discontinuous mass change rates of Crofer 22H and K41 in wet air at 700°C for 1000 hours.

As observed at 600 hours (Figure 5-12), Crofer 22H recorded a slowing gain, while the mass gain of K41 was minimal, traducing the simultaneous, competing diffusion induced scale growth and linear evaporation occurring within the samples.

This behaviour was also observed by Talic *et al.* [182], who recently oxidised Crofer 22H and K41 (which has been renamed 441) steels at 700°C in dry air for 2000 hours. However, Talic *et al*. did not report a parabolic mass gain of the steels over 2000 hours but, rather, a linear evolution, with 250-hour gaps between measurements. This would support the observation made here previously that the mass gain turns from parabolic to linear, though this was observed for wet atmospheres. In the present study though, sample mass measurements were taken closer to each other (every 100 hours), delivering more detailed portraits of the oxidation behaviour. A similar mass loss on ferritic steels was also observed at 750°C wet air by Windish *et al.* [20].

Vaporisation of Cr_2O_3 remains a complex subject. Various and different condensed phases of volatile Cr species may form upon reacting with oxygen, including CrO_3, CrO_2, and CrO [21]. The formation of these species was only solidly proven to occur at 950°C [21] and little data has been reported for lower temperatures. More importantly, the evaporation study of pure Cr in section 5.2.3 concluded that there was no chromium evaporating from the pellets at 700°C in dry air, which questions the Cr vaporisation, claimed by Talic *et al.* [182], to explain the linearity of their mass measurement results. In this second phase of oxidation, K41 continued to display a higher mass gain, with an ultimate gain of 0.1426 mg/cm^2, compared to 0.1230 mg/cm^2 for Crofer 22H. Sachitanand *et al.* [66] reported that steels with higher manganese (Mn) concentrations displayed higher mass gain. This was not visible in the present study at 700°C, as K41 contains at least the same amount of Mn as Crofer 22H, as per the supplier given composition. The mass gain values reported here are of the same order of magnitude as those of Talic *et al.* [182], also reporting a continuous increase over 1000

hours in dry air oxidation at 700°C. However, in that time, the values obtained by Talic *et al.* [182] were lower (approximately 0.038 mg/cm^2 and 0.023 mg/cm^2) than in the present study, pointing to the accelerated kinetics caused by the presence of humidity. Talic *et al.* also reported, in line with our findings on wet air, that 441/K41 steel showed a faster and higher mass gain than Crofer 22H in synthetic air. Comparing different steels in synthetic dry air at 700°C, Talic *et al.* confirmed that the growth of oxide scales on FeCr-alloys [22] decreases with decreasing temperature of operation. By superimposing the present results with those of Sachitanand *et al.*[66] , who oxidised different FeCr steels, including Crofer 22H, at 850°C in wet air (6 L/min), it can also be affirmed that even in the presence of humidity at a lower temperature, the oxide growth rates of FeCr steels appear to settle with time (Figure 5-13). This corresponds to the attained regime also observed in section 5.2.1, where evaporation and oxidation evolve at a similar rate [19]. However, it was also shown in section 5.2.3 that the mass of Cr lost due to vaporisation needed to be accounted for, to ensure the accuracy of results. Surprisingly, at 850°C, in the same humidity conditions but with a flow rate of 6l/min, Grolig [180] reported a total mass gain of 0.54 mg/cm^2 for 441/K41 steel after 1150 hours of exposure, close to the 0.55 mg/cm^2 reported by Sachitanand *et al.* for Crofer 22H after 1000 hours of exposure. In both cases, we found that, at 700°C, the mass gains of these ferritic steels reported in the present work were approximately six times smaller, depicting a much slower growth of oxide scale at lower operating temperatures, beneficial for SOFC interconnect purposes.

The Cr evaporation corrected mass change profiles for Crofer 22H and K41 steels exposed to wet air at 700°C for 1000 hours, obtained by adding the measured Cr lost by evaporation, are presented in Figure 5-14. The dotted lines represent the Cr loss during the exposure test. Similarly, to the findings on chromium pellets presented in section 5.1, the corrected mass gain for Crofer 22H and K41 steels showed that a concurrent Cr mass loss, due to

volatilisation, was occurring during the oxidation of the steel samples, resulting in the lower mass gain profiles presented in Figure 5-14. It was observed that after 1000 hours, the corrected mass gain was estimated as 0.1095 mg/cm^2 and 0.1291 mg/cm^2 for Crofer 22H and K41, respectively, a difference of uncorrected measurements of 0.0135 mg/cm^2 for both steels. This value is approximately 10 times lower compared to results obtained by Sachitanand *et al.* for Crofer 22H at 850°C and 6 L/min of wet air. This highlights the influence of temperature, but also flow rate, implying that at lower operating conditions, Cr volatilisation from ferritic steels can be greatly reduced.

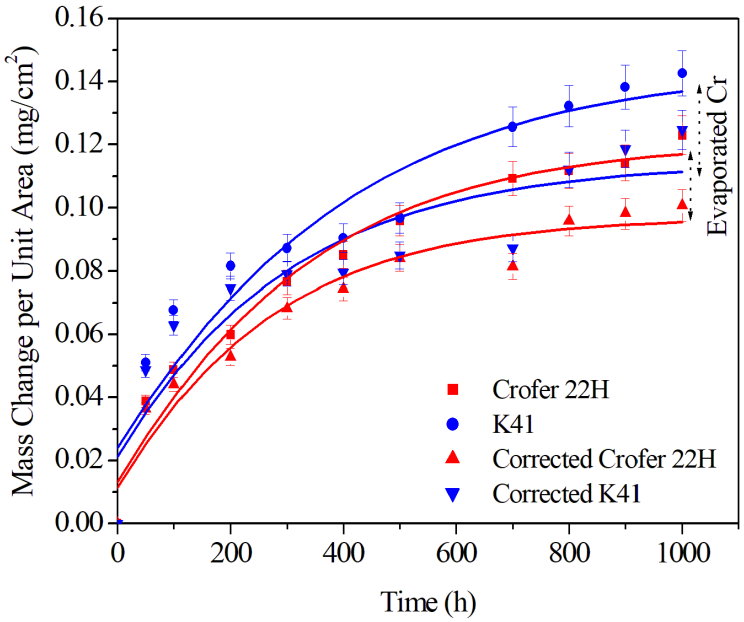

Figure 5-14. Corrected mass measurements of Crofer 22H and K41 in wet air at 700°C for 1000 hours.

The Cr evaporation data is reported in Figure 5-15 and Figure 5-16. These show plots for Cr evaporation per unit area and Cr evaporation rate as a function of time under isothermal conditions, respectively, for Crofer 22H and K41 steels. Crofer 22H exhibited the lowest evaporation (0.0135 mg/cm^2 after 312 hours), while that of K41 was higher by approximately a factor of four (0.0593 mg/cm^2 after 312 hours). The measured values were in good

agreement with Windish (20) in his aforementioned work, where he reported approximately 0.060 mg/ cm^2 for Crofer 22H, after 300 hours of exposure at 750℃. As observed in Figure 5-16. K41 showed a higher evaporation rate than Crofer 22H, and, with both rates decreasing with time. This is in good agreement with Froitzheim *et al.* [24], who explained that at lower flow rates, such as 1L/min, Cr evaporation varied linearly with the flow rate. As per the author's knowledge, no Cr evaporation data have been reported for K41 (441) in the exact conditions presented here. At 850℃, in synthetic air with 3% H_2O flowing at 6 L/min, Grolig *et al.* [180] reported three times the amount collected here at 700℃ that is 0.14 mg /cm^2 after 500 hours of exposure of the steel. While these authors concluded that this amount of Cr evaporation exceeded the requirements for this steel, it is believed that at 700℃, with a lower flow rate (1l/min), Crofer 22H and K41 are suitable candidates for SOFC interconnect material and can be further improved for long-term operation with the addition of protective coating materials, depending on the coating materials used.

The parabolic rate constants k_p for Crofer 22h and K41, in wet air at 700℃, were estimated using the corrected mass gain curves (Figure 5-14) as 3.61×10^{-10} g^2cm^{-4} s^{-1} (or 1.33×10^{-5} $mg^2/cm^{-4}h^{-1}$) and 4.60×10^{-10} g^2cm^{-4} s^{-1} (or 5.30×10^{-5} mg^2/cm^{-4} h^{-1}), respectively. A direct comparison between these values and literature data is not possible due to the differences in exposure conditions (temperature, flow rate, humidity and lack of/or different Cr evaporation measurement techniques). However, the present values are close in magnitude to reported literature data [20, 25, 26]. The volatilisation rate constants (k_v) were determined from the slope of the accumulated Cr evaporation rate plots after 312 hours (Figure 5-16) as 3.93×10^{-25} g^2cm^{-4} s^{-1} (or 3.93×10^{-13} gcm^{-2} s^{-1}) and 8.01×10^{-19} g^2cm^{-4} s^{-1} (or 8.95×10^{-10} gcm^{-2} s^{-1}) for Crofer 22H and K41, respectively. Unsurprisingly, K41 registered a faster Cr evaporation than Crofer 22H. These values are lower than Cr evaporation rates reported in literature. Sachitanand *et al.* for instance, have reported an evaporation rate of

1.30×10^{-14} 19 $g^2cm^{-4}\,s^{-1}$ (or 3.6×10^{-8} $gcm^{-2}\,s^{-1}$) for the steel Crofer 22H (850℃, synthetic air with 3wt.% H_2O, 500 hours of exposure), while Grolig *et al.* [180] reported 1.51×10^{-15} $g^2cm^{-4}s^{-1}$ (or 3.88×10^{-8} $gcm^{-2}\,s^{-1}$) for K41 in the same conditions. Clearly, the differences between the evaporation rates measured in the present work and the aforementioned publications are due to the temperature since the humidity was the same. The estimated rate constants of Crofer 22H and K41 in wet air at 700℃ are summarised in Table 5-4.

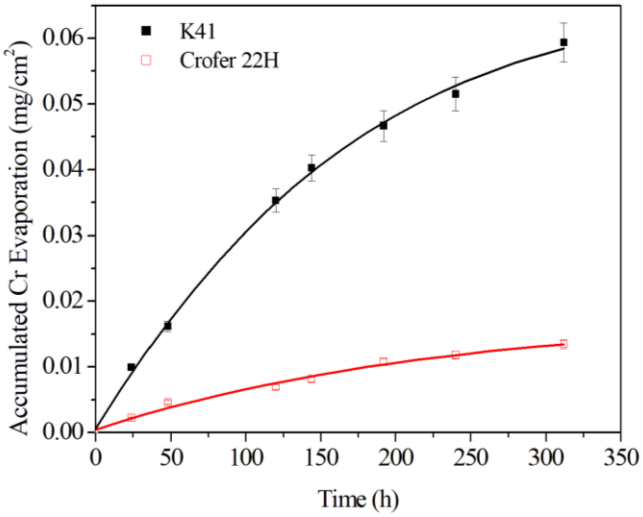

Figure 5-15: Accumulated Cr evaporation and as a function of time for Crofer 22H and K41 exposed to wet air at 700℃.

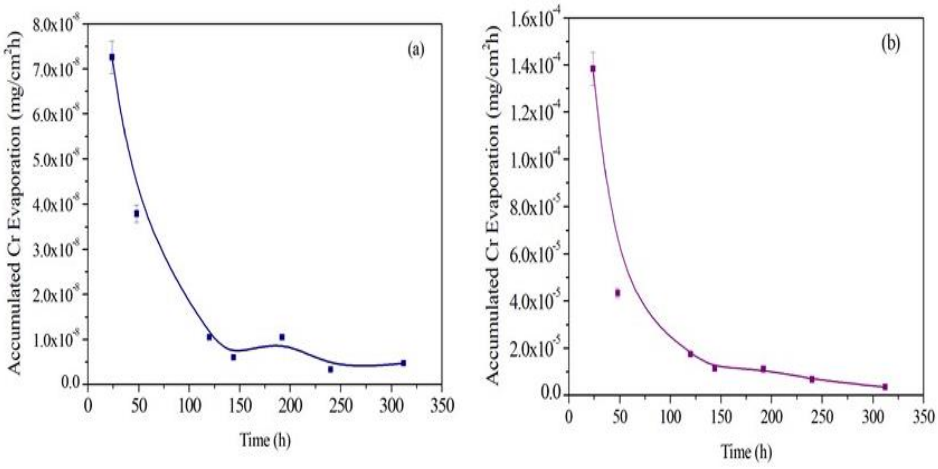

Figure 5-16. Cr evaporation rate as a function of time for (a) Crofer 22H and (b) K41 steels exposed to dry air with 3wt. % H2O at 700℃ for 312 hours.

Table 5-5. Kinetic parameters determined for Crofer 22H and K41 exposed to wet air atmospheres at 700℃.

	$k_p(g^2.cm^{-4}.s^{-1})$	$k_v\ (gcm^{-2}.s^{-1})$
Crofer 22H	1.9×10^{-5}	3.93×10^{-13}
K41	2.14×10^{-5}	8.95×10^{-10}

5.4.2. Microstructural Analysis

The surface microstructures of Crofer 22H and K41 steels before and after exposure tests at 700℃ in synthetic air, with 3% H_2O for 1000 hours, are presented in Figure 5-17.

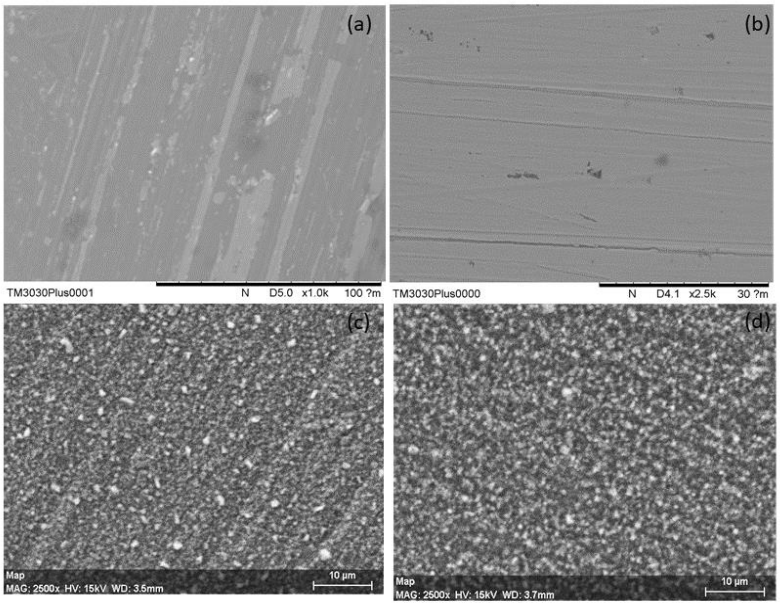

Figure 5-17. Surface SEM images (a, b) before and (c, d) after test exposures of (left) Crofer 22H and (right) K41 ferritic steels to wet air, over 1000 hours exposure at 700℃.

Based on the findings of Section 5.3, the samples were ground with SiC (P1200) and subsequently ultrasonically bathed in acetone and/or IP. Post treatment (a) and (b) are Crofer 22H and K41, respectively, in Figure 5-17, both samples showing surface defects, most likely evidence of the grinding process. Post-exposure surface micrographs (c) and (d) Crofer 22H and K41, respectively, in Figure 5-17 showed the formation of an oxide film through white nodules and grey crystals of oxide distributed arbitrarily over the entire surfaces of both steels after 1000 hours of exposure. While both steels showed a similar oxide morphology, the surface of K41 demonstrated more densely packed nodules, which correlated with the higher mass gains observed in Figure 5-12 and Figure 5-14, while Crofer 22H showed a smaller amount of the fine-sized white particles, more sparingly dispersed across the surface of the steel. Figure 5-18. shows the cross-sectional micrographs of Crofer 22H and K41 after 528 hours of exposure to the described oxidising conditions. Based on the cross section EDX (Figure 5-18.), an oxide scale was identified in both ferritic steels, consisting of (Fe, Mn Cr)$_3O_4$; this differs from published works at temperatures above 700°C [66,180,183] where a duplex scale composed of an outer layer (Mn,Cr)$_3O_4$ on top of a chromium oxide (Cr_2O_3) scale is reported. In the present work, a clear distinction of two scales was not observed. Belma *et.al* [182] who also pointed to the presence of iron (Fe) but equally did not show a distinct Cr_2O_3 layer in their EDX cross sections (although they also agreed to the aforementioned duplex scale) explained that at lower temperatures, fast growing Fe-oxides may appear in place of Cr_2O_3 oxide. Young *et. al* [184] who oxidised the ferritic steel Crofer 22 APU in Ar-4%H_2-20%H_2O reported that at 650°C, a transition from a Cr_2O_3 scale to the formation of Fe-oxides was occurring. These Fe-oxides are reportedly non-protective against oxidation [182,184], which implies that at lower operating temperatures, dense protective coatings would be required to ensure the longevity of the steels. The titanium (Ti) rich internal zone observed in K41 at 800°C in dry air by Jablonski *et al.* [65] was not observed

here, but a silicon (Si) rich sub-zone was observed below the oxide layer on K41 at the scale/metal interface. This was not observed on Crofer 22H. This rich SiO_2-layer was also found by Belma *et al.* [182] Jablonski *et al.* [65], adding to and explaining the overall higher mass gains of the K41 samples.

Being non-conductive, a layer SiO_2 would be detrimental to the Area surface resistance (ASR) of the interconnect component for the long-term operation of the SOFC. The samples showed a minimal difference in thickness at this time, which coincides with the close mass gain displayed in Figure 5-12 and Figure 5-14 at 500 hours. K41 steel oxide appeared slightly thicker at 771.67 nm, against 747.67 nm measured for its Crofer 22H counterpart, a result of the initial faster oxidation kinetics observed. It can also be seen that K41 steel suffered from some spallation, which was observed around the edges of the samples. The spallation seen here was not as severe as that observed by Grolig *et al.* at 850℃ [185].

Cross sectional measurements of oxide thickness were not successfully achieved on the samples subjected to 1000-hour-long exposures, as the oxide layers appeared to disappear upon the polishing of the samples. However, based on reported mass gain trends and the oxide thicknesses measured on samples after 500 hours of exposure, it can be assumed that the thickness would have greatly increased after 1000 hours of exposure (possibly tripled or quadrupled), with K41's oxide film still appearing slightly thicker than that of Crofer 22H.

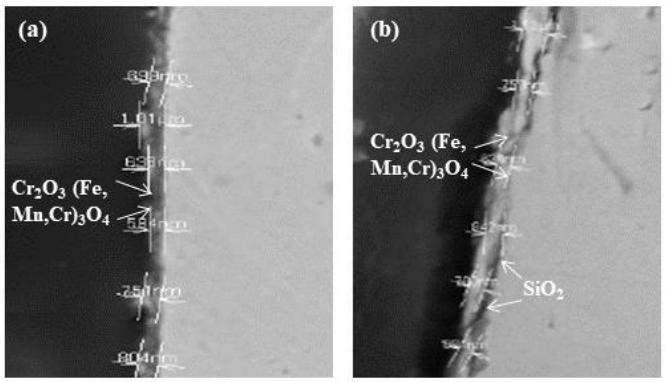

Figure 5-18. Cross section surface SEMs of oxide layer thickness for Crofer 22H (a) and K41 (b) ferritic steels after exposure to wet air for 528 hours.

5.5. Summary

In the first part of the chapter, the isothermal oxidation kinetics of pure chromium at 700℃ in oxidising atmospheres (synthetic dry air, (N_2-20% O_2) and synthetic wet air (N_2-20% O_2 with 3 % H_2O) were investigated to reveal the oxidation behaviour of sintered chromium at this temperature. During isothermal exposure, Cr pellets sintered with PVA binder showed almost identical behaviours to binder free pellets. The mass gain kinetics of the Cr pellets oxidised in dry air showed a parabolic behaviour, followed by a plateau after 150 hours that translated to the finalisation of the oxide growth. The mass gain kinetics of the Cr pellets oxidised in wet air were shown to be lower than those in dry air, due to Cr evaporation induced by the presence of humidity, resulting in a linear-like mass gain curve after 150 hours of exposure. While Cr was reported to also evaporate in dry atmospheres above 900℃ [147], no chromium was found to volatilise at 700℃ in dry air, in the present study.

Quantitative analyses highlighted the influence of mass loss, due to Cr evaporation, based on gravimetric data; these differences between corrected and uncorrected mass gains should not be disregarded. The rate constants (k_p and k_v), in both dry and wet atmospheres, revealed that not only the duration of the exposure test but also the method used (in comparison to methods reported in literature), had an effect on the rate constant values.

In the second part of the chapter, the commercial interconnect materials Crofer 22H and K41, were exposed at 700℃ to a typical SOFC cathode side environment (synthetic air with 3 % H_2O). Though a clear layering was not detectable, both investigated steels appeared to form an oxide scale (Fe, Mn Cr)$_3O_4$ while Si-rich zones were observed on K41 steel. The latter

demonstrated faster oxidation kinetics than Crofer 22H through higher measured mass gain and slightly faster Cr volatilisation. In agreement with the inferences of Sachitanand *et al*. [66], it was observed that a lower Mn content in the steel (here, K41) led to a faster Cr evaporation rate, and a higher Si content resulted in the apparition of silicon oxide-rich zones, as well as higher mass gains, as per the gravimetric measurements. Overall, in the present study, at 700°C, the Cr evaporation in both steels was lower than found in prior works using higher temperatures, indicating the benefit of SOFC operating temperature reduction.

Chapter 6 A Coupled Thermodynamic-Kinetic Model for the Oxidation of Binary Chromium-Rich Alloys.

“ Mais comment en sommes nous arrivés la ?“

This chapter aims to develop a one-dimensional (1D) numerical model to describe the oxidation of chromium (Cr) species within ferritic stainless steel used for solid oxide fuel cell (SOFC) interconnects and predicts their service lifetime under cathode operating conditions. This chapter presents the mathematical model developed for uncoated ferritic stainless steels (FSSs) using thermodynamic and kinetic approaches, modelling the diffusion oxidation of Cr during SOFC operating conditions. The model is applied to chromium concentrations results for Crofer 22H and K41 alloys presented in chapter 5.

6.1 Introduction

The continuous growth and maintenance of the chromium (Cr) protective oxide layer grown on ferritic stainless steels (FSSs) were dependent on the continuous supply of Cr, resulting from its diffusion through the bulk steel and oxide layer to the alloy surface. The maintenance of this layer, which protects the steel against further oxidation, depletes the alloy of Cr and other reactive elements. The purpose of this chapter is to develop a 1D numerical model to study the oxidation of Cr within the Fe-Cr-O system supporting FSSs used for SOFC interconnects and to predict its service lifetime under typical operating conditions.

First, in this chapter, thermodynamic modelling will be used to assess the oxidation behaviour of the Fe-Cr-O system at 700°C. The implications for the two types of ferritic steel, Crofer 22H and K41, which were experimentally investigated in Chapter 5, are discussed. The calculation is based on the coupling of phase diagrams and thermochemistry (calculation of phase diagrams or CALPHAD approach, see Chapter 2) and is presented as isothermal-section and oxide-stability diagrams. Second, a finite-difference computer code is written and used to model the 1D diffusion and oxidation process of a binary alloy-oxygen system (Fe-Cr-O) subject to isothermal oxidation under defined SOFC conditions (air atmosphere and 700°C operating temperature). The calculation is based on coupling diffusion transport of Cr through the substrate and oxide with the rate of oxidation and volatilisation reactions by applying the finite-difference method (FDM). The developed model can predict the mass gain upon exposure and, subsequently, the oxide film thickness, the concentration profile of the Cr over time, and the useable lifetime of the system under selected operating conditions. The parameter determination from the oxidation and volatilisation experiments is discussed along with the physical and design insights from the model. The model output predicts the composition of the oxide scale and concentration depth profile of elements after various oxidation exposure times by assuming parabolic oxide growth kinetics. Next, the

thermodynamic modelling of the Fe-Cr-O system at 700°C is presented in Section 6.2. Section 6.3 describes the mathematical development of the kinetic model. Finally, Section 6.4 presents the lifetime model predictions for the Fe-Cr-O system.

6.2 Thermodynamic Modelling of the Fe-Cr-O System at 700°C

6.2.1 Approach

A predictive thermodynamic assessment of the ternary system Fe-Cr-O was conducted using the thermodynamic calculation software Thermo-Calc, which uses the CALPHAD approach described in Chapter 2. The TCFE7 self-consistent elemental database embedded in the software was found to be the most suitable, since the success of the simulation greatly depended on the accuracy of the database used. This database was used to retrieve the thermodynamic data of the system and compute its thermal phase equilibria at 700°C, as shown in the diagram below.

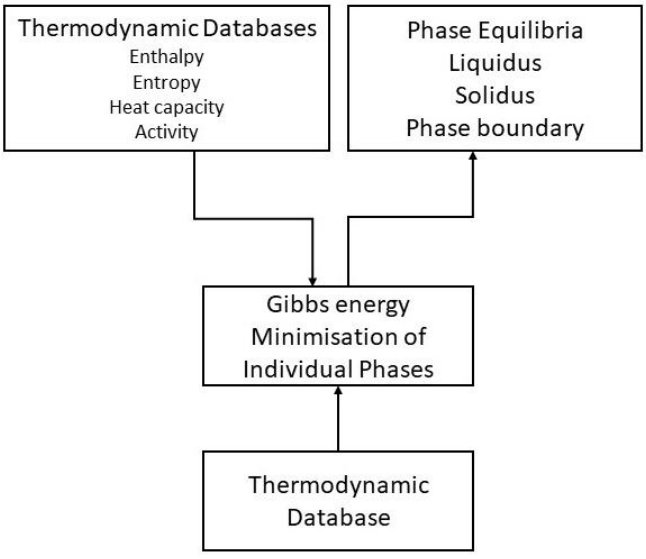

Figure 6-1 General working principle of the Thermo-Calc software (ThermoCalC course training manual).

Upon user input of chemical elements, the software starts by analysing its databank to reveal the phases and phase constituents of the system at the defined temperature, pressure, and system composition [122] and calculates the local equilibrium, that is, the point at which the system is the most stable, such that the Gibbs energy change of the reaction is null ($\Delta G = 0$). This operation is known as Gibbs energy minimisation. The solid phases are modelled through a model for composition dependence of Gibbs energy known as the compound energy formalism [155,186]. Phase diagrams of the Fe-Cr-O system, in the form of isothermal-section and chemical-potential diagrams, are computed to predict the different oxides prone to formation at 700°C and to assess their comparative stability.

6.2.3 Isothermal Section of Fe-Cr-O at 700°C and 800°C

Figure 6-2 illustrates the isothermal section of the Fe-Cr-O system at 700°C, which was modelled using the TCFE7 database in the Thermo-Calc (see Chapter 2 for details). The calculations were based on the mass fraction. The results were compared to the Fe-Cr-O phase diagram at 600°C presented by Pujilaksono *et al.* [175] using Thermo-Calc software and at 800°C reported by Dheeradhada *et.al* [114] using the Pandat software. In the present work [114], the phase diagrams revealed stable oxide phases at 700°C and at 800°C, namely [$(Fe,Cr)_2O_3$], the spinel $(Fe,Cr)_3O_4$), and halite (FeO) (Figure 6-3). The strong presence of iron (Fe) agreed with the Fe-rich oxides observed during the oxidation studies of the ferritic steel types Crofer 22H and K41 in Chapter 5, and a clear-cut, single Cr_2O_3 phase was not apparent at 700°C. This was accentuated by the co-existence of the halite phase (FeO) with spinel at 700°C, whereas it was shown to exist as a single-phase field at 800°C [114]. As the temperature was reduced from 800°C to 700°C, the oxygen (O_2)-rich portion in the [$(Fe,Cr)_2O_3$] phase extends further than in the phase diagram at 800°C with a constant concentration at 30% (or 0.3 mass fraction) compared to 60% (or 0.6 mass fraction) at 800°C, pointing to a lower O_2 solubility at 700°C. Interestingly, the two solid-solution phases (body

centre cubic (BCC (Fe, Cr)) + Cr_2O_3) appeared to shrink by 50% from 800°C to 700°C. This points to the effect of the reduction of the operating temperature, at which the BCC phase is stable and in equilibrium with Cr_2O_3 for ferritic steel containing up to approximately 28% Cr (or 0.28 mass fraction) at 700°C compared to almost 40% (or 0.4 mass fraction) of Cr at 800 °C.

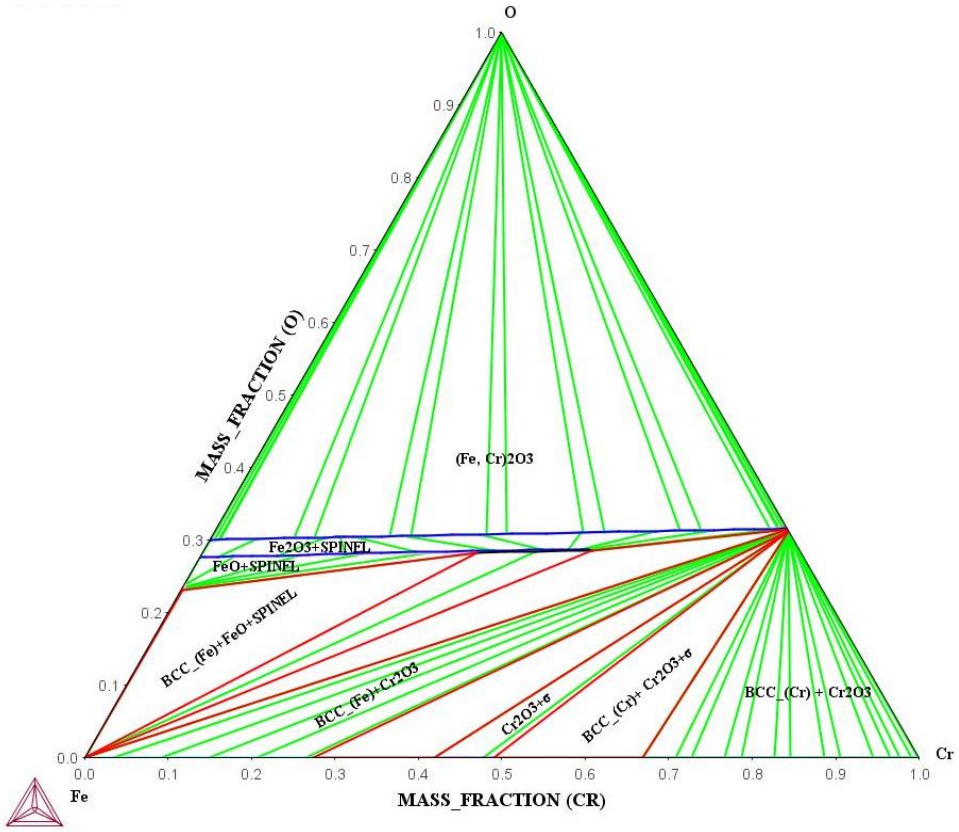

Figure 6-2 Calculated phase diagram of Fe-Cr-O at 700°C.

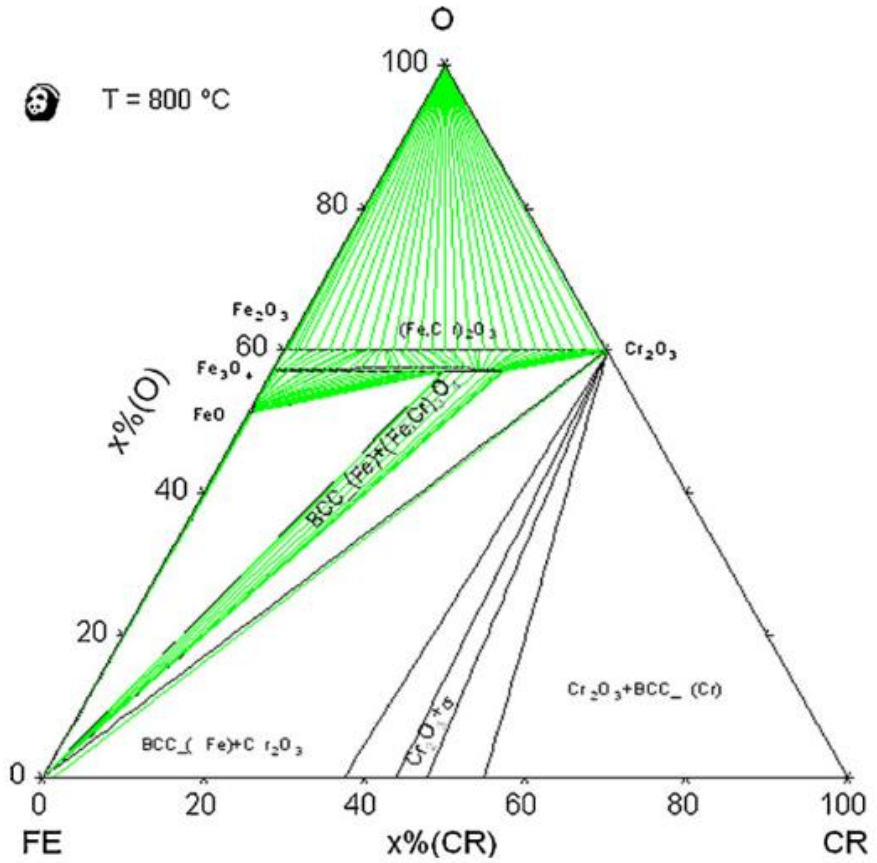

Figure 6-3 *Dheeradhada et.al* [114] calculated the isothermal section of Fe-Cr-O at 800°C.

6.2.4 Stability Diagram of the Fe-Cr-O System at 700°C

The interconnect component is exposed to the oxidising side of the SOFC, which carries a much higher oxygen partial pressure (pO_2; 0.21 atm) compared to the reducing (fuel) side (10^{-18} to 10^{-8} atm). This suggests the alloy composition and pO_2 are two controllable variables, which greatly influence the scale formation, but more importantly, its composition. The influence of temperature and pO_2 on the phase formation and phase stability in Fe-Cr-O was modelled using ThermoCalC and is presented in the following paragraph.

Figure 6-4 depicts the calculated stability diagram of the Fe-Cr-O system at 700°C, which presents the amount and composition of the phases as a function of pO_2. Similar to the

research findings at 800°C [114], the corundum phase, either as spinel ($(Fe,Cr)_3O_4$) or $(Fe,Cr)_2O_3$), is the most stable phase at a pO_2 higher than 10^{-8} atm. This correlates with the microstructural changes (spinel) observed on the surface of the oxidised ferritic steel types of Crofer 22H and K41 in air, as discussed in Chapter 5. At a lower pO_2 ($pO_2 < 10^{-25}$ atm), the BCC (Fe or Cr depending on the dominant concentration) and sigma phases are in equilibrium with the corundum phase $(Cr,Fe)_2O_3$, which would be either richer in Cr or Fe. For pO_2 Between 10^{-25} and 10^{-8} atm, the Fe-Cr-O system appears to evolve in four different phases: halite (FeO), spinel ($(Fe,Cr)_3O_4$), BCC (Fe or Cr), and corundum $(Fe,Cr)_2O_3$. At 800°C in this pO_2 range [114], the corundum phase was found to exist as a pure Cr_2O_3 rather than $(Cr,Fe)_2O_3$, illustrating the consequence of reducing the operating temperature.

The dotted lines in Figure 6-4 correspond to the composition range studied in this work and enable us to predict the sequence of oxides expected to form upon oxidation of ferritic steel at 700°C, as presented in Figure 6-5. For ferritic steels containing between 17% and 24% Cr, the predictive sequence indicates that, at the interface of the oxide and air, where the PO_2 is the highest, spinel, here of type ($(Fe,Cr)_3O_4$) is the dominant compound. Inversely, at the oxide/metal interface (low PO_2), $(Fe,Cr)_2O_3$ is expected to form in place of Cr_2O_3 at 800°C [114], and several oxides are anticipated to form in between, as previously described. Interestingly, these results also show that for $pO_2 > 10^{-18}$atm, the spinel phase is exclusively predicted to exist, and increasing the pO_2 would be inconsequential. During the SCORED 2.0 project, experiments carried by research partner, where PO_2 was increased above 10^{-18}atm correlated with these findings.

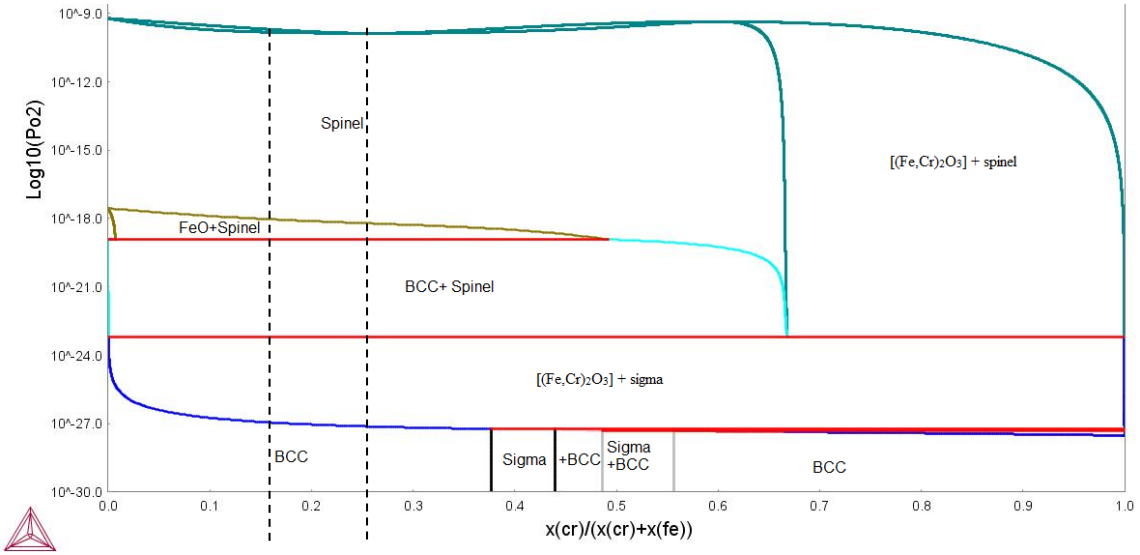

Figure 6-4 Calculated stability diagram for Fe-Cr-O at 700°C.

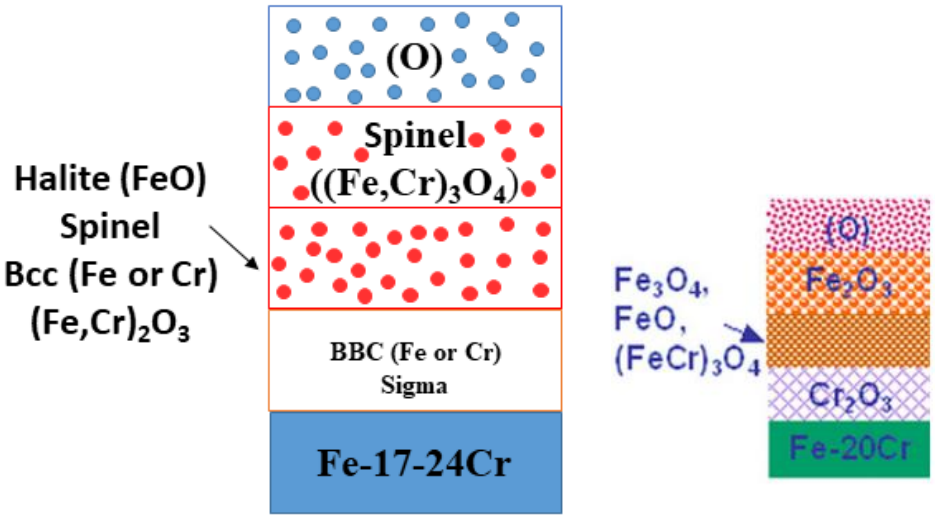

Figure 6-5 Sequence of oxide formation for the Fe-Cr-O system calculated in the present work at 700°C (left) and reported in [114] at 800°C (right).

6.3 One-dimensional Kinetic Model Development

6.3.1 System Description and Formulation

The physical system considered in the following consists of elemental Cr contained in (unless otherwise stated) a non-reactive ferritic (Fe) stainless steel matrix. As discussed in Chapter 2, through a comparison of diffusion coefficients reported in the literature, at high temperatures, Cr diffuses outward through the steel, depleting the latter (leading to an external oxidation of the system). Although this occurs concurrently with the inward diffusion of oxygen (leading to an internal oxidation of the system), the diffusion of Cr is known to be faster than that of oxygen [90]. Although including internal oxidation would lead to a fuller (as oxygen also has a solubility in Fe), more complete model, the much slower diffusion of oxygen in the Cr layer allows the assumption of no internal oxidation, which simplifies the model without much repercussion. As such, only external oxidation (i.e. appearing on the outside surface of the steel) and, thus, solely the diffusion of Cr, is considered in this work, it also assumes that no initial oxide exists, that is, initially, the rate of growth of the oxide is so low that it may initially be set to zero.

Thus, if the oxidation process is dominated by the outward diffusion of the Cr species and no initial oxide film exists, the transported species must undergo the following stages in the system illustrated in Figure 6-6, where *C* denotes the respective concentration of the reacting elements:

(1) Chromium ions are transported by a diffusion mechanism from the system reservoir to the vicinity of the alloy surface.

(2) Chromium ions react with the oxidant, and oxide nuclei are formed.

(3) The oxidation process proceeds through the continuous solid-state diffusion of Cr ions through the steel and the oxide scale, with a subsequent reaction on the alloy surface.

(4) In the presence of water vapour, the growth of the oxide scale simultaneously competes with the formation of volatile Cr species, through the humid oxidation of chromia at the interface oxide/gas

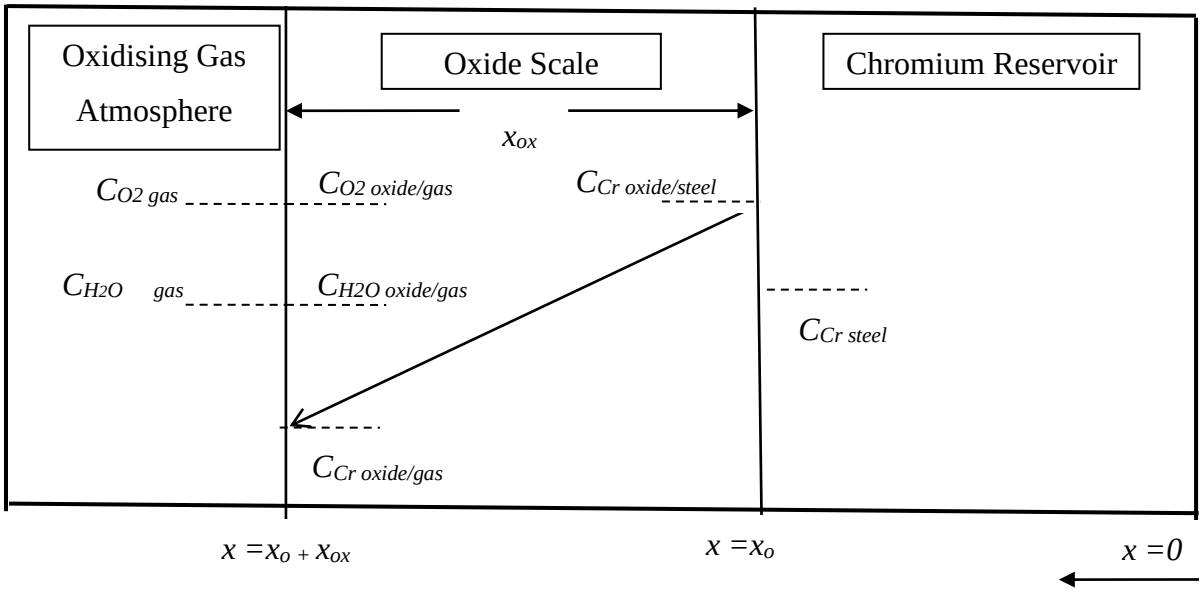

Figure 6-6 Schematic description of the considered system (not to scale).

6.3.2 Modelling Work Challenges

Some challenges were encountered concerning creating a true oxidation diffusion model of an interconnect alloy. Unlike gases and some liquids, no currently developed theory predicts diffusion coefficients in dense solids. Diffusion coefficients are almost exclusively obtained by tracer diffusion experiments, often with discrepancies as discussed in Chapter 2, and no recent experimental data have been reported. In addition, most diffusion coefficients available in the literature for Cr were determined from polycrystals at a temperature range exceeding that of the present experiment, [90,97,98] making them unsuitable for this modelling work.

6.3.3 Solid-state Diffusion of Chromium in the Steel Matrix

Chromium diffuses through two different solid-state media: the steel matrix and the oxide scale. The steel reservoir has a finite concentration of Cr, and as its surface oxidises during the operation of the fuel cell, a depletion of chromium from the steel matrix occurs over time. This varying time-dependent Cr concentration translates into a transient solid-state isothermal Cr diffusion through the alloy. Fick's second law, expressed in Eq. (6-3) for this case, is used to calculate the rate of change of the Cr concentration in the steel matrix based on the local concentration gradient:

$$\frac{\partial C_{Cr_{steel}}}{\partial t} = \frac{\partial}{\partial x}\left(D_{Cr_{steel}} \frac{\partial C_{Cr_{steel}}}{\partial x}\right), \qquad \text{Equation 6-1}$$

where $\partial C_{Cr\ steel}/\partial t$ is the rate of change of Cr concentration per unit of time t, $D_{Cr\ \text{steel}}$ is the diffusion coefficient of Cr in the steel, and $\partial C_{Cr\ steel}/\partial x$ is the concentration gradient of Cr in the steel.

The complexity of this partial differential equation means that it can hardly be solved analytically. However, through numerical methods, it is possible to monitor the depletion of Cr in the steel matrix. The finite difference (FD) method was used here, which allows such differential equations to be solved computationally. In the FD approach, time (t) and space (x) are divided into grids of discrete points i and j (where i is a point in space and j is a point in time), such that they can be expressed by approximations known as difference equations (Figure 6-7). This process is known as discretisation and is a requisite for computational calculations.

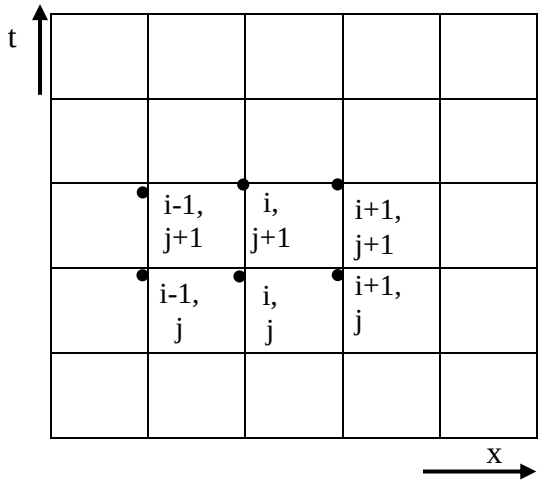

Figure 6-7 Finite-difference approximation grid.

In addition, an implicit scheme was employed, which is superior to an explicit scheme because it eliminates numerical instability and consequential numerical errors. In the explicit formulation, *j*+1 can be solved explicitly for each spatial position; however, this is associated with greater numerical instability because the time step is limited to a maximum (Eq. 6-4), which fatally results in greater errors. In the implicit formulation, no explicit formula exists for each point; instead, a set of simultaneous equations exists to be solved over the entire region of interest. Implicit methods, as opposed to explicit schemes, allow the use of a larger time step with less computational time without suffering from instability resulting from the numerical errors in explicit methods:

$$\Delta t \leq \frac{(\Delta x)^2}{2D} \qquad \text{Equation 6-2}$$

Thus, the discretised bulk concentration of Cr ions is expressed in terms of the concentration of the neighbouring grid points as follows:

$$C_i^n = C_{i-1}^{n+1} - (D_i^n \gamma C_{i+1}^{n+1} - 2C_i^{n+1} + C_{i-1}^{n+1})C + \left(\frac{1}{4\gamma(C_{i+1}^{n+1} - C_{i-1}^{n+1})(D_{i+1}^n - D_{i-1}^n)}\right) \qquad \text{Equation 6-3}$$

where *i* describes the current grid point in space, *n* denotes the current iteration in time, *C* is the concentration of Cr ions, *D* describes the concentration-dependent Cr diffusion coefficient, and γ represents $\Delta t/\Delta x^2$, where x is the thickness of substrate.

This leads to a system of linear equations that must be represented as a matrix of the following form to be computed:

$$C_i^n = AC_i^{n+1} \qquad \text{Equation 6-4}$$

where A is the coefficient of the matrix, C^{n+1} denotes the variable vector, and C^n represents the resultant constant vector. Thus, we obtain the following matrix of coefficients:

$$\begin{pmatrix} \vdots \\ C_2^n \\ \vdots \end{pmatrix}$$

$$= \begin{pmatrix} \cdots & 0 & -D_i^n\gamma + \frac{D_{i+1}^n\gamma}{4} \frac{D_{i-1}^n\gamma}{4} & 1 + 2D_i^n\gamma & -D_i^n\gamma - \frac{D_{i+1}^n\gamma}{4} + \frac{D_{i-1}^{n+1}\gamma}{4} & 0 & \cdots \end{pmatrix} \begin{pmatrix} \vdots \\ C_2^{n+1} \\ \vdots \end{pmatrix}$$

Equation 6-5

6.3.4 Initial and Boundary Conditions

At the start (i.e. at $t = 0$ for all $x = L$, i.e the thickness of the substrate), the initial concentration of Cr within the bulk of the alloy is $C_{Cr} = C^0_{Cr}$. During the high-temperature oxidation of the interconnects, only the surface that contacts the oxidising air from the cathode is of interest. Consequently, a zero-flux wall boundary condition is applied across the length (*L*) of the bottom part of the substrate, expressed as follows:

$$\left(\frac{\partial C_{Cr_{steel}}}{\partial x}\right)_{x=L} = 0 \qquad \text{Equation 6-6}$$

Once the above equation is discretised, we obtain Equation 6-9, and Equation 6-10 describes the resultant matrix operation.

$$C_i^n = C_i^{n+1} - 2\frac{D\Delta t}{\Delta x^2}(C_{i+1}^{n+1} - C_i^{n+1}) \qquad \text{Equation 6-7}$$

$$C_m^{n+1} = (0 \quad 1 + 2D\gamma \quad -2D\gamma) = (C_m^n) \qquad \text{Equation 6-8}$$

At the steel–oxide interface, the boundary condition is governed by the flux of Cr ions diffusing from the bulk to the growing oxide. Cr flux through the oxide is necessary to support the protective oxide's growth and maintain its homogeneity. This flux is assumed to be constant, implying a steady-state diffusion of Cr through the oxide. Fick's first law (Eq. 6-11) is used as a boundary condition for the flux of Cr crossing the steel–oxide interface.

$$J_{Cr\,ox} = D_{Cr\,ox}\left(\frac{C_{Cr\,ox/steel} - C_{Cr\,ox/gas}}{x_{ox}}\right) \qquad \text{Equation 6-9}$$

where $J_{\text{Cr ox}}$ is the rate of change of Cr concentration per unit of time t, $D_{Cr\ \text{steel}}$ is the local diffusion coefficient of Cr in the oxide, $C_{Cr\ ox/steel}$ is the concentration of Cr near the oxide–steel interface, $C_{Cr\ oxide/gas}$ is the concentration of Cr near the oxide–gas interface and x_{ox} is the space coordinate measured normal to the considered section (i.e. the thickness of the oxide). Several parameters, including temperature and reactant flow, affect the diffusion of Cr in the oxide. At the oxidation front (the air–oxide interface), the boundary conditions are governed by the prevailing oxidation kinetics, which are described in Section 6.3.5.

The effective diffusion coefficient D_{eff} encompasses both lattice and grain boundary diffusion, as described in [187]:

$$D_{eff} = D_L(1 + f) + D_{gb} \qquad \text{Equation 6-10}$$

where D_L and D_{gb} are, respectively, the lattice and grain boundary diffusion coefficients and f is the fraction associated with the grain boundary, generally taken as 0.0005 for chromia scales [187]. The diffusivity being greatly dependent on the temperature, the Arrhenius relation [188] was used to extrapolate the effective diffusion coefficient at 700°C:

$$D = D_o exp\left(\frac{-Ea}{RT}\right) \qquad \text{Equation 6-11}$$

where D_o is a pre-exponential factor that depends on the diffusion type, E_a is the activation energy, *T* is the temperature in K and *R* is the gas constant.

To estimate the sensible value for the present work, we used D_{eff} values from [90,97,98] to construct an Arrhenius relation and estimate the activation energy, which was used to estimate D_{eff}. Since we assumed steady-state diffusion in the oxide, a single diffusion coefficient was used in all the oxide calculations (Table 6-1). However, due to the transient-state of the bulk, a loop system in the Cr depletion calculation enabled the output of D_{eff} for every numerical iteration. The initial values used for the calculation achieved numerical convergence (Table 6-1).

Table 6-1. Model Input Parameters

Fe17Cr	
Pressure	1 atm
Temperature	700˚C
Flow rate	1 litre / minute
Water vapour concentration	3%
Substrate thickness	0.2 cm
Diffusion coefficient in bulk	8E-15 $cm^2.s^{-1}$
Diffusion coefficient in oxide	2E-13 $cm^2.s^{-1}$
Chromium oxidation rate constant	4.60E-10 $g^2cm^{-4}\ s^{-1}$
Chromia oxidation rate constant	8.95E-10 $gcm^{-2}\ s^{-1}$

Fe22Cr	
Pressure	1 atm
Temperature	700°C
Flow rate	1 litre / minute
Substrate thickness	0.2 cm
Initial diffusion coefficient in bulk	8E-15 $cm^2.s^{-1}$
Initial diffusion coefficient in bulk	2E-13 $cm^2.s^{-1}$
Chromium oxidation rate constant	3.61E-10 $g^2cm^{-4}\ s^{-1}$
Chromia oxidation rate constant	3.93E-13 $gcm^{-2}\ s^{-1}$

6.3.5 External Oxidation Reaction Kinetics

As explained in Section 6.3.1, the model proposed describes a binary alloy (FeCr) with preferential oxidation at the oxide–gas interface. To model the kinetics, the following assumptions were made:

a) The steady-state has been reached;

b) Oxygen in excess is adsorbed on the surface of the oxide film;

c) Cr is transported across the oxide film (Cr_2O_3) to the vicinity of the alloy surface;

d) Oxygen and Cr react at the oxide–air interface to form a new layer; and

e) Cr_2O_3 is the only oxide formed (for simplicity, as experimentally Fe is always present)

Two oxidation reactions occurred continuously throughout an SOFC operating at 700°C. The first reaction was the oxidation of Cr, resulting in the formation of chromium oxide (Cr_2O_3) expressed as:

$$2\ Cr_{(s)} + \frac{3}{2} O_{2\ (g)} \longrightarrow Cr_2O_{3\ (s)}, \qquad \text{Equation 6-12}$$

for which the reaction rate is expressed as:

$$J_{R1} = 2k_{r1} {C_{cr}}^{s} {C_{o_2}}^{t} \qquad \text{Equation 6-13}$$

where C_{Cr} is the concentration of the reacting Cr, C_{O2} is the concentration of oxygen, k_{r1} is the reaction constant derived experimentally from Chapter 5 and *s* and *t* are the orders of reaction for Cr and O_2, respectively. By combining the excess oxygen assumption with first-order reaction kinetics, Equation 6-15 can be simplified and written in terms of Cr alone:

$$\mathrm{J_{R1}} = 2\mathrm{k_{r1}} C_{Cr} \qquad \text{Equation 6-14}$$

The second reaction involves the oxidation of chromium oxide (Cr_2O_3), leading to the formation of volatile and cathode-poisonous Cr gas ($CrO_2(OH_2)$):

$$Cr_2O_{3\ (s)} + \frac{3}{2} O_{2\ (g)} + 2H_2O_{(l)} \longrightarrow 2CrO_2\ (OH)_{2\ (g)} \qquad \text{Equation 6-15}$$

The reaction rate expression for Eq. 6-17 is the following:

$$\mathrm{J_{R2}} = 2k_{r1} C_{Cr_2O_3} C_{H_2O} \qquad \text{Equation 6-16}$$

Equation 6-18 combines oxygen excess and first-order reaction kinetics, where C_{H2O} is the concentration of the reacting water vapour at the air–oxide interface.

When exposed to air humidity, the SOFC runs under wet air operating conditions. The flux of water vapour from the gaseous phase to the vicinity of the alloy surface can be expressed as follows:

$$J_{H_2O} = 2h(C_{H_2O_{gas}} - C_{H_2O_{ox}}), \qquad \text{Equation 6-17}$$

where $C_{H2O\ gas}$ is the concentration of water vapour on the oxidant side, $C_{H2O\ ox}$ is the concentration of water vapour on the oxide–gas interface and *h* is a constant.

Although the diffusion in steel was described as transient in Section 3.1.2, the numerical time-steps that brought the model to convergence were much shorter than the duration of the reaction. Furthermore, having assumed that the rest of the system was at steady-state, it was reasonable to assume a general steady-state of the system to equalise the different fluxes:

$$J_{Cr\ ox} = J_{R1}\ and\ J_{H_2O} = J_{R2} \qquad \text{Equation 6-18}$$

Finally, the overall reaction flux, *J*, involving the formation and removal of chromium oxide, is given by rearranging Eqs. 6-11, 6-16, 6-18 and 6-19 into Eq. 6-21, also expressed as Equation 6-22:

$$J = J_{R1} - J_{R2} \qquad \text{Equation 6-19}$$

$$J = \frac{C_{Cr\ steel}}{1+\frac{2k_1 x_{ox}}{D_{Cr_{ox}}}} - \frac{C_{H2O}}{\frac{1}{h}+\frac{1}{2k_2}} \qquad \text{Equation 6-20}$$

6.4 Application to FeCr Alloys

6.4.1 Parameters

The finite-difference model described above was applied to the oxidation of two single-phase binary alloys: Fe-17Cr (at %) and Fe-22Cr (at %) alloys isothermally oxidised at 700°C (973 K) in ambient partial pressure in oxygen. These Cr concentrations were selected to approximate the Cr concentrations in the K41 and Crofer 22H alloys oxidised in Chapter 5, respectively, and the reaction rates calculated in that chapter were used. Diffusion coefficients were approximated from Tsai [187], who determined effective diffusion coefficients in Cr_2O_3 and in Cr_2O_3 scales on an Ni-30Cr alloy at 900 °C. The same initial

diffusion coefficients were used for two reasons: to compare the systems based only on concentration and reaction rate changes, and to account for the lack of diffusivity reported in Section 6.3.2. The parameters used are summarised in Table 6-1 unless otherwise stated. The model produced values of oxide growth changes and humidity and Cr depletion profiles over time.

6.4.2 Oxide Growth at 700 °C in Air + 3% H_2O

In his model of the oxidation of a Ni-Al-Cr alloy, Wu [189] assumed the initial presence of various oxide layers, which allowed him to avoid describing the initial oxide growth stage. In the present model, this was made possible by assuming that no initial oxide was formed, mirroring the grinding and polishing steps conducted experimentally. By coupling the binary diffusion equation with the reaction kinetics, the overall thickness of the film developed as a function of oxidation time can be modelled, encompassing all the individual oxide phases predicted in Section 6.1.3. Most oxide growth models available in the literature are based on the parabolic growth assumption, but chromia (as shown in the experimental work reported in Chapter 5) is known to deviate from this ideal behaviour. The present model thus accounts for the simultaneous oxidation and vaporisation of the protective oxide.

Figs. 6-8 and 6-9 plot the oxide growth predicted after 1,000 hours and 5,000 hours in air with 3% humidity for Fe17Cr and Fe22Cr alloys. Figs. 6-11 and 6-12 compare the oxide growth with different levels of humidity in the system over 50,000 operation hours. As can be observed in Figure 6-8, initially, (in line with experimental observations for K41) the oxide growth is fast compared to evaporation, resulting in paralinear behaviour over 1,000 hours of exposure.

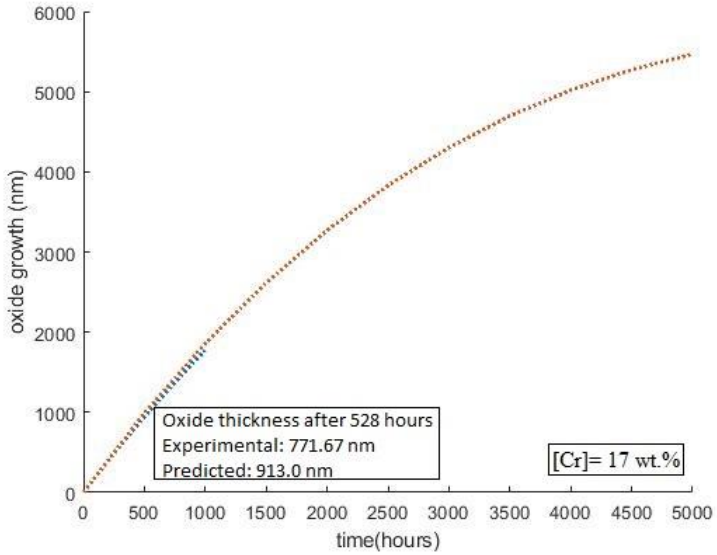

Figure 6-8. Predicted oxide growth profiles of Fe17Cr (wt.%) steel over 5,000 hours in air + 3% H_2O at 700 °C.

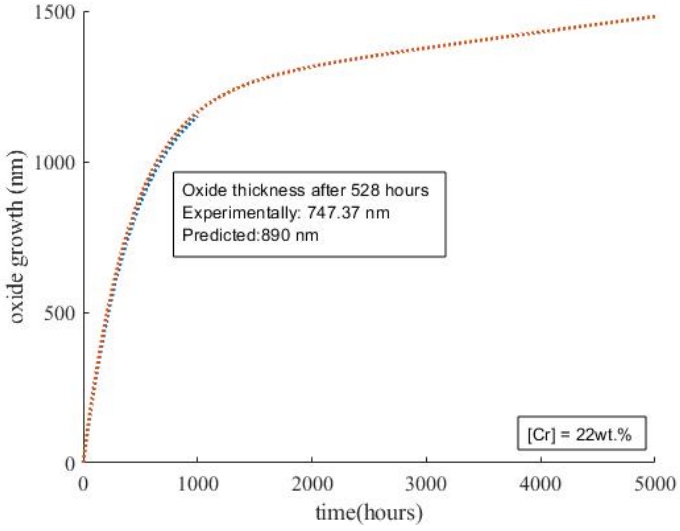

Figure 6-9. Predicted oxide growth profiles of Fe22Cr (wt. %) steel over 5,000 hours in air +3 % H_2O at 700 °C.

After this point, the evaporation reaction dominates, resulting in a continuous loss of protective oxide. In the absence of humidity, however, the oxide grows to a maximum and near plateaus. This behaviour was also experimentally observed on pure Cr pellets in (5.2.2),

translating the saturation of the pellets with chromium oxide and leading to a constant scale thickness. This is more visible in Figure 6-10 which was extrapolated to 50,000 hours of operation.

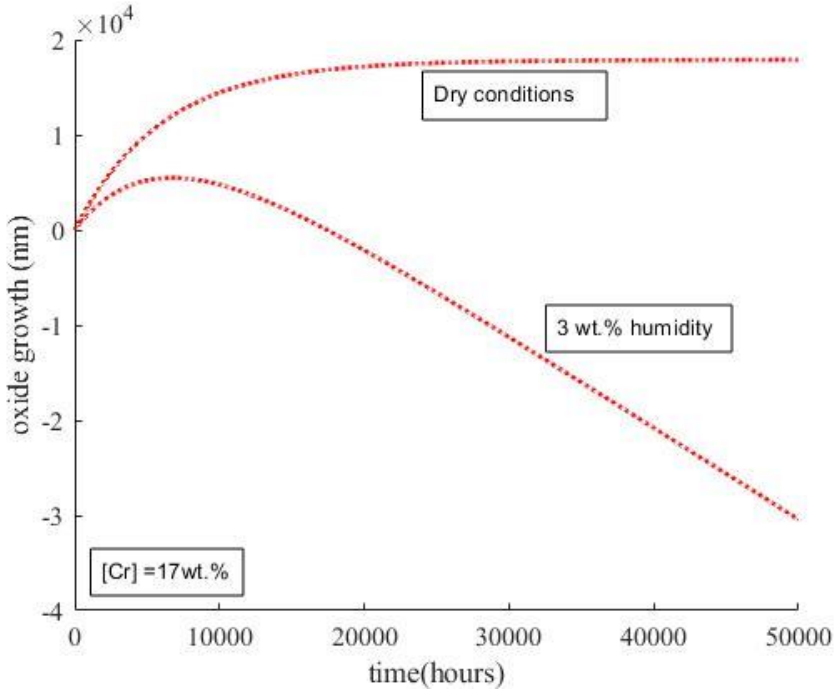

Figure 6-10. Predicted oxide growth profiles of Fe17Cr (wt%) steel over 50,000 hours in dry air and air+3% H_2O at 700 °C.

6.4.3 Effect of Water Vapour on Oxide Growth

Fig. 6-11 and Fig. 6-12 illustrate the effect of increased water vapour on oxide growth at 700 °C in air for 17 wt% Cr and 22 wt% Cr binary alloys over a simulated period of 5,000 operational hours at 700 °C. It can be seen that for a lower Cr concentration of 17 wt% (Fig. 6-11), an increase from 3% to 5% humidity still presents the simultaneous oxidation and volatilisation characteristics of the paralinear behaviour of K41 steel in these conditions (Chapter 5), extrapolated to 50,000 hours in Figure 6-10. This is driven by the relation between the rate of oxide supply and its consumption, the latter being more pronounced in an

atmosphere of 5% H_2O air. However, an increase to 10% water vapour clearly influences oxidation behaviour, as it results in a completely negative oxide growth profile (Fig. 6-11). This could mean that at this humidity level, any oxide formed is directly consumed in the formation of volatile Cr gases. However, as the oxide never appears to grow, it may also indicate a degradation of the base metal including spallation or rust-like behaviour. For the binary Fe22Cr alloy (Fig. 6-12), the effects of increased water vapour from 3% to 5% humidity are slightly reduced, as the volatilisation is slower to occur. This is also visible at 10 wt% humidity, where after 5,000 hours of simulated operation, an oxide thickness is still present, though decreasing. Thus, at similar humidity conditions, oxides grown on alloys with higher Cr content would suffer the effects of Cr vaporisation at a slower rate than those grown on alloys with lower Cr content. This is beneficial for interconnect components made from ferritic stainless steels.

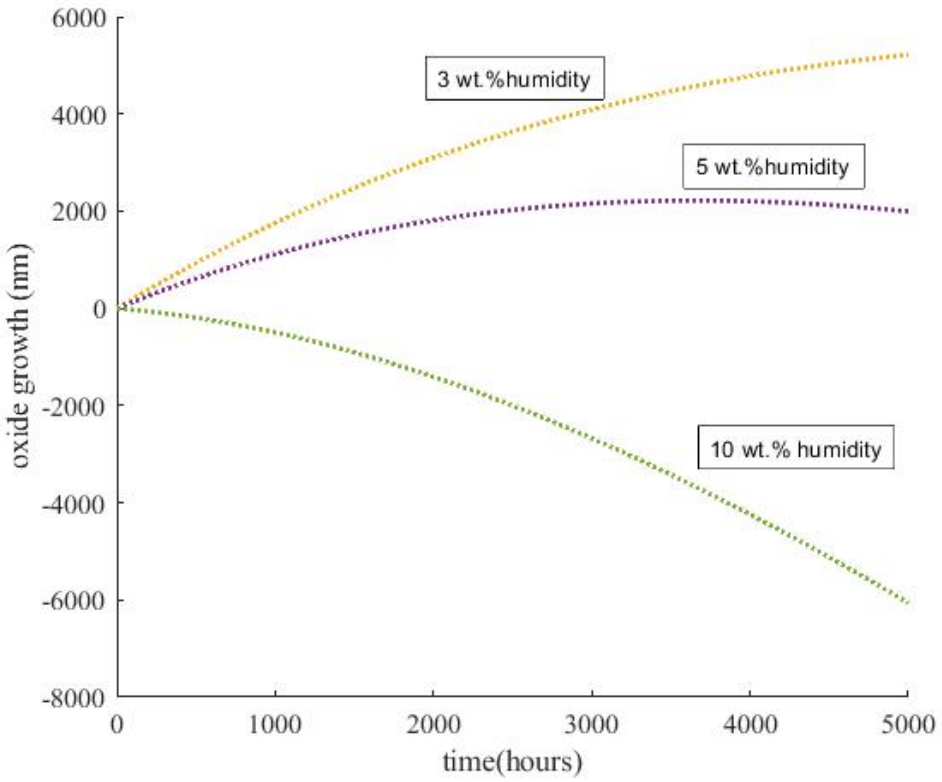

Figure 6-11. Predicted oxide growth profiles of Fe17Cr (wt. %) steel over 5,000 hours in Air+3% H_2O at 700 °C at different humidity levels.

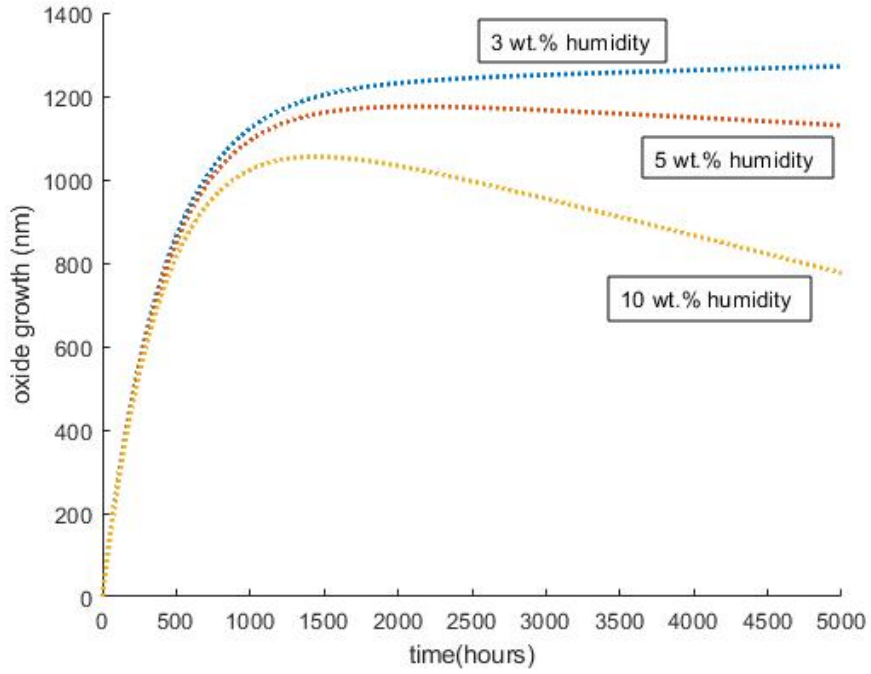

Figure 6-12. Predicted oxide growth profiles of Fe22Cr (wt%) steel over 5,000 hours in Air+3% H_2O at 700 °C at different humidity levels.

6.4.4 Chromium Depletion and System Lifetime

To be considered stainless steels, ferritic stainless steels are required to contain a minimum Cr concentration of 11% [40]. Iron-based alloys used for SOFC interconnects generally range between 17–25 wt% of Cr content, which is depleted during the operational life of the SOFC. It follows that below a critical Cr content, the Cr supply to the continuous growth or rehealing of the protective oxide would end, and less protective oxides would appear. This point can be used to define the end of the useful life of the alloy. Here, a numerical computation to model Cr depletion in the Fe17Cr and Fe22Cr (wt%) systems we developed and thus predicts the substrates' lifespans. Fig. 6-14 shows the variation of the bulk Cr

concentration against time for the oxidation of the binary systems Fe17Cr and Fe22Cr (wt%) over 50,000 hours at 700 °C in air with 3% water vapour.

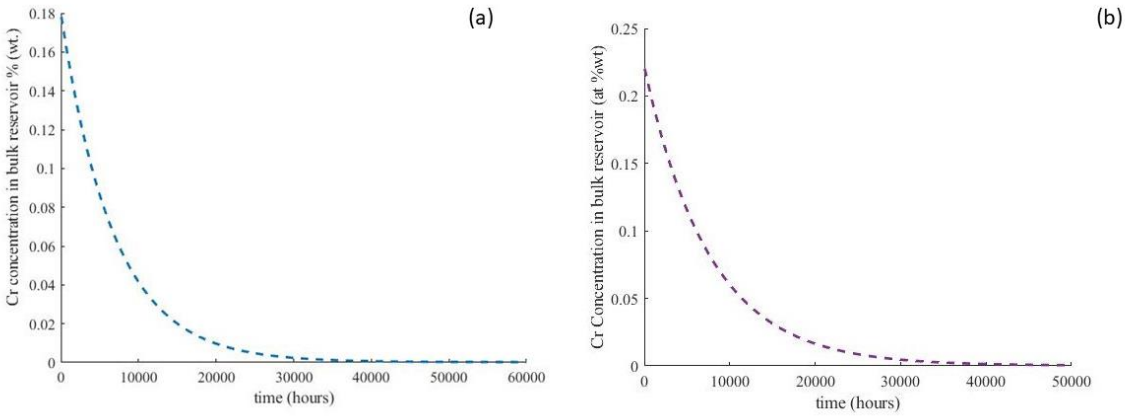

Figure 6-13. Simulated Cr depletion profile in the bulk reservoir of (a) Fe17Cr and (b) Fe22Cr.

For the Fe17Cr alloy, the model predicted that it would take 26,500 hours of oxidation time to reach a Cr concentration 11 wt%, whereas the same concentration would be attained after 53,500 hours for the Fe22Cr alloy, implying nearly twice the operational time in a cathodic SOFC atmosphere. Whilst the model is only binary, and, various other alloying elements would be needed to precise the exactitude of the lifetime of Crofer 22H and K41, these results are a clear indication of the trend these alloys would follow. Due to its higher chromium content, Crofer 22H would serve its purpose longer than K41 alloy in SOFC conditions.

6.5 Summary

The first part of this chapter examined the thermodynamic changes occurring in the Fe-Cr-O system at 700 °C using the CALPHAD approach. In contrast to data reported in the literature

for 800 °C, our prediction showed that at 700 °C, Cr_2O_3 does not exist as a single phase, instead co-existing in the form of spinel. Overall, however, the temperature reduction resulted in the following successive oxide phases: $(Fe,Cr)_2O_3$, spinel $(Fe,Cr)_3O_4$ and halite (FeO) (Figure 6-2). Modelling the phase stability diagram of the system enabled the sequential prediction of these phases. The diagram implied that the stability of these oxide phases is dependent on the oxygen partial pressure (PO_2), but only to an extent; at PO_2 values higher than 10^{-8} atm, only spinel ($(Fe,Cr)_3O_4$) exists in a stable form.

In the second part of the chapter, a one-dimensional (1D) kinetic model was developed using the finite-difference method to serve as a basis for predicting the lifespan of ferritic stainless-steel alloys used for SOFC interconnects. The model was applied to two binary systems (Fe17Cr and Fe22Cr, wt.%), encompassing the diffusion of Cr and subsequent oxidation in air. Given user input, the model can profile predicted oxide growth and Cr ions depletion as a function of time. Overall, whilst similar trends were observed between the measured oxide growth of K41 steel and Crofer 22H steels, some numerical discrepancies persisted. This was attributed to the idealistic nature of the model, the exclusion of important alloying elements such as manganese and experimental observations, including spallation. In order to increase its accuracy, the developed model should account for Manganese diffusion for instance, which was to form a spinel cap over Cr_2O_3, as reported in chapter 5. However, the model was in line with the experimental results in that higher Cr concentrations resulted in slower oxide growth, which ultimately extended the useful lifetimes of the alloys.

Chapter 7 Conclusions & Outlook

« ...Et toute chose a une fin »

7.1 Conclusions

Chromium, a key component of ferritic stainless steels used for SOFC interconnect applications, was investigated both experimentally and through numerical tools.

In the first part of this study, the isothermal oxidation kinetics of binder-free Cr sintered pellets were studied via exposure to synthetic dry air, (N_2-20% O_2) and synthetic wet air (N_2-20% O_2 with 3 % H_2O) atmospheres at 700°C, and the evaporation of chromium was measured using the denuder tube method. No volatile chromium was reported in dry conditions, and a parabolic mass gain behaviour was observed. In humidified oxidation, however, para-linear growth was observed, with lower mass gain kinetics compared to dry oxidation. The study showed that both the duration of the exposure and the chromium collection method had an impact on the estimation of the kinetics parameters, leading to different oxidation and evaporation rate constant values reported in literature.

Two commercial interconnect steels – Crofer 22H and K41 – were exposed at 700°C to a typical SOFC cathode side environment (synthetic air with 3 wt. % H_2O). Both investigated steels appeared to form a duplex scale consisting of a spinel ($(Fe,Cr,Mn)_3O_4$) and an oxide (Cr_2O_3). Over an experimental period of 1000 hours, less Cr was found to evaporate from these steels at 700°C as compared to reported Cr evaporation at higher temperatures, supporting their use for reduced SOFC operating temperature. However, the non-conductive Si-rich zones observed on K41 steel, together with a higher Cr evaporation rate and faster oxidation kinetics, should lead to a preference for Crofer 22H. The thermodynamic modelling of the Fe-Cr-O system at 700°C conducted in the last part of this study also indicated that

Cr_2O_3 does not exist singly and enabled layering of formed oxides with respect to oxygen partial pressure. In a cathodic atmosphere of a pO_2 higher than 10^{-8} atm, only the spinel ($(Fe,Cr)_3O_4$) was predicted by the model as the stable phase. A one-dimensional kinetic model of the diffusion and oxidation of chromium in the Fe-Cr-O system was also developed. A test case was set up for binary alloys Fe17Cr and Fe22Cr with wt. % using the reaction rates obtained experimentally for K41 and Crofer 22H steels. Whilst numerical discrepancies were present, a similar trend was observed between the measured and predicted oxide growth profiles. The developed model featured the prediction of useful lifetime of the systems by utilising predicted bulk concentration profiles. Again, the Fe22Cr system was predicted to supply oxide growth for almost twice the time as the Fe17Cr system.

7.2 Outlook

Although this study has provided some insights into the oxidation behaviour of chromium at a lower temperature in line with SOFC temperature reduction, as well as an initial step in predicting lifetime and oxide growth in a single-phase binary FeCr alloy, further work is needed to improve the accuracy of the uncoated alloy model in particular, and to pave the way for coating system modelling.

In practice, the air flow used in SOFCs is specific to the SOFC designed. In this study, 1000 ml/min of air flow was used for the oxidation of both chromium and chromium rich steel, as per the SCORED 2.0 project. In developing the denuder technique used in this study, Froitzheim [113] showed that at 850ºC, and below 5000 ml/min, the evaporation rate of Cr species in ferritic steels is dependent on air flow, which in turns affects the results in terms of oxide growth; thus it would be interesting to conduct a similar study at the reduced operating temperature of 700ºC and determine the independent flow regime of Cr volatilisation.

One of the issues in modelling the high temperature oxidation of chromium at lower temperatures, as highlighted by this work, is the lack of diffusivity data, including self-diffusion in chromium rich alloys and diffusion chromium oxide. In this context, diffusion coefficient values can be affected by the diffusional medium, the temperature and the experimental method used. Published values available are for single- and polycrystalline Cr_2O_3 at a temperature of 1000ºC, with little mention of chromium oxides formed by iron-based alloys. In particular, Tsai [90] and Huntz [92] determined Cr diffusion coefficients in Cr_2O_3 formed on nickel-based alloys (Ni-30Cr) at 800–1100 ºC. As explained in chapters 2 and 6, this parameter can have significant effects upon the depletion process, so it is important to know which value is correct.

The modelling of alloys oxidation has progressed over the years, but mainly with regard to alumina-forming alloys used in the nuclear and automotive industry. As research on fuel cell metallic materials is still considered new, there is a lack of available models. Commercial software packages (Factsage, ThermoCalc, Dictra, MATLAB) that can model oxidation and interdiffusion still do not possess thermodynamic databases comprehensive enough to model chromium diffusion and oxidation as part of a multicomponent system; therefore, further development is needed in this area. The spinel formation on commercial steels in chapter 5 highlighted the importance of alloying elements, in particular manganese, which would also need to be accounted for in a full model of uncoated ferritic steels for SOFCs.

References

1. Lee H. *Statement by IPCC Chair, Opening of COP 25*. Madrid; 2019.

2. E4tech. *The Fuel Cell Industry Review*. E4tech. 2019;1–52.

3. Energy B. *Industry Leading Companies Choose Bloom Electrons for Immediate Cost Savings and Carbon Reduction Benefits*. Bloom Energy. 2011;

4. Steinberger-Wilckens, R., Dodds, P.E., Kurban, Z., Velazquez Abad, A., and Radcliffe J. *The Role of Hydrogen in Delivering Energy: A H2FC Supergen White Paper*. H2FC Supergen. 2017;

5. Timurkutluk B, Timurkutluk C, Mat MD, Kaplan Y. *Development of high-performance anode supported solid oxide fuel cell*. Int J Energy Res. 2012;36(15):1383–7.

6. Zhu WZ, Deevi SC. *Opportunity of metallic interconnects for solid oxide fuel cells: A status on contact resistance*. Mater Res Bull. 2003;38(6):957–72.

7. Zhu WZ, Deevi SC. *Development of interconnect materials for solid oxide fuel cells*. Mater Sci Eng A. 2003;348(1):227–43.

8. Barnett S. *A new solid oxide fuel cell design based on thin film electrolytes*. Energy. 1990;15(1):1–9.

9. de Souza S. *Thin-film solid oxide fuel cell with high performance at low-temperature*. Solid State Ionics. 1997;98(1–2):57–61.

10. de Souza S. *Reduced-Temperature Solid Oxide Fuel Cell Based on YSZ Thin-Film Electrolyte*. J Electrochem Soc. 1997;144(3):L35.

11. Abdalla AM, Hossain S, Azad AT, Petra PMI, Begum F, Eriksson SG, et al. *Nanomaterials for solid oxide fuel cells: A review*. Renew Sustain Energy Rev.

2018;82:353–68.

12. Charpentier, P Fragnauda, Schleicha PDM, Gehainb E. *Preparation of thin film SOFCs working at reduced temperature*. Solid State Ionics. 2000;135(1–4):373–80.

13. Maguire J. *Cathode materials for intermediate temperature SOFCs*. Solid State Ionics. 2000;127(3–4):329–35.

14. Ding, Jinguo, C. *Evaluation of Sr substituted Nd2CuO4 as a potential cathode material for intermediate-temperature solid oxide fuel cells*. Int J Hydrogen Energy. 2009;34(16):6869–75.

15. Sreedhar I, Agarwal B, Goyal P, Singh SA. *Recent advances in material and performance aspects of solid oxide fuel cells*. J Electroanal Chem. 2019;

16. Kendall K, Kendall M, Niewolak L, Tietz F, Quadakkers WJ. *Chapter 7-Interconnects*. In: High-Temperature Solid Oxide Fuel Cells for the 21st Century. 2016. p. 195–254.

17. Yang Z, Weil KS, Paxton DM, Stevenson JW. *Selection and Evaluation of Heat-Resistant Alloys for SOFC Interconnect Applications*. J Electrochem Soc. 2003;150(9):A1188.

18. Fontana S, Chevalier S, Caboche G. *Metallic interconnects for solid oxide fuel cell: Performance of reactive element oxide coating during 10, 20 and 30 months exposure*. Oxid Met. 2012;78(5–6):307–28.

19. Onishi T, Nakakubo S, Takeda M. *Calculations of Internal Oxidation Rate Equations and Boundary Conditions between Internal and External Oxidation in Silicon Containing Steels*. Mater Trans. 2010;51(3):482–7.

20. Fergus JW. *Lanthanum chromite-based materials for solid oxide fuel cell*

interconnects. Solid State Ionics. 2004;171(1–2):1–15.

21. Mahato N, Banerjee A, Gupta A, Omar S, Balani K. *Progress in material selection for solid oxide fuel cell technology: A review*. Prog Mater Sci. 2015;72(July):141–337.

22. Fontana S, Amendola R, Chevalier S, Piccardo P, Caboche G, Viviani M, et al. *Metallic interconnects for SOFC: Characterisation of corrosion resistance and conductivity evaluation at operating temperature of differently coated alloys*. J Power Sources. 2007;171(2):652–62.

23. Wu J, Liu X. *Recent Development of SOFC Metallic Interconnect*. J Mater Sci Technol. 2010;26(4):293–305.

24. Fergus JW. *Metallic interconnects for solid oxide fuel cells*. Mater Sci Eng A. 2005;397(1–2):271–83.

25. Yokokawa H. *Perovskite Oxide for Solid Oxide Fuel Cells*. 2009;(5).

26. Singh P, Yang Z, Viswanathan V, Stevenson JW. *Observations on the Structural Degradation of Silver During Simultaneous Exposure to Oxidizing and Reducing Environments*. J Mater Eng Perform. 2004;13(3):287–94.

27. Piccardo P, Amendola R. *SOFC's Interconnects Materials Development*. Aisofc. 2009;(June):189–94.

28. Jiang SP, Chen X. *Chromium deposition and poisoning of cathodes of solid oxide fuel cells - A review*. Int J Hydrogen Energy. 2014;39(1):505–31.

29. Nesbitt JA. *COSIM-A Finite Difference Computer Model to Predict Ternary Concentration Profiles Associated With Oxidation and Interdiffusion of Overlay-Coated Substrates*. 2000;TM 2000-20:1–42.

30. Pragnell WM, Evans HE. *A finite-difference model to predict 2D depletion profiles*

arising from high temperature oxidation of alloys. Model Simul Mater Sci Eng. 2006;14(4):733–40.

31. Eriksson R, Yuan K, Li X-H, Lin Peng R. *MCrAlY coating design based on oxidation–diffusion modelling. Part II: Lifing aspects*. Surf Coatings Technol. 2014 Aug;253:27–37.

32. Yuan K. *Oxidation and Corrosion of New MCrAlX Coatings - Modelling and Experiments*. 2014.

33. Niewolak L, Tietz F, Quadakkers WJ. *Interconnects*. High-Temperature Solid Oxide Fuel Cells 21st Century. 2016;195–254.

34. Badwal SPS, Foger K. *Solid oxide electrolyte fuel cell review*. Ceram Int. 1996 Jan;22(3):257–65.

35. Liebert B. *Electrical characterization of a chromium alloy interconnect materials*. In: Proceesings of Sixth International Symposium on Solid Oxide Fuel Cells (SOFC VI). Honolulu; 1999. p. 722–30.

36. Brandner M, Bienert C, Megel S, Kusnezoff M, Trofimenko N, Sauchuk V, et al. *Long Term Performance of Stacks with Chromium-based Interconnects (CFY)*. ECS Trans. 2013;57(1):2235–44.

37. Mah JCW, Muchtar A, Somalu MR, Ghazali MJ. *Metallic interconnects for solid oxide fuel cell: A review on protective coating and deposition techniques*. Int J Hydrogen Energy. 2016;42(14):9219–29.

38. Niewolak L, Tietz F, Quadakkers WJ. *Interconnects*. High-Temperature Solid Oxide Fuel Cells 21st Century. 2016;195–254.

39. Jablonski PD, Alman DE. *Oxidation resistance and mechanical properties of*

experimental low coefficient of thermal expansion (CTE) Ni-base alloys. Int J Hydrogen Energy. 2007;32(16):3705–12.

40. Singh R, Singh R. *Stainless Steels*. In: Applied Welding Engineering. Elsevier; 2016. p. 83–90.

41. Yokokawa H. *Overview of Intermediate-Temperature Solid Oxide Fuel Cells*. In 2009.

42. Bhadeshia H, Honeycombe R, Bhadeshia H, Honeycombe R. *Chapter 12 – Stainless Steel*. In: Steels: Microstructure and Properties. 2017.

43. Adams T a., Nease J, Tucker D, Barton PI. *Energy Conversion with Solid Oxide Fuel Cell Systems: A Review of Concepts and Outlooks for the Short- and Long-Term*. Ind Eng Chem Res. 2012;52(9):3089–111.

44. Pniok H. *Periodic Table* .

45. Bernier Cast Metals I. *Iron and Steel Casting Market : Growth Opportunities and forecast 2024*. 2018;

46. Lo KH, Shek CH, Lai JKL. *Recent developments in stainless steels*. Mater Sci Eng R Reports. 2009;65(4–6):39–104.

47. Shaigan N, Qu W, Ivey DG, Chen W. *A review of recent progress in coatings, surface modifications and alloy developments for solid oxide fuel cell ferritic stainless steel interconnects*. J Power Sources. 2010;195(6):1529–42.

48. Toh, C. H. Munroe, P. R. Young DJ. *Development of Alumina-Forming Austenitic (AFA) Stainless Steels Stainless Steels*. Mater Corros. 1999;60(3):7–28.

49. Grabke HJ. *Thermodynamics, mechanisms and kinetics of metal dusting*. Mater Corros - Werkstoffe und Korrosion. 1998;49(5):303–8.

50. Outokumpu. *Handbook of Stainless Steel*. Sandvikens Tryckeri. 2013;1–89.

51. Qin B, Wang ZY, Sun QS. *Effect of tempering temperature on properties of 00Cr16Ni5Mo stainless steel*. Mater Charact. 2008;59(8):1096–100.

52. Dalmau A, Richard C, Igual – Muñoz A. *Degradation mechanisms in martensitic stainless steels: Wear, corrosion and tribocorrosion appraisal*. Tribol Int. 2018 May 1;121:167–79.

53. Lula R. *Stainless Steels*. American Society for Metals; 1986.

54. Upadhyaya GS, Mukherjee SK. *Sintered 434L ferritic stainless steels*. Mater Des. 1985;6(6):323–7.

55. Öztürk B, Topcu A, Öztürk S, Cora ÖN. *Oxidation, electrical and mechanical properties of Crofer®22 solid oxide fuel cell metallic interconnects manufactured through powder metallurgy*. Int J Hydrogen Energy. 2018;43(23):10822–33.

56. Glatz W, Batawi E, Janousek M, Kraussler W, Zach R, Zobl G. *A New Low Cost Mass Production Route for Metallic SOFC-Interconnectors*. ECS Proc Vol. 1999;1999–19:783–90.

57. Glatz W, Janousek M, Batawi E, Honegger K. *Cost efficient industrial manufacturing routes for intermediate and high temperature SOFC interconnects*. In: Proceedings of 4th European SOFC Forum. 2000.

58. Herchen H, Karuppaiah C, Armstrong T, Verma A. *Method of making fuel cell interconnect using powder metallurgy*. Google Patents; 2015.

59. Glatz W, Kunschert G, Janousek M. *Powder-Metallurgical Processing and Properties of High Performance Metallic SOFC Interconnect Materials*. In: Proceedings of 6th European SOFC Forum. 2004.

60. Venskutonis A. *No Title*. In: P/M processing of ODS Cr- and FeCr-based alloys for

solid oxide fuel cell applications. 2005. p. 534.

61. Danninger H, Gierl-Mayer Dr C. *Advanced powder metallurgy steel alloys*. In: Advances in Powder Metallurgy: Properties, Processing and Applications. 2013.

62. Kang S-JL, Kang S-JL. *Sintering processess*. Sintering. 2005 Jan 1;3–8.

63. German RM. *Sintering Practice*. In: Sintering: from Empirical Observations to Scientific Principles. 2014.

64. Grolig JG, Froitzheim J, Svensson J-E. *Coated stainless steel 441 as interconnect material for solid oxide fuel cells: Evolution of electrical properties*. J Power Sources. 2015;284:321–7.

65. Jablonski PD, Cowen CJ, Sears JS. *Exploration of alloy 441 chemistry for solid oxide fuel cell interconnect application*. J Power Sources. 2010;195(3):813–20.

66. Sachitanand R, Sattari M, Svensson JE, Froitzheim J. *Evaluation of the oxidation and Cr evaporation properties of selected FeCr alloys used as SOFC interconnects*. Int J Hydrogen Energy. 2013;38(35):15328–34.

67. Metals V. *Crofer 22 H Material Data Sheet No. 4050*. 2010.

68. Rahaman MN. *Kinetics and mechanisms of densification*. Sinter Adv Mater. 2011;33–64.

69. Groover MP. *Fundamentals of modern manufacturing: materials processes, and systems.* John Wiley and Sons; 2013.

70. Sauerwald F. *The onset of grain growth in the absence of cold work in powder metal compacts produced by pressing and sintering*. Ztsch Anorg Chem. 1922;122:277–94.

71. Sauerwald F. *Factors essential in cold working and recrystallization studied in powder metal compacts*. Ztsch Elektrochemie. 1923;29:70–85.

72. Buytoz S, Orhan A, Gur AK, Caligulu U. *Microstructural Development of Fe-Cr-C and B4C Powder Alloy Coating on Stainless Steel by Plasma-Transferred Arc Weld Surfacing*. Arab J Sci Eng. 2013;38(8):2197–204.

73. Al-mangour B, Angeles L. *In : Stainless Steel P OWDER M ETALLURGY OF S TAINLESS*. 2016.

74. Dovydenkov VA, Radomysel ID. *Methods of production and properties of sintered stainless steels for machine components- a review*. Plenum Publ corportation. 1978;5(5).

75. Chasoglou D. *Surface Chemical Characteristics of Chromium-alloyed Steel Powder and the Role of Process Parameters during Sintering*. 2012;

76. Bouscaren AT. *The sinterability of chromium powder*. Am Polit Sci Rev. 1965;59(04):1014.

77. Schütze M, Quadakkers WJ. *Future Directions in the Field of High-Temperature Corrosion Research*. Oxid Met. 2017;(Iek 2).

78. H.J.T. Ellingham. *Reducibility of oxides and sulphides in metallurgical processes*. J Soc Chem Ind. 1944;63(5):125–60.

79. Wood GC. *High-temperature oxidation of alloys*. Oxid Met. 1970;2(1):11–57.

80. Kofstad P. *High Temperature Oxidation of Metals*. Mater Corros und Korrosion. 1967;18(10):956–7.

81. Young J. *The Nature of High Temperature Oxidation*. Corros Ser. 2008;1:1–27.

82. Young DJ. *Chapter 1 – The Nature of High Temperature Oxidation*. In: High Temperature Oxidation and Corrosion of Metals. 2016. p. 1–30.

83. Hindam H, Whittle DP. *Microstructure, adhesion and growth kinetics of protective*

scales on metals and alloys. Oxid Met. 1982;18(5–6):245–84.

84. ANZEL I. *High temperature oxidation of metals and alloys*. Br Corros J. 200AD;34(4):247–53.

85. Kofstad P, Lillerud KP. *On High Temperature Oxidation of Chromium II. Properties of Cr2O3 and the Oxidation Mechanism of Chromium*. J Electrochem Soc. 1980;127(November):2410–9.

86. Lillerud KP, Kofstad P. *On high temperature oxidation of chromium: I. Oxidation of annealed, thermally etched chromium at 800°--1100° C*. J Electrochem Soc. 1980;127(11):2397–410.

87. Stone H. *Chemical stability and high temperature oxidation*. University of Cambridge. 2014.

88. Smeltzer WW. *Oxidation theory of alloys*. In: Transactions of the Japan Institute of Metals, Supplement. Japan Inst of Metals; 1982. p. 35–43.

89. Zhang P. *Performance of MCrAlX coatings : Oxidation, Hot corrosion and Interdiffusion*. Linköping University Electronic Press; 2019.

90. Tsai SC, Huntz AM, Dolin C. *Growth mechanism of Cr2O3 scales: Oxygen and chromium diffusion, oxidation kinetics and effect of yttrium*. Mater Sci Eng A. 1996;212(1):6–13.

91. Balogh Z, Schmitz G. *Diffusion in Metals and Alloys*. Phys Metall. 2014;387–559.

92. Huntz AM, Balmain J, Tsaï SC, Messaoudi K, Loudjani MK, Lesage B, et al. *Diffusion studies in oxides scales grown on alumina-and chromia-forming alloys*. Scr Mater. 1997 Sep;37(5):651–60.

93. Horita T, Yamaji K, Xiong Y, Kishimoto H, Sakai N, Yokokawa H. *Oxide scale*

formation of Fe–Cr alloys and oxygen diffusion in the scale. Solid State Ionics. 2004;175(1):157–63.

94. Gusak A. *Diffusion-Controlled Solid State Reactions, in Alloys, Thin-Films, and Nano Systems*. In: Diffusion-Controlled Solid State Reactions: In Alloys, Thin-Films, and Nano Systems. 2010. p. 11–35.

95. Mehrer H. *Diffusion in Solids – Fundamentals, Methods, Materials, Diffusion-Controlled Processes*. Springer Series in Solid-State Sciences. Volume 155. 2007.

96. Sabioni ACS, Huntz AM, Silva F, Jomard F. *Diffusion of iron in Cr2O3: polycrystals and thin films*. Mater Sci Eng A. 2005;392(1):254–61.

97. Sabioni ACS, Huntz AM, Philibert J, Lesage B, Monty C. *Relation between the oxidation growth rate of chromia scales and self-diffusion in Cr2O3*. J Mater Sci. 1992;27(17):4782–90.

98. Lobnig RE, Schmidt HP, Hennesen K, Grabke HJ. *Diffusion of cations in chromia layers grown on iron-base alloys*. Oxid Met. 1992;37(1–2):81–93.

99. Jiang SP, Chen X. *Chromium deposition and poisoning of cathodes of solid oxide fuel cells - A review*. Int J Hydrogen Energy. 2014;39(1):505–31.

100. Tucker MC, Kurokawa H, Jacobson CP, De Jonghe LC, Visco SJ. *A fundamental study of chromium deposition on solid oxide fuel cell cathode materials*. J Power Sources. 2006;160(1):130–8.

101. Jiang SP, Zhen Y. *Mechanism of Cr deposition and its application in the development of Cr-tolerant cathodes of solid oxide fuel cells*. Solid State Ionics. 2008;179(27):1459–64.

102. Paulson SC, Birss VI. *Chromium Poisoning of LSM-YSZ SOFC Cathodes*. J

Electrochem Soc. 2004;151(11):A1961.

103. Park E, Taniguchi S, Daio T, Chou J-T, Sasaki K. *Comparison of chromium poisoning among solid oxide fuel cell cathode materials*. Solid State Ionics. 2014;262:421–7.

104. Hart N, Brandon N, Day M, Lapeña-Rey N. *Functionally Graded Composite Cathodes for Solid-Oxide Fuel Cell*. J Power Sources. 2002 Apr 1;106:42–50.

105. Falk-Windisch H, Svensson JE, Froitzheim J. *The effect of temperature on chromium vaporization and oxide scale growth on interconnect steels for Solid Oxide Fuel Cells*. J Power Sources. 2015;287:25–35.

106. Kaun T, Cruse T, Krumpelt M. *Chromium poisoning of cathodes by ferritic stainless steels*. Ceram Eng Soc Proc. 2004;25(3):401–6.

107. Kim J, Sprenkle V, Canfield N, Meinhardt K, Chick L. *Effects of chrome contamination on the performance of La0.6Sr0.4Co0.2Fe0.8O3 cathode used in solid oxide fuel cells*. J Electrochem Soc. 2006;153(5):880–6.

108. Megel S, Girdauskaite E, Sauchuk V, Kusnezoff M, Michaelis A. *Area specific resistance of oxide scales grown on ferritic alloys for solid oxide fuel cell interconnects*. J Power Sources. 2011 Sep 1;196(17):7136–43.

109. ThyssenKrupp. *Crofer 22 APU - Material Data Sheet No. 4046*. ThyssenKrupp VDM. 2010;(4046).

110. Hua B, Pu J, Lu F, Zhang J, Chi B, Jian L. *Development of a Fe–Cr alloy for interconnect application in intermediate temperature solid oxide fuel cells*. J Power Sources. 2010 May;195(9):2782–8.

111. Windisch HF, Froitzheim J, Svensson JE. *Influence of Chromium Evaporation and Oxidation on Interconnect Steels at 650- 850°C*. 2013;57(1):2225–33.

112. Petric A, Ling H. *Electrical conductivity and thermal expansion of spinels at elevated temperatures*. J Am Ceram Soc. 2007;90(5):1515–20.

113. Froitzheim J, Ravash H, Larsson E, Johansson LG, Svensson JE. *Investigation of Chromium Volatilization from FeCr Interconnects by a Denuder Technique*. J Electrochem Soc. 2010;157(9):B1295.

114. Dheeradhada VS, Cao H, Alinger MJ. *Oxidation of ferritic stainless steel interconnects: Thermodynamic and kinetic assessment*. J Power Sources. 2011;196(4):1975–82.

115. LeSar R. *Introduction to Computational Materials Science* [Internet]. Cambridge: Cambridge University Press; 2013.

116. Khan MZ, Mehran MT, Song R-H, Lee J-W, Lee S-B, Lim T-H. *A simplified approach to predict performance degradation of a solid oxide fuel cell anode*. J Power Sources. 2018 Jul 1;391:94–105.

117. Kakaç S, Pramuanjaroenkij A, Zhou XY. *A review of numerical modeling of solid oxide fuel cells*. Int J Hydrogen Energy. 2007 May 1;32(7):761–86.

118. Zeng S, Zhang X, Song Chen J, Li T, Andersson M. *Modeling of solid oxide fuel cells with optimized interconnect designs*. Int J Heat Mass Transf. 2018;125:506–14.

119. Hajimolana SA, Hussain MA, Daud WMAW, Soroush M, Shamiri A. *Mathematical modeling of solid oxide fuel cells: A review*. Renew Sustain Energy Rev. 2011 May 1;15(4):1893–917.

120. Grew KN, Chiu WKS. *A review of modeling and simulation techniques across the length scales for the solid oxide fuel cell*. J Power Sources. 2012 Feb 1;199:1–13.

121. Peksen M. *Numerical thermomechanical modelling of solid oxide fuel cells*. Prog

Energy Combust Sci. 2015;48:1–20.

122. Hack K. *Computational thermodynamics: A mature scientific tool for industry and academia*. Pure Appl Chem. 2011;83(5):1031–44.

123. Ahn K, Choi S, Lee J-H, Kim B-K, Kim J, Kim H. *Enhanced carbon tolerance on Ni-based reforming catalyst with Ir alloying: A DFT study*. Appl Surf Sci. 2017 Oct 15;419:678–82.

124. Sugiura S, Shibuta Y, Shimamura K, Misawa M, Shimojo F. *Role of oxygen vacancy in dissociation of oxygen molecule on SOFC cathode: Ab initio molecular dynamics simulation*. Solid State Ionics. 2016;285:209–14.

125. Ma Y, Fenineche N, Elkedim O. *Ab initio study of La10−xSrx(Si,Ge)6O27−0.5x apatite for SOFC electrolyte*. Comput Mater Sci. 2015 Nov 1;109:25–33.

126. Galea NM, Lo JMH, Ziegler T. *A DFT study on the removal of adsorbed sulfur from a nickel(111) surface: Reducing anode poisoning*. J Catal. 2009 Apr 25;263(2):380–9.

127. Zhou J, Chen G, Wu K, Cheng Y, Peng B, Guo J, et al. *Density functional theory study on oxygen adsorption in LaSrCoO4: An extended cathode material for solid oxide fuel cells*. Appl Surf Sci. 2012;258(7):3133–8.

128. Lai H-Y, Chan Y-H, Chen C-K. *Enhancement of ion conductivity for doped electrolytes in SOFC by MD modeling*. Comput Mater Sci. 2018;144:265–72.

129. Lu H, Hua D, Iqabl T, Zhang X, Li G, Zhang D. *Molecular dynamics simulations of the coke formation progress on the nickel-based anode of solid oxide fuel cells*. Int Commun Heat Mass Transf. 2018 Feb 1;91:40–7.

130. Yang Z, Guo M, Wang N, Ma C, Wang J, Han M. *A short review of cathode poisoning and corrosion in solid oxide fuel cell*. Int J Hydrogen Energy. 2017;42(39):24948–59.

131. Wei S-S, Wang T-H, Wu J-S. *Numerical modeling of interconnect flow channel design and thermal stress analysis of a planar anode-supported solid oxide fuel cell stack.* Energy. 2014;69:553–61.

132. Liu X, Martin CL, Delette G, Laurencin J, Bouvard D, Delahaye T. *Microstructure of porous composite electrodes generated by the discrete element method*. J Power Sources. 2011;196(4):2046–54.

133. Lei Y, Cheng T-L, Wen Y-H. *Phase field modeling of microstructure evolution and concomitant effective conductivity change in solid oxide fuel cell electrodes*. J Power Sources. 2017 Mar 31;345:275–89.

134. Davis R, Haataja M. *Microstructural stability of supported metal catalysts: A phase field approach*. J Power Sources. 2017;369:111–21.

135. Jiao Z, Shikazono N. *Simulation of the reduction process of solid oxide fuel cell composite anode based on phase field method*. J Power Sources. 2016;305:10–6.

136. Chen S, Doolen GD. *Lattice Boltzmann Method*. Annu Rev Fluid Mech. 1998;30:329–64.

137. Espinoza-Andaluz M, Andersson M, Sundén B. *Modeling of a Gradient Porosity SOFC Anode using the Lattice Boltzmann Method*. Energy Procedia. 2017;105:1332–8.

138. Xu H, Dang Z. *Lattice Boltzmann modeling of carbon deposition in porous anode of a solid oxide fuel cell with internal reforming*. Appl Energy. 2016;178:294–307.

139. Xu H, Dang Z. *Numerical investigation of coupled mass transport and electrochemical reactions in porous SOFC anode microstructure*. Int J Heat Mass Transf. 2017;109:1252–60.

140. Darvish S, Wang CC, Jiang SP, Zhong Y. *Thermodynamic stability mapping and electrochemical study of La 1-x Sr x Co 0.2 Fe 0.8 O 3 ± δ (x=0.2–0.4) as a cathode of solid oxide fuel cells in the presence of SO 2*. Electrochim Acta. 2018;0–28.

141. Povoden E, Chen M, Grundy AN, Ivas T, Gauckler LJ. *Thermodynamic Assessment of the La-Cr-O System*. J Phase Equilibria Diffus. 2009;30(1):12–27.

142. Povoden E, Grundy AN, Gauckler LJ. *Thermodynamic reassessment of the Cr-O system in the framework of Solid Oxide Fuel Cell (SOFC) research*. J Phase Equilibria Diffus. 2006;27(4):353–62.

143. Carl W. *Beitrag zur Theorie des Anlaufvorgangs*. Vol. 21B, Zeitschrift für Physikalische Chemie. 1933. p. 25.

144. Whittle DP, Evans DJ, Scully DB, Wood GC. *Compositional changes in the underlying alloy during the protective oxidation of alloys*. Acta Metall. 1967;15(9):1421–30.

145. Xu Z, Xu W, Stephens E, Koeppel B. *Mechanical reliability and life prediction of coated metallic interconnects within solid oxide fuel cells*. Renew Energy. 2017;113:1472–9.

146. Xu Z, Rosso KM, Bruemmer S. *Metal oxidation kinetics and the transition from thin to thick films*. Phys Chem Chem Phys. 2012;14(42):14534.

147. Dorcheh AS, Schütze M, Galetz MC. *Factors affecting isothermal oxidation of pure chromium in air*. Corros Sci. 2018;130(May 2017):261–9.

148. Nijdam T., Jeurgens LP., Sloof W. *Modelling the thermal oxidation of ternary alloys—compositional changes in the alloy and the development of oxide phases*. Acta Mater. 2003;51(18):5295–307.

149. Crank J. *the Mathematics of Diffusion*. 2nd Ed Oxford Univ Press UK. 1975;

150. Krupp U, Chang SY, Schimke A. *Modelling Internal Corrosion Processes as*.

151. Evans HE. *Stress effects in high temperature oxidation of metals*. Int Mater Rev. 1995 Jan 1;40(1):1–40.

152. Nijdam TJ, Jeurgens LPH, Sloof WG. *Modelling the thermal oxidation of ternary alloys - Compositional changes in the alloy and the development of oxide phases*. Acta Mater. 2003;51(18):5295–307.

153. Hansson AN, Hattel JH, Dahl K V. *Modelling Cr depletion under a growing Cr 2 O 3 layer on austenitic stainless steel : the influence of grain*. IOP Publ Model Simul Mater Sci Eng Model. 2009;17(3).

154. Fisher JC. *Calculation of diffusion penetration curves for surface and grain boundary diffusion*. J Appl Phys. 1951;22(1):74–7.

155. Andersson J-O, Helander T, Höglund L, Shi P, Sundman B. *Thermo-Calc & DICTRA, computational tools for materials science*. Calphad. 2002;26(2):273–312.

156. SHI P fang, Engström A, Höglund L, CHEN Q, Sundman B, Ågren J, et al. *Computational Thermodynamics and Kinetics in Materials Modelling and Simulations*. J Iron Steel Res Int. 2007;14(5 SUPPL. 1):210–5.

157. Wessman S. *Applications of Computational Thermodynamics and Kinetics on Transformations in Stainless Steels* [Internet]. 2013.

158. Eriksson R, Yuan K, Li X-H, Lin Peng R. *MCrAlY coating design based on oxidation–diffusion modelling. Part II: Lifing aspects*. Surf Coatings Technol. 2014;253:27–37.

159. Larsson H, Jonsson T, Naraghi R, Gong Y, Reed RC, Ågren J. *Oxidation of iron at 600 °C – experiments and simulations*. Mater Corros. 2017;68(2):133–42.

160. Zwetanova A, Machkova A, Christov M. *Modelling of chromium contamination of sofc cathodes from metallic interconnects*. 2007;42(1):89–92.

161. Antepara I, Villarreal I, Rodríguez-Martínez LM, Lecanda N, Castro U, Laresgoiti A. *Evaluation of ferritic steels for use as interconnects and porous metal supports in IT-SOFCs*. J Power Sources. 2005;151:103–7.

162. England DM, Virkar A V. *Oxidation Kinetics of Some Nickel-Based Superalloy Foils in Humidified Hydrogen and Electronic Resistance of the Oxide Scale Formed Part II*. J Electrochem Soc. 2001;148(4):A330.

163. Corporation FI. *The Essential Waterjet Flowmaster ® Software* [Internet]. 2011. p. 1–5.

164. Kerker M, Loebl EM. *The Scattering of Light and Other Electromagnetic Radiation: Physical Chemistry: A Series of Monographs* [Internet]. Elsevier Science; 2013. (Physical chemistry).

165. Gu L, Robles-Kelly A. *Shadow modelling based upon Rayleigh scattering and Mie theory*. Pattern Recognit Lett. 2014 Jul 1;43:89–97.

166. Webb P a. *Volume and Density Determinations for Particle Technologists*. Society. 2001;(February):1–16.

167. Sanchez-Hachair A, Hofmann A. *Hexavalent chromium quantification in solution: Comparing direct UV–visible spectrometry with 1,5-diphenylcarbazide colorimetry*. Comptes Rendus Chim. 2018;21(9):890–6.

168. Badwal SPS, Giddey S, Munnings C, Kulkarni A. *Review of progress in high temperature solid oxide fuel cells*. J Aust Ceram Soc. 2014;50(1):23–37.

169. Froitzheim J, Meier GH, Niewolak L, Ennis PJ, Hattendorf H, Singheiser L, et al.

Development of high strength ferritic steel for interconnect application in SOFCs. J Power Sources. 2008 Mar;178(1):163–73.

170. Michalik, Marek / Hänsel, Michael / Quadakkers WJ. *Effect of water vapour on growth and adherence of chromia scales on pure chromium*. Forschungszentrum Jülich's Publ House. 2007;

171. Thongyai N, Daowphiset S, Pungwiwat N. *Study of Stainless Steel Surface Cleanability*. (2):2–4.

172. Henriques B, Soares D, Silva FS. *Optimization of bond strength between gold alloy and porcelain through a composite interlayer obtained by powder metallurgy*. Mater Sci Eng A. 2011 Jan 25;528(3):1415–20.

173. German RM. *Measurement Tools and Experimental Observations*. Sintering: from Empirical Observations to Scientific Principles. 2014. 71–130 p.

174. Quadakkers WJ, Malkow T, Piron-Abellan J, Flesch U, Shemet V, Singheiser L. *No*. In: McEvoy A, editor. Proceedings of the 4th European Solid Oxide Fuel Cell Forum. Lucerne: The European SOFC Forum; 2000. p. 827–36.

175. Pujilaksono B, Jonsson T, Heidari H, Halvarsson M, Svensson JE, Johansson LG. *Oxidation of binary FeCr alloys (Fe-2.25Cr, Fe-10Cr, Fe-18Cr and Fe-25Cr) in O2 and in O2 + H2O environment at 600 °c*. Oxid Met. 2011;75(3–4):183–207.

176. Mrowec S, Stokłosa A. *Calculations of parabolic rate constants for metal oxidation*. Oxid Met. 1974;8(6):379–91.

177. Opila EJ, Myers DL, Jacobson NS, Nielsen IMB, Johnson DF, Olminsky JK, et al. *Theoretical and Experimental Investigation of the Thermochemistry of CrO2(OH)2(g)*. J Phys Chem A. 2007 Mar 1;111(10):1971–80.

178. Gulbransen EA, Andrew KF. *Kinetics of the Oxidation of Chromium*. J Electrochem Soc. 1957;104(6):334.

179. Pujilaksono B, Jonsson T, Halvarsson M, Panas I, Svensson JE, Johansson LG. *Paralinear oxidation of chromium in O 2 + H 2O environment at 600-700 °c*. Oxid Met. 2008;70(3–4):163–88.

180. Grolig JG, Froitzheim J, Svensson J-E. *Coated stainless steel 441 as interconnect material for solid oxide fuel cells: Oxidation performance and chromium evaporation*. J Power Sources. 2014;248:1007–13.

181. Stygar M, Brylewski T, Kruk A, Przybylski K. *Oxidation properties of ferritic stainless steel in dual Ar-H 2-H2O/air atmosphere exposure with regard to SOFC interconnect application*. Solid State Ionics. 2014;262:449–53.

182. Talic B, Venkatachalam V, Hendriksen PV, Kiebach R. *Comparison of MnCo2O4 coated Crofer 22 H, 441, 430 as interconnects for intermediate-temperature solid oxide fuel cell stacks*. J Alloys Compd. 2020;821:153229.

183. Alnegren P, Engineering B, Chemistry IE. *Oxidation behavior of selected FeCr alloys in environments relevant for solid oxide electrolysis applications*. Thesis. 2012;

184. Young DJ, Zurek J, Singheiser L, Quadakkers WJ. *Temperature dependence of oxide scale formation on high-Cr ferritic steels in Ar–H2–H2O*. Corros Sci. 2011;53(6):2131–41.

185. Grolig JG, Froitzheim J, Svensson J-E. *Coated stainless steel 441 as interconnect material for solid oxide fuel cells: Evolution of electrical properties*. J Power Sources. 2015;284:321–7.

186. Hillert M. *The compound energy formalism*. J Alloys Compd. 2001;320(2):161–76.

187. Tsai SC, Huntz AM, Dolin C. *Diffusion of18O in massive Cr2O3 and in Cr2O3 scales at 900°C and its relation to the oxidation kinetics of chromia forming alloys*. Oxid Met. 1995;43(5–6):581–96.

188. Rafal Abdank-Kozubski. *Recent Progress in Diffusion Thermodynamics and Kinetics in Intermetallic Compounds*. Trans Tech Publications Ltd; 2014. 229 p.

189. Wu RTC. *Mechanisms of High Temperature Degradation of Thermal Barrier Coatings*. Imperial College, London; 2009.